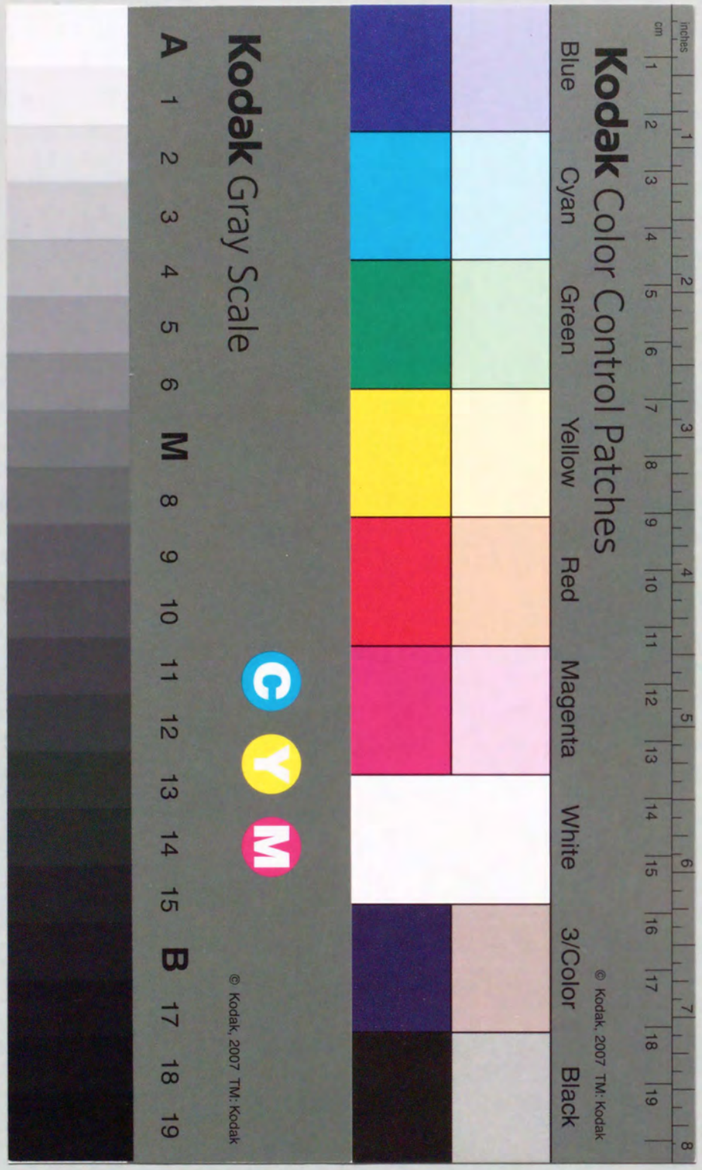
OUKA
The University of Osaka
Institutional Knowledge Archive

Title	OBSERVATION OF S=1/2 DEGREES OF FREEDOM IN AN S=1 LINEAR-CHAIN HEISENBERG ANTIFERROMAGNET
Author(s)	Hagiwara, Masayuki
Citation	大阪大学, 1992, 博士論文
Version Type	VoR
URL	https://doi.org/10.11501/3091087
rights	
Note	

The University of Osaka Institutional Knowledge Archive : OUKA

https://ir.library.osaka-u.ac.jp/

The University of Osaka



OBSERVATION OF S=1/2 DEGREES OF FREEDOM IN AN S=1 LINEAR-CHAIN HEISENBERG ANTIFERROMAGNET

by

Masayuki HAGIWARA

DISSERTATION IN PHYSICS

THE OSAKA UNIVERSITY

GRADUATE SCHOOL OF SCIENCE

TOYONAKA, OSAKA

OBSERVATION OF S=1/2 DEGREES OF FREEDOM IN AN S=1 LINEAR-CHAIN HEISENBERG ANTIFERROMAGNET

by

Masayuki HAGIWARA

DISSERTATION IN PHYSICS

THE OSAKA UNIVERSITY

GRADUATE SCHOOL OF SCIENCE

TOYONAKA, OSAKA

July, 1992

Contents

page

Abstract vii

List of symbols viii

§ 1. Introduction

1-1. Linear chain magnetic systems 1

1-2. Haldane effect 14

§ 2. Crystal and magnetic properties of $Ni(C_2H_8N_2)_2NO_2ClO_4$ (NENP)

2-1. Crystal structure of NENP 23

2-2. Magnetic properties of NENP 25

§ 3. Experimental procedure

3-1. Sample preparation 35

3-2. Electron spin resonance (ESR) measurement

3-2-1. X-band ESR spectrometer 36

3-2-2. K-band ESR spectrometer 39

3-2-3. Detection of ESR signals 40

3-2-4. X-band ESR cryostat 40

3-2-5. Temperature control system 41

3-3. Magnetization measurement

3-3-1. SQUID susceptometer 44

3-3-2. Method of signal detection 47

3-4. High field magnetization measurement

3-4-1. Magnet system 50

3-4-2. Method of magnetization measurement 50

3-4-3. Other techniques 52

§ 4. ESR experiment on Cu : NENP

4-1. ESR signals observed at X- and K-bands 54

4-2. Temperature dependence 59

4-3. Angular dependence 62

4-4. Hyperfine lines 66

§ 5. Analysis

5-1. Model Hamiltonian 69

5-2. Temperature dependence 71

5-3. Angular dependence 74

5-4. Energy diagram 77

5-5. Hyperfine lines 80

5-6. Magnetization in Cu : NENP 88

§ 6. High field magnetization process of Cu : NENP

6-1. Experimental results 90

6-2. Analysis 92

§ 7. Spin 1/2 degrees of freedom in an undoped NENP

7-1. Background 96

7-2. Experimental results 98

7-3. Analysis 105

§ 8. Conclusions 110

Acknowledgements 111

References 113

Appendix I.

The hyperfine lines in the present model 120

Appendix II.

The angular dependence of the hyperfine lines 123

Appendix III.

Calculation of the magnetization curve 127

Abstract

An electron spin resonance (ESR) and magnetization measurements have been performed on single crystal samples of the spin(S) one quasi-one-dimensional Heisenberg antiferromagnet $Ni(C_2H_8N_2)_2NO_2ClO_4$ (NENP) containing Cu impurities. Novel ESR signals have been observed at low temperatures in these crystals whose intensity decreases rapidly as the temperature is increased. The experimental results are well explained by a model based on the valence-bond-solid (VBS) state : namely, when a Ni atom in NENP is substituted by a Cu atom, the valence bonds in the VBS state are broken at the Cu site resulting in S=1/2 degrees of freedom at the Ni sites neighboring the Cu atom.

The result of the magnetization measurements on the same system is quantitatively explained by the model without any adjustable parameters. The S=1/2 degrees of freedom have also been observed in an imperfect single crystal of NENP without impurity atoms from ESR and magnetization measurements.

This study provides the first experimental evidence for the existence of a fractional spin in magnetic system. At the same time, the ground state of an S=1 linear-chain Heisenberg antiferromagnet is shown to be well approximated by the VBS model.

List of symbols

The symbols which often appear in the text have the following meaning :

D : Single ion anisotropy constant (uniaxial anisotropy)
E : Single ion anisotropy constant (rhombic anisotropy)
E_G : Haldane gap energy
h : Plank's constant ($\hbar=h/2\pi$)
$\vec{H}$: External magnetic field
J : Nearest neighbor intrachain exchange constant
J' : Nearest neighbor interchain exchange constant
k_B : Boltzmann constant
μ_B : Bohr magneton
μ_N : Nuclear magneton
ν_0 : ESR frequency
S : Spin operator
T : Temperature

§ 1. Introduction

1-1. Linear chain magnetic systems

The study of linear chain magnetic systems has a long history. The linear chain magnetic system is defined as the one in which exchange interactions exist only in the chain direction. Although there is no ideal linear chain magnetic system in real substances, the study of the system has the following importance and viewpoints :
(i) It is easier to calculate the magnetic properties than to do so in higher dimensions. In some cases, exact solutions of the interacting many body systems in which quantum effects play an important role are obtained, and are used to test the validity of quantum statistical mechanics. (ii) The critical region is enhanced in linear chain systems in comparison with that in three dimensional magnetic systems. Therefore, novel properties appear and the study of these phenomena gives a clue in understanding phase transitions.
(iii) A number of magnetic substances close to ideal linear chain magnetic systems has been found and investigated extensively from the 1960s.

The Hamiltonian for a linear chain magnetic system in zero field is given by

$$\mathcal{H} = -2 \sum_i \{ J_{/\!/} S_i^z S_{i+1}^z + J_\perp (S_i^x S_{i+1}^x + S_i^y S_{i+1}^y) \} , \qquad (1\text{-}1\text{-}1)$$

where $J_{//}$ and $J_{\perp}$ are the nearest neighbor exchange interaction constants parallel and perpendicular to the quantization axis (z-axis), respectively, and S_i^x, S_i^y and S_i^z are the components of electron spin vector at the i-th site. Equation (1-1-1) represents, in the case of $J_{//}=J_{\perp}$ the Heisenberg Hamiltonian, for $J_{//}=0$ XY one and for $J_{\perp}=0$ Ising one, respectively.

Theoretical work on the Hamiltonian (1-1-1) for $J_{//}=J_{\perp}$ and S=1/2 dates back to 1930 when Bloch[1] introduced the concept of a spin wave and gave the exact eigen states for a ferromagnet with one flopped spin. In 1931, Bethe[2] obtained, based on an ansatz, the exact eigen states for interacting spin waves for arbitrary number of flopped spins on an S=1/2 linear chain. Hulthén[3] used the Bethe ansatz to obtain the exact value for the ground state energy in an S=1/2 linear chain Heisenberg antiferromagnet (LCHA) in 1938. These arguments for $J_{//}=J_{\perp}$ were extended by Orbach[4] (1958) and by Walker[5] (1959) to the cases ranging from $J_{\perp}=0$ to $J_{\perp}=J_{//}$. Yang and Yang[6] proved exactly the Bethe ansatz for the ground state of a finite linear chain antiferromagnet (1966).

The magnetization curve and susceptibility of these systems at zero temperature were calculated by Griffiths[7] in 1964. The thermal and magnetic properties in external magnetic field at non-zero temperatures were investigated by Bonner and Fisher[8] who carried out the computer calculation for the number of spins in the chain N=2 to 11 in the range from $J_{\perp}=0$ to $J_{\perp}=J_{//}$ and for ferro- and antiferro-magnetic couplings (1964). They also estimated the behavior of thermal and magnetic properties of an infinite chain ($N=\infty$) by extrapolation. Although the ground state energy for the

S=1/2 LCHA was calculated exactly[3], an intuitive physical picture expressing the ground state had not been obtained until recently. Anderson[9] proposed in 1973 the resonating-valence-bonds (RVB) state as a physical picture for the ground state of an S=1/2 Heisenberg antiferromagnet. The RVB state is composed of singlet pairs (valence bonds). The energy of the RVB state becomes lower than that of the classical Néel state and is close to the exact value obtained by Hulthén[3].

The XY Hamiltonian ($J_{//}=0$) is solvable. Lieb, Shultz and Mattis[10] obtained the ground state energy, elementary excitation and free energy exactly (1961), and Katsura[11] studied the thermal and magnetic properties including the behavior in a field (1962). The S=1/2 Ising Hamiltonian ($J_{\perp}=0$) is easy to solve exactly[12]. The magnetic and thermal properties of the Ising model with S=1/2, 1 and 3/2 were calculated exactly by Suzuki et al.[13] and Obokata and Oguchi[14]. As to classical spin ($S=\infty$) systems, Fisher[15] calculated exactly the free energy, susceptibility and correlation functions of one dimensional Heisenberg magnet (1964).

Concerning elementary excitations, the spin wave theories were developed by Holstein and Primakoff[16] and by Dyson[17] for a ferromagnetic coupling and by Anderson[18] and by Kubo[19] for an antiferromagnetic coupling in the 1950s. Anderson obtained the relation $\varepsilon(\mathbf{k})=2|J||\sin\mathbf{k}|$, where $\mathbf{k}$ is the wave vector, for the spin wave dispersion in an S=1/2 LCHA. In 1962, des Cloizeaux and Pearson[20] calculated exactly the spin wave states for an S=1/2 infinite LCHA and obtained the dispersion relation $\varepsilon(\mathbf{k})=\pi|J||\sin\mathbf{k}|$ which is $\pi/2$ times larger than that obtained in the classical spin

wave theory. Dynamics of linear chain magnetic systems has been investigated extensively from the 1970s. One of the non-linear excitations of these systems is known as magnetic soliton and was first investigated by Nakamura and Sasada[21] (1974). The solitons in the linear-chain XY ferromagnet and antiferromagnet in a symmetry-breaking external magnetic field were studied theoretically by Mikeska[22,23] (1978,1980). The propagative spin mode in an Ising-like antiferromagnet was predicted by Villain[24] (1975) and Ishimura and Shiba[25] (1980).

Experimentally, linear chain magnetic systems were extensively studied in the 1960s and the 1970s[26,27], and were compared with the theory mentioned above. Most of the experimental work on one dimensional magnets has been performed on Heisenberg systems. The properties of some of the antiferromagnetic Heisenberg chain and the other magnetic chain substances are listed in Tables 1-1-1 and 1-1-2, respectively. In Table 1-1-1, the values of $|J'/J|$ were calculated by Oguchi[28].

Here, we show some experimental results on linear chain magnets. The susceptibility datum of $CuCl_2{\cdot}2NC_5H_5$ compound obtained by Takeda et al.[29] is shown in Fig. 1-1-1. This compound is a typical S=1/2 Heisenberg antiferromagnet and the agreement between the experiment and the theory is excellent above 2 K. The magnetization datum of this compound is plotted and compared with the theoretical curve calculated by Griffiths[7] in Fig. 1-1-2. The same authors[29] also investigated a linear chain Ising ferromagnet $CoCl_2{\cdot}2NC_5H_5$. The specific heat of this compound is shown in Fig. 1-1-3. In this case, the rounded maximum in the specific heat

	S	$T(\chi_{max})$ (K)	$T(C_{max})$ (K)	$\frac{C_{max}}{R}$	$\frac{T(\chi_{max})}{T(C_{max})}$	$\frac{\chi_{max}T(\chi_{max})}{g^2}$	J/k (K)	T_c (K)	T_c/θ	$\lvert J'/J\rvert$ (Oguchi)
$CuCl_2 \cdot 2NC_5H_5$	$\frac{1}{2}$	17·5				0·035	−13	1·13	0·087	4×10^{-3}
$KCuF_3$	$\frac{1}{2}$	243				0·036	−190	38 22	0·20 0·12	$1·6 \times 10^{-2}$ 6×10^{-3}
$CuCl_2$	$\frac{1}{2}$	70	40	0·61	1·75	0·035	$\simeq -60$	23·91	$\simeq 0·4$	$\simeq 6 \times 10^{-2}$
Iminoxyl radical	$\frac{1}{2}$	$\simeq 6$	4	0·328	$\simeq 1·5$	0·035	−4·2	?(<1·3)	?	?
$CsNiCl_3$	1	35				0·085	−13	4·65	0·13	7×10^{-3}
$RbNiCl_3$	1	45				0·079	−17	11	0·24	2×10^{-2}
$CsMnCl_3 \cdot 2H_2O$	$\frac{5}{2}$	32				0·38	−3·57	4·89	0·12	6×10^{-3}
$[(CH_3)_4N][MnCl_3]$	$\frac{5}{2}$	55				0·34	−6·5	0·84	0·011	$< 10^{-4}$

Table 1-1-1. Magnetic and thermal properties of some antiferromagnetic chains. Here, χ and C represent the magnetic susceptibility and the specific heat, respectively, T_c the transition temperature at which three-dimensional ordering occurs and θ is the Curie-Weiss constant. The ratio of J' to J is calculated by Oguchi[28]. (Quoted from ref. 26)

	Type of interaction	Sign of interaction	S	J/k (K)	T_c (K)	T_c/θ
$CsCuCl_3$	Heisenberg	+	$\frac{1}{2}$	?	10·4	?
$[(CH_3)_4N][NiCl_3]$	Heisenberg	+	1	1·0	? (<1·7)	? (<0·6)
$K_3Fe(CN)_6$	Ising	−	$\frac{1}{2}$	−0·23	0·129	0·56
$CsCoCl_3$	Ising	−	$\frac{1}{2}$	≃−100 (?)	≃8 (?)	≃0·08 (?)
$Dy(C_2H_5SO_4)_2 \cdot 9H_2O$	Ising	+	$\frac{1}{2}$	0·2	0·13	0·5
$CoCl_2 \cdot 2NC_5H_5$	Ising	+	$\frac{1}{2}$	9·5	3·5	0·37
$RbFeCl_3$	PH	+	1	?	2·55	?
$CsNiF_3$	PH	+	1	≃−8·3	2·61	≃0·12

Table 1-1-2. Magnetic and thermal properties of other simple chain systems : the ferromagnetic Heisenberg chain, the antiferromagnetic and ferromagnetic Ising chain and the ferromagnetic planar Heisenberg (PH) chain. (Quoted from ref. 26)

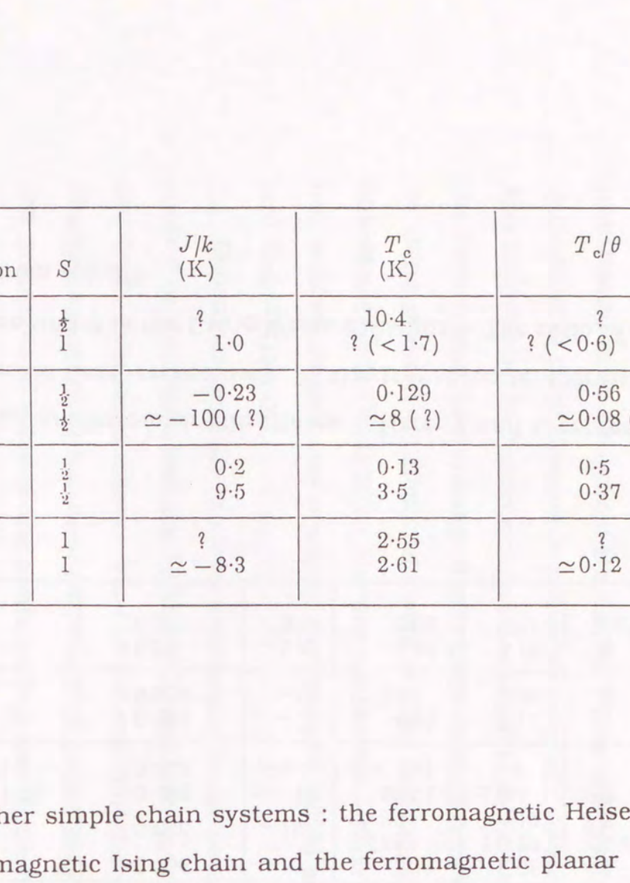


Fig. 1-1-1. Powder susceptibility of the S=1/2 LCHA $CuCl_2 \cdot 2NC_5H_5$. The departure between the experiment and the theory below 2 K is enhanced. (Quoted from ref. 29)

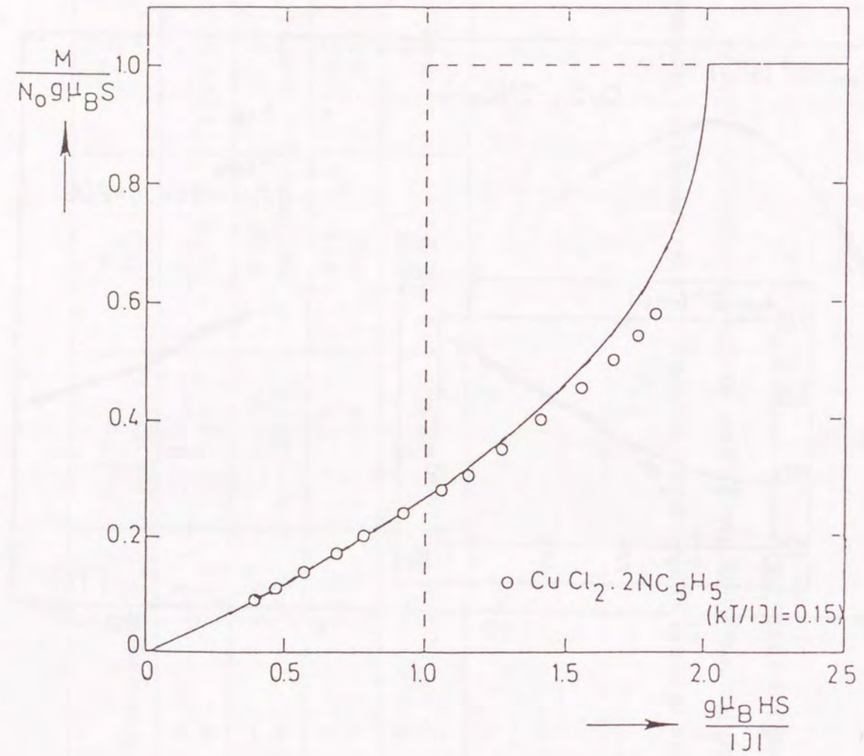


Fig. 1-1-2. Low temperature magnetization curve of the S=1/2 LCHA compound, $CuCl_2 \cdot 2NC_5H_5$, is compared with the theoretical result obtained by Griffiths[7] at T=0 K. The dashed curve shows the behavior expected for the Ising chain. (Quoted from ref. 26)

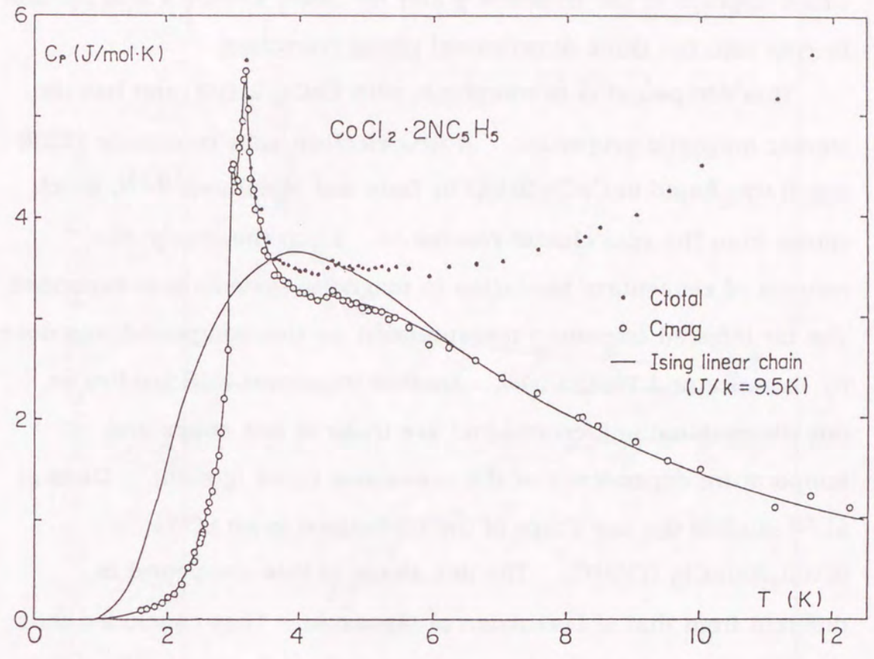


Fig. 1-1-3. Total specific heat (filled circle) of the ferromagnetic Ising chain $CoCl_2 \cdot 2NC_5H_5$ and its magnetic specific heat (open circle). The solid line shows the exact result for the magnetic specific heat of the Ising linear chain with J/k=9.5 K. (Quoted from ref. 29)

which appears in the Heisenberg and XY cases, becomes sharper and merges into the three dimensional phase transition.

This compound is isomorphous with $CoCl_2 \cdot 2H_2O$ and has the similar magnetic properties. A new electron spin resonance (ESR) signal was found in $CoCl_2 \cdot 2H_2O$ by Date and Motokawa[30,31], which comes from the spin cluster resonance. From this study, the concept of elementary excitation in magnetic systems was expanded. The far-infrared transition measurement on this compound was done by Torrance and Tinkham[32]. Another important ESR studies on one dimensional antiferromagnet are those of line shape and temperature dependence of the resonance fields (g-shift). Dietz et al.[33] studied the line shape of the ESR signal in an LCHA, $(CH_3)_4NMnCl_3$ (TMMC). The line shape of this compound is different from that of Lorentzian or Gaussian. They concluded that the line shape and its angular dependence were explained by a spin diffusion process. The g-shift at low temperatures in one dimensional antiferromagnets $CsMnCl_3 \cdot 2H_2O$ and TMMC was investigated experimentally and theoretically by Nagata and Tazuke[34] They satisfactorily explained the shift by taking into account the magnetic dipolar interaction in the short range ordered state. The result of comparison of the theory with the experiment in $CsMnCl_3 \cdot 2H_2O$ is shown in Fig. 1-1-4.

The result of the neutron scattering experiment in which the spin wave was measured on $CuCl_2 \cdot 2N(C_5D_5)$ by Endoh et al.[35] is shown in Fig. 1-1-5. The result agrees with the exact solution[20] of the spin wave state in an S=1/2 LCHA. As for non-linear excitation of one dimensional systems, there are some experimental

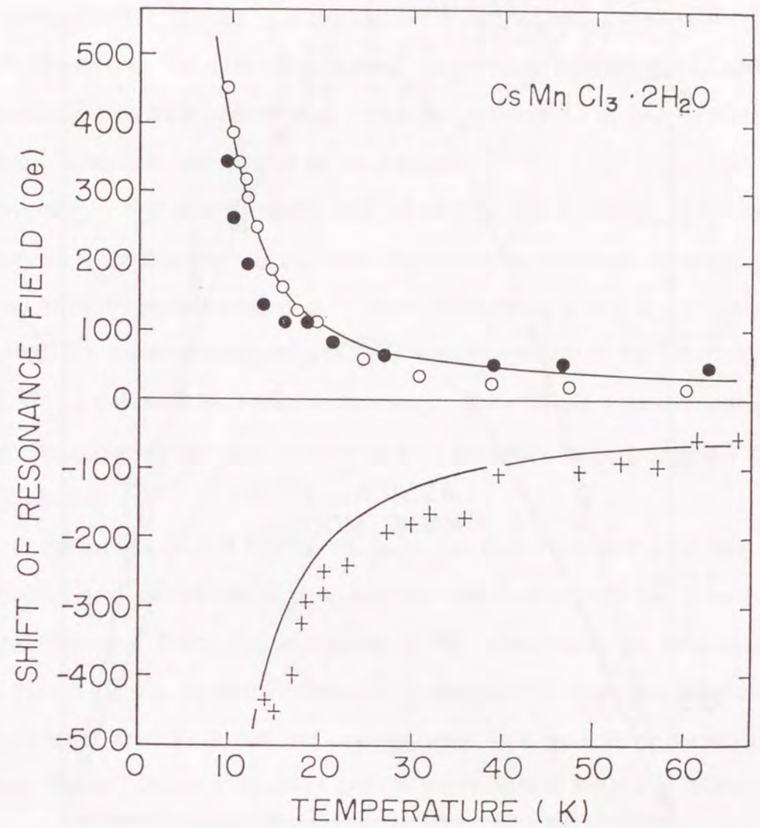


Fig. 1-1-4. Comparison of the theory with the experiment on the g-shift in the LCHA compound $CsMnCl_3 \cdot 2H_2O$ at 34.4 GHz. The measured values of the shift are indicated by +(H//a), ○(H//b) and ●(H//c). The solid curves are calculated by Nagata and Tazuke[34] (Quoted from ref. 34)

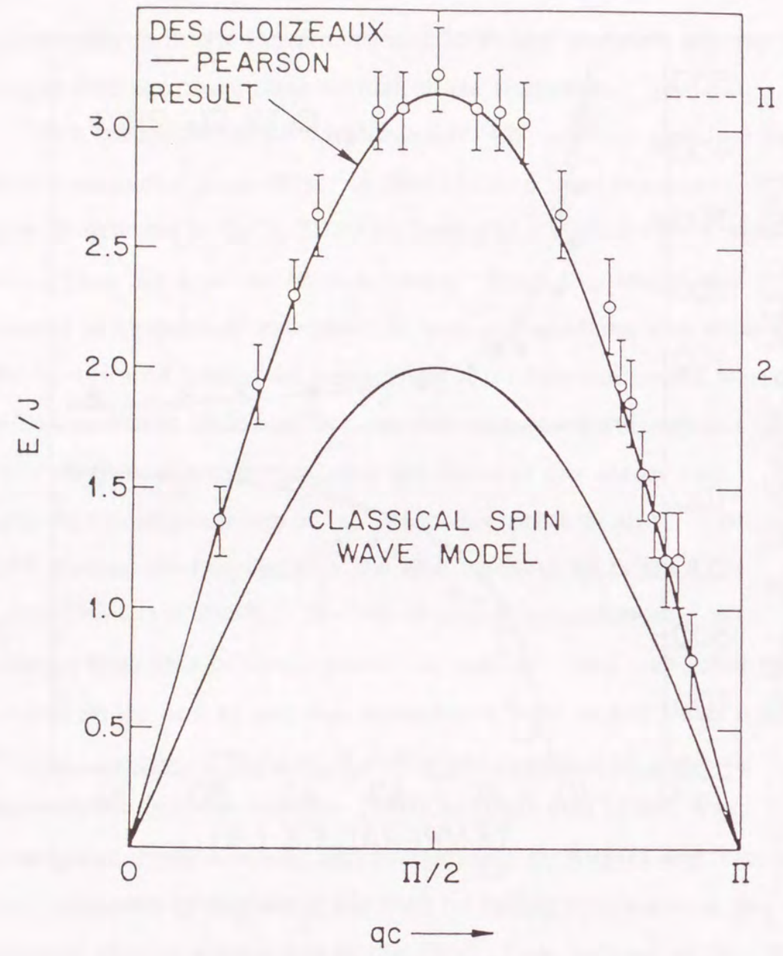


Fig. 1-1-5. Spin wave dispersion curve in the S=1/2 LCHA, $CuCl_2 \cdot 2N(C_5D_5)$ at 1.3 K. The energy is scaled in units of J=13.4 K. The solid lines represent the theoretical spin wave dispersion curves calculated by Des Cloizeaux and Pearson[20] and with classical model. (Quoted from ref. 35)

results[36-39]. Kjems and Steiner[36] found soliton mode predicted by Mikeska[22] in the one dimensional easy-plane ferromagnet $CsNiF_3$ by inelastic neutron scattering. The interpretation of the experimental data, however, was found to be incorrect[40-42]. The magnetic solitons in the one dimensional antiferromagnet $(CD_3)_4NMnCl_3$ were observed by Boucher et al. from the inelastic neutron scattering[37] and NMR[38] measurements. The dynamics in a one dimensional Ising like antiferromagnet $CsCoCl_3$ was investigated by Yoshizawa et al.[39] by inelastic neutron scattering. They found a propagative mode of one-dimensional antiferromagnetic domain walls predicted by Villain[24].

As for an S=1/2 LCHA, we have the exact solutions for the ground and spin wave states, and the physics is now fairly well understood. From the argument of the universality in spin systems, it was believed, before Haldane's conjecture[43], that the magnetic excitation spectrum did not change with spin quantum number, i. e., that there was no excitation gap at wave vector k=0 or π between the ground state and the first excited one in an LCHA, irrespective of spin values.

1-2. Haldane effect

In 1983, Haldane[43] found that the continuum field theory describing the low energy dynamics of a large-spin one-dimensional Heisenberg antiferromagnet is expressed by the O(3) non-linear sigma model. He predicted that the LCHA with integer spin values, even though the spin has a small number, has an excitation energy gap between the ground state and the first excited one and the exponentially decaying correlation functions, while the LCHA with half-integer spin values has no energy gap between them and the correlation function with power law decay. Since then, extensive theoretical[44-71] and experimental[72-94] works have been done to test the Haldane's conjecture.

Since the Bethe-ansatz is not applicable for an S=1 LCHA, numerical works have been carried out from the beginning of the study. These are, the exact diagonalization of finite chains[44,45], a finite-size scaling[46-52] and a variational[53], Monte Carlo[54-57] and other calculations[58-64]. Although there was a controversy[44,50,55] at the beginning of the numerical study, most calculations[45-49,51-54,56-64] have supported the Haldane's conjecture. The energy gap (Haldane gap) has been estimated to be $0.41\,|2J|$[52,54] (Fig. 1-2-1).

The phase diagram[47,49,59,63] using the Hamiltonian given by,

$$\mathcal{H} = \sum_i [\, -2J (S_i^x S_{i+1}^x + S_i^y S_{i+1}^y + \Delta S_i^z S_{i+1}^z) + D (S_i^z)^2 \,] \quad , \quad (1\text{-}2\text{-}1)$$

in the (Δ, D) plane is shown in Fig. 1-2-2. One of the most important results in this figure is that a singlet ground state phase

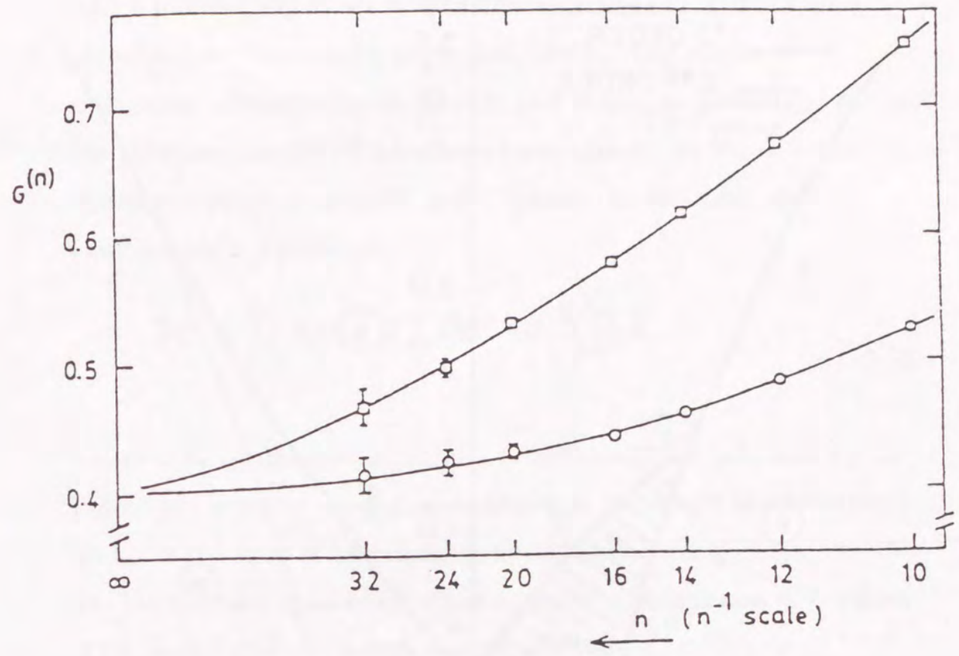


Fig. 1-2-1. Energy gaps in S=1 finite chain vs. n^{-1} (n is the number of spins) calculated by Nightingale and Blöte by using a Monte Carlo method. Open circles and squares give $(E_0\text{-}E_1)/J$ and $(E_0\text{-}E_2)/J$, respectively, where E_0 is the ground state energy and E_1 and E_2 the energy of the first and second lowest excited states, respectively. The curves are guides to the eye. (Quoted from ref. 54)

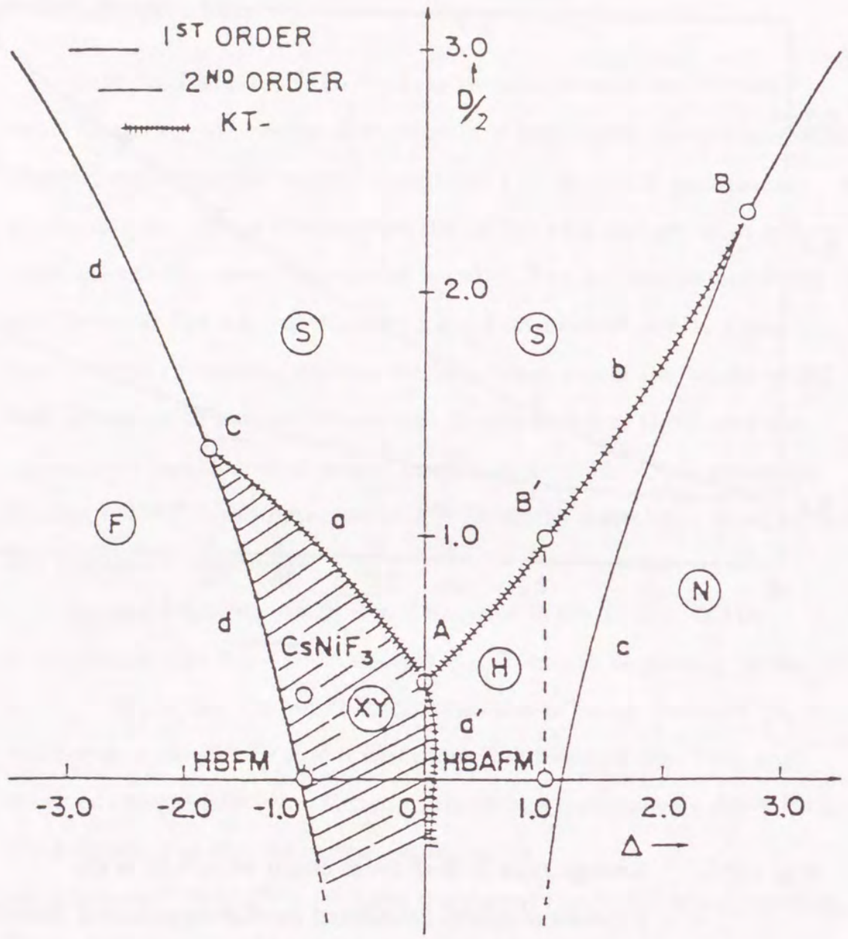


Fig. 1-2-2. Phase diagram obtained with the Hamiltonian (Eq. (1-2-1)). H : Haldane phase, S : disordered phase with the singlet ground state and the large single ion anisotropy, N : Neél ordered phase, XY : gapless XY phase, F : Ferromagnetic ordered phase. (Quoted from ref. 64)

with a nonzero gap exists in an extended range of Δ and D values including the Heisenberg point (Δ=1, D=0). The effects of interchain exchange interaction (J') and single ion anisotropy (D) on the Haldane phase[67-69] have been investigated. In Fig. 1-2-3 is shown the phase diagram[69] in D-J' plane. In this case, the Hamiltonian is written as,

$$\mathcal{H} = \sum_{<i,j>} \vec{S}_i \cdot \vec{S}_j + D \sum_j (S_j^z)^2 + J' \sum_{(i,j)} \vec{S}_i \cdot \vec{S}_j \quad , \qquad (1\text{-}2\text{-}2)$$

where <i,j> denotes an intrachain nearest-neighbor pair and (i,j) an interchain one, the second term describes the single ion anisotropy and J' is the ratio of interchain to intrachain coupling constants. We see the Haldane disordered phase exists in a wide region of D values if the interchain interaction is sufficiently small.

As to a rigorous work for a solvable model, Affleck et al.[65] studied an S=1 LCHA with a biquadratic term given by,

$$\mathcal{H} = -2J \sum_i \{ \vec{S}_i \cdot \vec{S}_{i+1} + \frac{1}{3} (\vec{S}_i \cdot \vec{S}_{i+1})^2 \} \quad , \qquad (1\text{-}2\text{-}3)$$

and proved that the system has a unique infinite volume ground state with a gap and exponentially decaying correlation functions. They provided the valence bond solid (VBS) state[65] as the exact ground state of this system. The VBS state is constructed out of valence bonds by extending the RVB state proposed by Anderson[9] to the case of S=1. Figure 1-2-4 (a) shows diagrammatically the S=1 VBS state. Spin one is obtained by symmetrization of two S=1/2

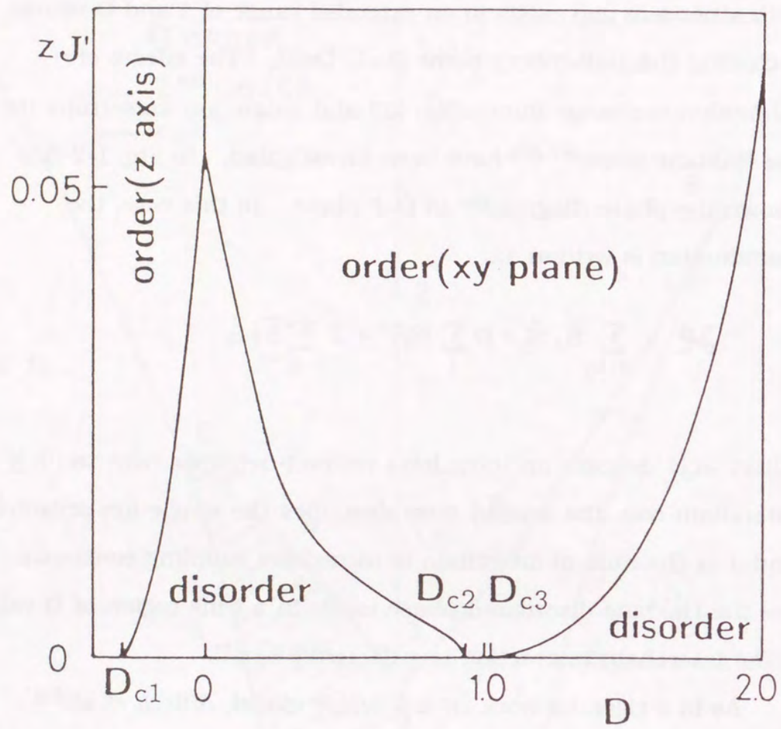


Fig. 1-2-3. Phase diagram in D-J' plane obtained with the Hamiltonian (Eq. (1-2-2)). Here, z is the number of adjacent chains. (Quoted from ref. 69)

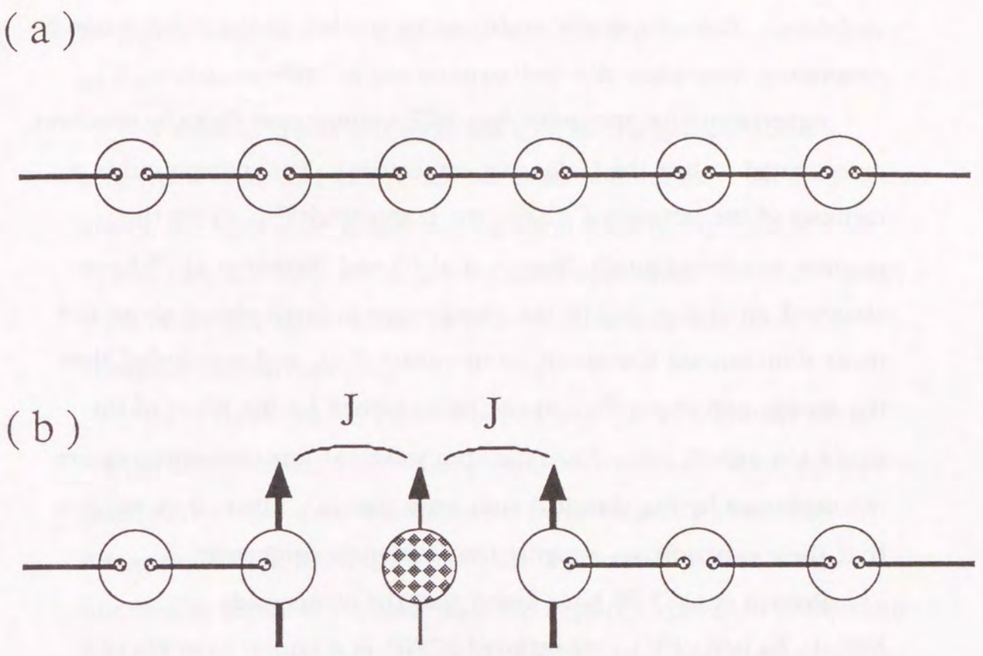


Fig. 1-2-4. (a) A schematic representation for the valence bond solid (VBS) ground state of an S=1 LCHA. The larger circles show the atomic sites and the smaller ones the S=1/2 variables. The lines represent the valence bonds.
(b) A host atom is substituted by an impurity resulting in the S=1/2 states at the host sites neighboring the impurity. The arrows show the spin moment.

variables. The spin singlet state can be written as the valence bonds emanating from each site and terminating on different sites.

Experimentally, the quasi S=1 LCHA compound $CsNiCl_3$ was first investigated to test the Haldane's conjecture. This compound is a member of the hexagonal ABX_3-type compounds[95]. From the neutron scattering study, Buyers et al.[72] and Steiner et al.[73] have observed an energy gap in the short-range-ordered phase above the three dimentional transition temperature (T_N), and concluded that the energy gap above T_N can not be explained by the effect of the single ion anisotropy. Also, the spin waves at low temperatures are not explained by the classical spin wave theory. Thus, they suggest that their experiments support the Haldane's conjecture.

Renard et al.[74-76] have found that the compound $Ni(C_2H_8N_2)_2NO_2ClO_4$, abbreviated NENP, is a typical example of a quasi S=1 LCHA. This compound is a better candidate for an S=1 LCHA than $CsNiCl_3$, because no three dimensional magnetic order exists down to 1.2 K[74], which makes the verification of the Haldane gap easy. A number of experiments[74-87] including susceptibility[74-76], neutron scattering[74-76], high field magnetization[78], electron spin resonance (ESR)[79-81], nuclear magnetic resonance (NMR)[82-86] and heat capacity[87] measurements have been carried out on this compound. The Haldane gap has been verified through these experiments. The results of these experiments are described in the next section. $Ni(C_3H_{10}N_2)_2NO_2ClO_4$ (NINO)[75], $AgVP_2S_6$[76], $(CH_3)_4NNi(NO_2)_3$ (TMNIN)[94] and $Ni(C_3H_{10}N_2)_2N_3ClO_4$ (NINAZ) have been also found

as typical examples of a quasi S=1 LCHA and have been investigated as well as NENP.

In spite of these experimental efforts, the ground state properties of an S=1 LCHA has not been understood. As is described above, the VBS state is the exact ground state of Eq. (1-2-3). We expect that the VBS model gives a good approximation to the ground state of an S=1 linear chain antiferromagnet with the quadratic exchange interaction only.

There has been no experiment to test the VBS ground state. We got the following idea. Let us consider the case when a host atom in the VBS state is substituted by an impurity atom, for instance, Ni^{2+} in NENP by Cu^{2+}. In this case, if the exchange interaction between the host and the impurity spins is considerably smaller than that between the host spins, the valence bonds will be broken at the impurity sites. This will results in producing S=1/2 states at the host spin sites neighboring the impurity (Fig. 1-2-4(b)). For the ordinary Heisenberg Hamiltonian, the effective coupling between these S=1/2 degrees of freedom at the two ends of a chain is of $O[(-1)^L(e^{-L/\xi})L^{-1/2}]$ where L is the chain length and $\xi \approx 7$ is the correlation length. Thus, open chain has low energy boundary excitations[70,71]. This S=1/2 degrees of freedom should be observed experimentally.

The format of this paper is the following. In § 2, the crystal and magnetic properties of NENP are described. The experimental procedure is explained in § 3. The experimental results of ESR on Cu doped NENP are reported in § 4. The ESR results are analyzed in § 5. The results of high field magnetization measurements on

NENP containing Cu impurity are discussed in § 6. In § 7, the experimental results and analysis on an imperfect single crystal of NENP without impurities are given. The final section (§ 8) is devoted to conclusions.

§ 2. Crystal and magnetic properties of $Ni(C_2H_8N_2)_2NO_2ClO_4$ (NENP)

2-1. Crystal structure of NENP

NENP crystallizes in the orthorhombic system and belongs to the Pnma space group[96]. The crystal structure of this compound is shown in Fig. 2-1-1. The lattice constants are a=15.223Å, b=10.300Å and c=8.295Å. The structure consists of $Ni(C_2H_8N_2)_2NO_2$ chains which are well separated from each other by ClO_4 anions. In the chains, NO_2 molecule is bonded to a Ni atom by its nitrogen atom (N-Ni=2.163Å) and to the next Ni atom by one of its oxygen atoms (Ni-O=2.183Å), and ····· Ni-NO_2-Ni ····· chains are directed along the b-axis. Each Ni atom is surrounded by four nitrogen atoms from two diamine molecules. The local stereochemistry of nickel is a distorted octahedron.

The 3d orbitals are divided into two kinds of orbitals ($d\varepsilon$,$d\gamma$) in the octahedoral field. The electronic configuration of the lowest orbital state of Ni^{2+} ion is $(d\varepsilon^6)d\gamma^2$ (that in parentheses indicate paired electron). Only the $d\gamma$-$p\sigma$ (provided from the anion like O^{2-}) bond can take part in the superexchange interaction. This gives rise to antiferromagnetic interaction for the case of the angle 180° between Ni^{2+} ions and the intervening anion[97,98]. The total spin of Ni^{2+} is one.

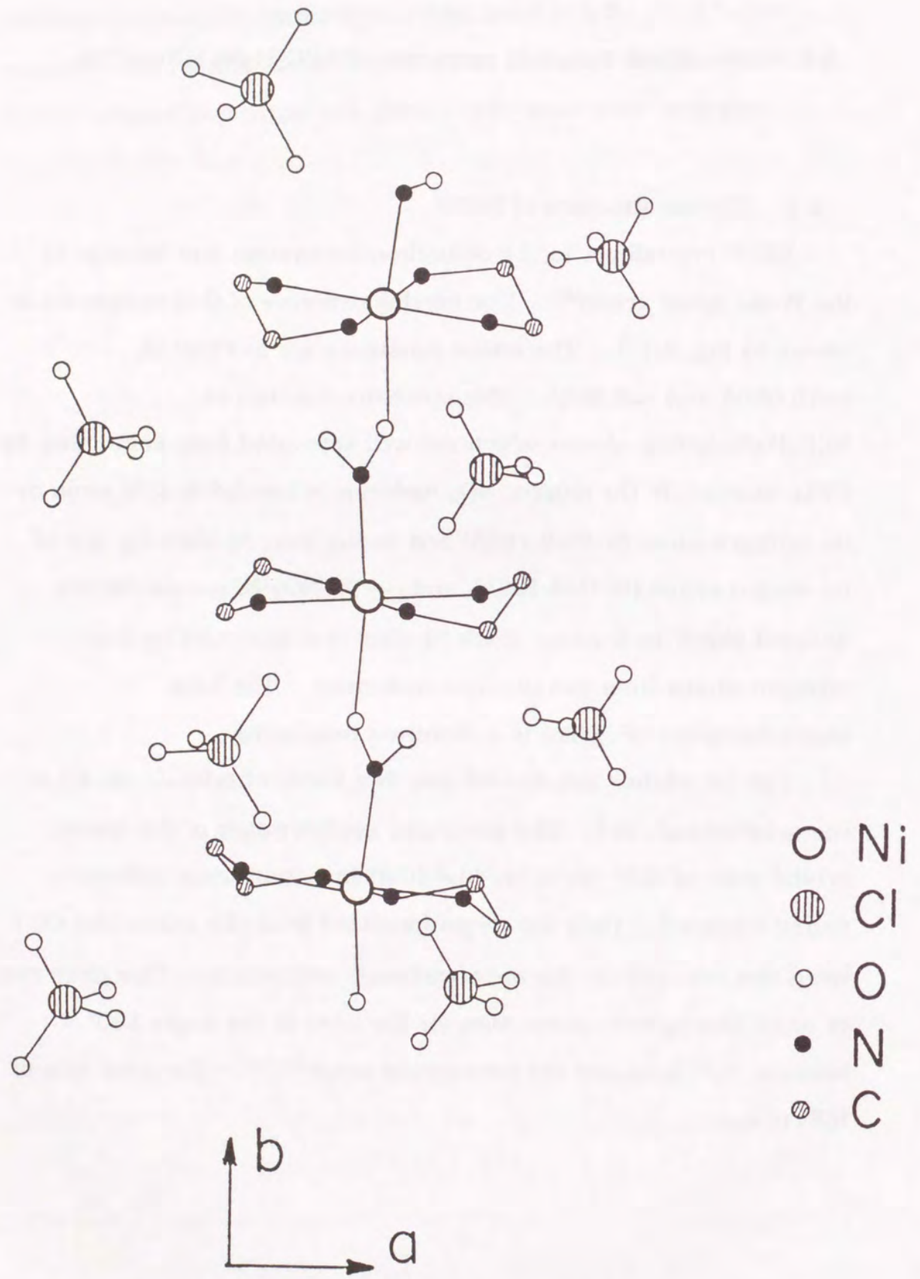


Fig. 2-1-1. Crystal structure of $Ni(C_2H_8N_2)_2NO_2ClO_4$ (NENP)

2-2. Magnetic properties of NENP

The molar magnetic susceptibilities (χ_M) of a single crystal of NENP along the three crystallographic axes show a rounded maximum around 60 K and decrease abruptly as the temperature is further decreased (Fig.2-2-1). This rounded maximum is typical of low dimensional antiferromagnets. The temperature at this maximum (T_{max}) is related to the intrachain exchange interaction as $T_{max} \cong 1.25|2J|/k_B$. The rapid decrease at the low temperature indicates the existence of an energy gap between a singlet ground state and the excited one. This temperature dependence of the susceptibility is completely different from that of an S=1/2 LCHA (see Fig. 1-1-1).

The intrachain exchange interaction constant (J) and the g-values along the crystallographic axes (g_a, g_b and g_c) are obtained by fitting the susceptibility data with the theory for an S=1 LCHA[96]. The value of the single ion anisotropy constant (D) is also estimated from the susceptibility data to be 0.9 K. In the other experiments[74-76,78-80], the D value is estimated to be about ten times larger than this. The magnetic parameters are listed in Table 2-2-1.

Renard et al.[74,75] have estimated the energy gap with the following relation:

$$\chi(T) = \chi(0) + C \times \exp(-E_G/k_BT), \qquad (2\text{-}2\text{-}1)$$

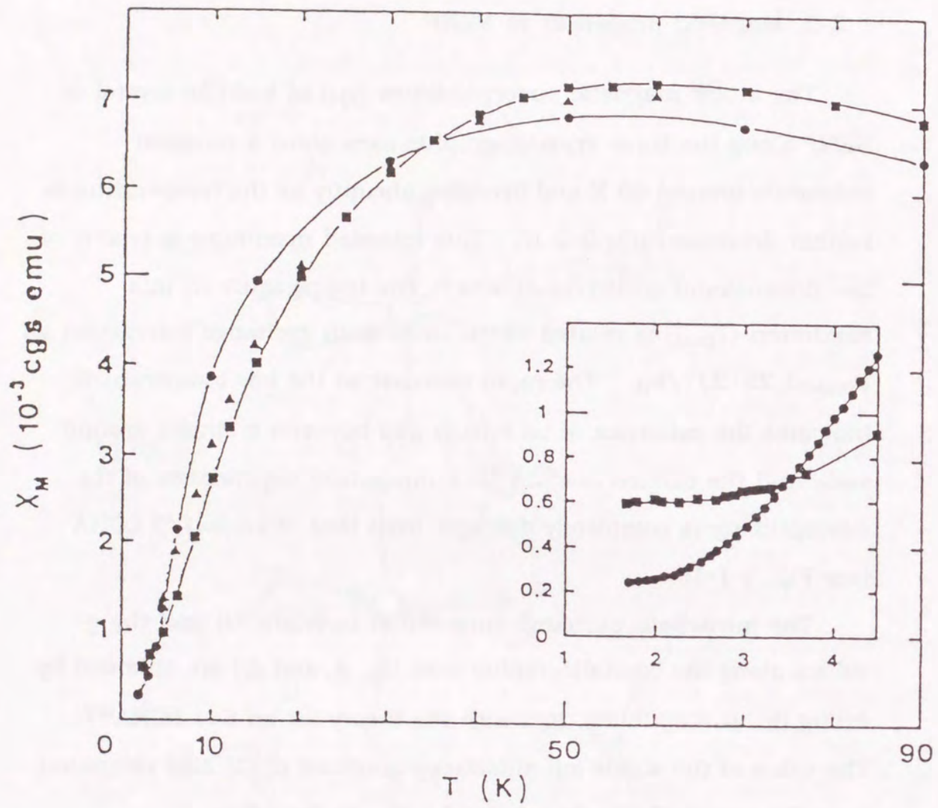


Fig. 2-2-1. Molar magnetic susceptibility of NENP along the three crystallographic axes a(■), b(●) and c(▲) as a function of temperature. The solid lines are guides to the eye. (Quoted from ref. 76)

Parameters	Values	References
g-values	ga= 2.21 gb= 2.15 gc= 2.23	96)
Intrachain exchange interaction constant (2J)	33 (cm^{-1})= 47.5 (K) 55 (K)	96) 74-76)
Interchain exchange interaction constant (J')	$\|J'/J\| = 4\times10^{-4}$	74-76)
Single ion anisotropy constant (D)	- 0.9 (K) - 12 (K) - 16 (K) - 11 (K) - 14 (K)	96) 74-76) 78) 79) 80)
Single ion anisotropy constant (E)	-0.92 (K) -0.72 (K)	79) 80)
Haldane gap energy (E_G)	19 (K) 17 (K) 13 (K) 17 (K) 11 (K) 19 (K)	74-76) 78) 79) 80) 86) 87)

Table 2-2-1. Magnetic parameters of NENP

where C is a constant and $\chi(0)$ is the susceptibility at zero temperature. This leads to $E_G^{//}/k_B$=11 K for H parallel to the chain axis and $E_G^{\perp}/k_B$=17 K for H perpendicular to it.

Inelastic neutron scattering measurements[74-76] have been carried out on this material in order to determine the energy gap directly. The dispersion curves of the magnetic excitations parallel and perpendicular to the chain axis are shown in Fig. 2-2-2. The experimental data near q=1 are well fitted by the relation,

$$\hbar\omega_q = [\,(E_G^{//,\perp})^2 + (2\pi\,|2J|\,S\,(1-q)^2\,]^{1/2}, \quad (2\text{-}2\text{-}2)$$

with $E_G^{//}$=2.6meV (30K), $E_G^{\perp}$=1.17meV (14 K) and $|2J|/k_B$=55 K, where q is the wave vector in reciprocal lattice units. The experimental data along the [100] direction can be fitted by a classical spin wave theory with $|J'/J|=4\times10^{-4}$. The value of the Haldane gap energy E_G estimated from $E_G^{//}$ and $E_G^{\perp}$ using the relation $E_G=(E_G^{//}+2E_G^{\perp})/3$ is 19 K, which is slightly smaller than that calculated ($0.41\,|2J|$ [52,54]).

A clear evidence for the existence of the Haldane gap has been obtained from the high field magnetization measurements by Katsumata et al[78]. The magnetization is very small in the low field region and begins to increase sharply at a finite field for all three crystallographic axes (Fig. 2-2-3). This result has been interpreted as follows : the energy of one of the excited triplet (S_z=-1) decreases with H and becomes equal to that of the singlet ground state at the transition field (H_T), and the system becomes magnetic. The energy

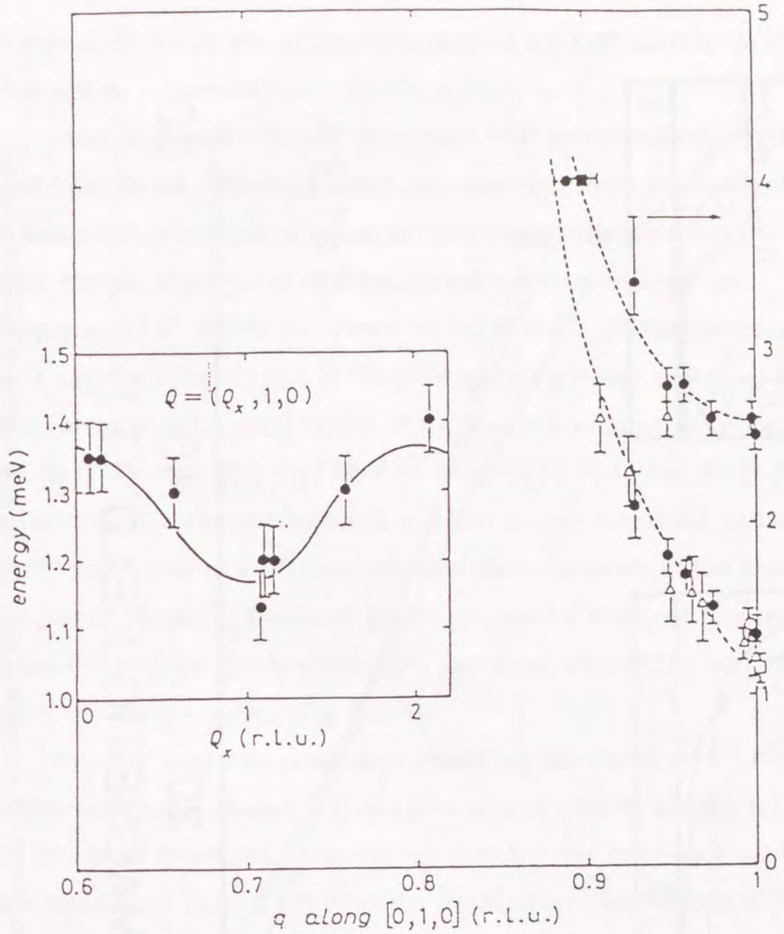


Fig. 2-2-2. Dispersion curves of the magnetic excitations in NENP parallel and perpendicular to the chain axis at 4.2 K. The dashed and solid lines are fits to the theory. (See text). Q=(Qx, q, 0). Qx : ○ 0.1, ■ 0.6, △ 1.1, ● 2.1, ❑ 3.1. (Quoted from ref. 74)

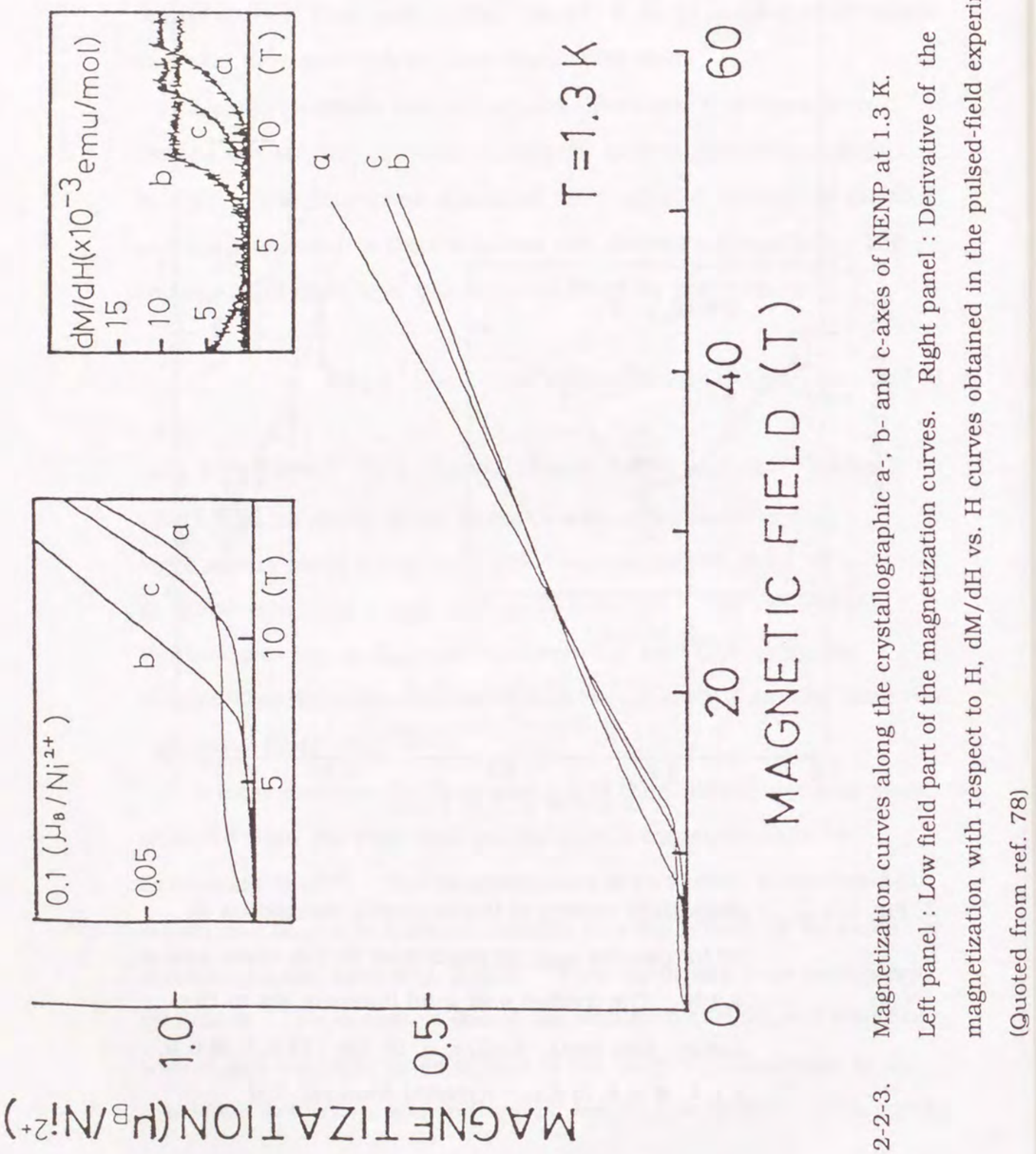


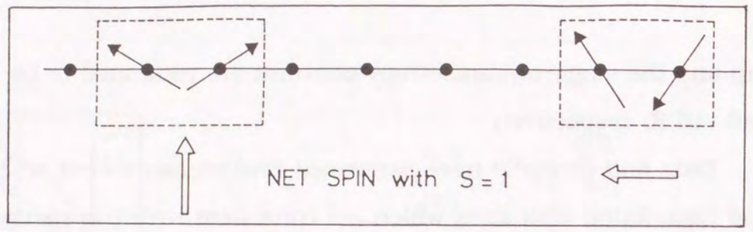
Fig. 2-2-3. Magnetization curves along the crystallographic a-, b- and c-axes of NENP at 1.3 K.
Left panel : Low field part of the magnetization curves. Right panel : Derivative of the magnetization with respect to H, dM/dH vs. H curves obtained in the pulsed-field experiment.
(Quoted from ref. 78)

gap and the single ion anisotropy constant are estimated to be 17 K and -16 K, respectively.

Date and Kindo[79] have performed ESR measurement on NENP and have found ESR lines which are consistent with the energy levels scheme obtained from the analysis of the magnetization data[78]. The ESR signals observed at the designated temperatures for the frequency of 47.0 GHz are shown in Fig. 2-2-4. The temperature and angular dependences of the ESR signals are well explained by the energy diagram, and values of the single ion anisotropy constants (D, E) and energy gap (E_G) have been obtained from this study (see Table 2-2-1). The energy levels scheme is also confirmed by Lu et al.[80] and Palme et al.[81] from the ESR measurements in the high frequency region. Date and Kindo proposed a localized two-spin bound state with the resultant spin one as an elementary excitation from the Haldane state (Fig. 2-2-4).

Nuclear magnetic resonance (NMR) measurements[83-86] on NENP have been carried out and proton spin lattice relaxation time T_1 has been measured. The energy gap (E_G) has been estimated by Fujiwara et al. to be 11 K from the temperature dependence of T_1.

Heat capacity measurements on NENP have been carried out in static magnetic fields up to 13 T by Kobayashi et al.[87]. They have obtained the value 19 K for the Haldane gap which agrees well with that obtained by inelastic neutron scattering experiments[74-76]. They also found that a non-zero gap exists at around the transition field (H_T) and concluded that a mixing between the ground and excited states exists.



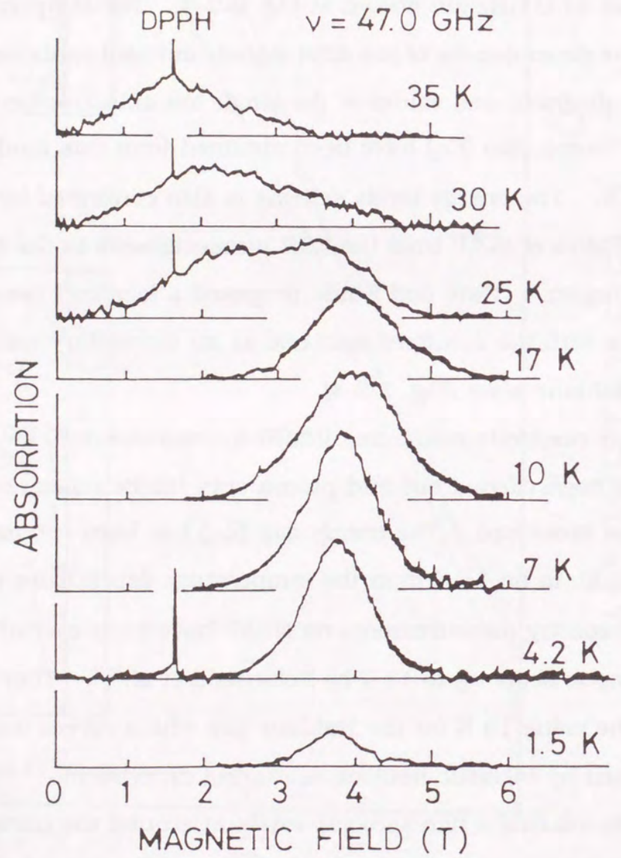


Fig. 2-2-4. Temperature dependence of the ESR signal in NENP. Upper panel : A model describing the elementary excitation in the Haldane state. (Quoted from ref. 79)

Renard et al.[76] have measured the susceptibilities of 3.6 at% Cu : NENP and 6.2 at% Cu : NENP (Fig. 2-2-5). The impurity contribution is well fitted by the Curie law. The experimental Curie constants are about 4.6 times larger than the calculated ones for free Cu^{2+} impurities. Recently, the susceptibility data are re-analyzed by Affleck[99]. He found that the Curie constant lies between 3.2 and 4.4 depending on field direction.

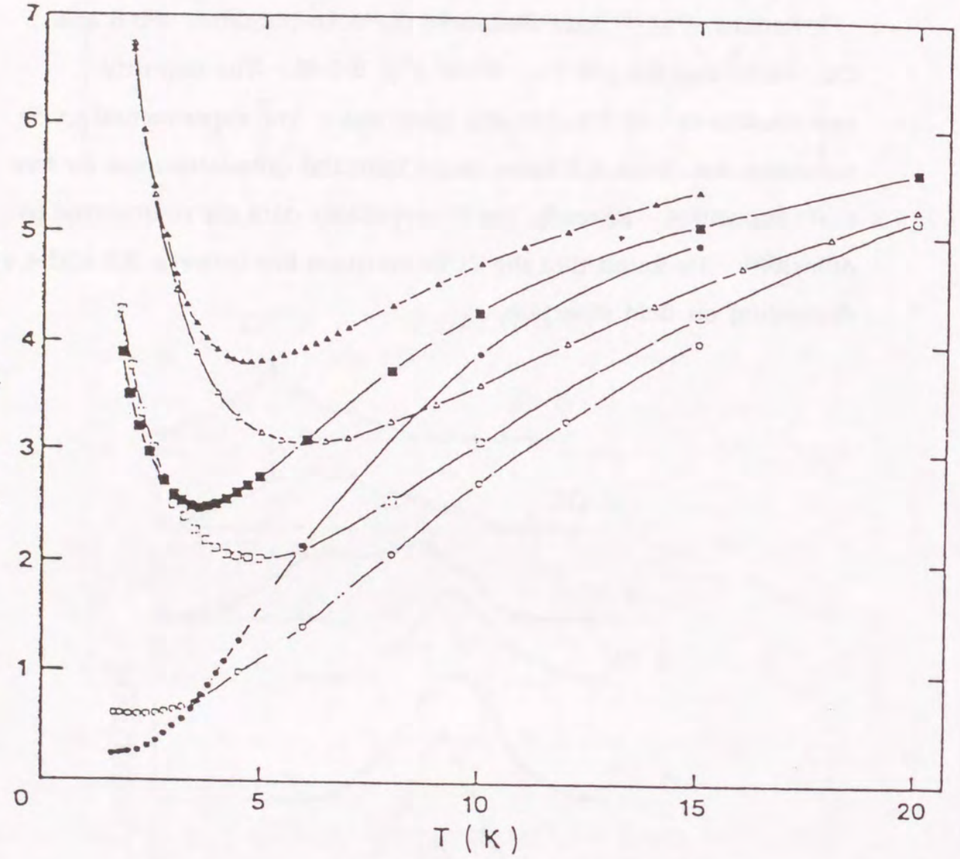


Fig. 2-2-5. Molar magnetic susceptibilities of NENP doped with Cu and pure NENP. Pure NENP : a-axis (○), b-axis (●) ; NENP : Cu 0.36at% : a-axis (□), b-axis (■) ; NENP : Cu 0.62at% : a-axis (△), b-axis (▲). (Quoted from ref. 76)

§ 3. Experimental procedure

3-1. Sample preparation

Single crystals of NENP were grown from an aqueous solution containing stoichiometric amounts of $Ni(ClO_4)_2 \cdot 6H_2O$, $(C_2H_8N_2)_2$ and $NaNO_2$ at room temperature (~20 °C) [96]. Single crystals up to 3mm×3mm×10mm were grown in about one month. The single crystals used in some ESR (0.7 at% Cu : NENP) and high field magnetization measurements were made by Prof. J. P. Renard in the Institut d'Electronique Fondamentale, Univesité Paris-Sud. The others (0.1 at% Cu : NENP, undoped NENP) were made by the author.

The crystal of NENP has the nature of cleavage which is used to determine the crystal axes. In NENP, bc-plane is parallel to the cleavage plane and the long axis of the crystal corresponds to the b-axis. The directions of the crystals used in the experiments were confirmed by an X-ray at room temperature. Chemical analysis was done by an Inductively Coupled Plasma (ICP) method and the sensitivity of this method is 0.001~0.01 wt% for Cu.

3-2. Electron spin resonance (ESR) measurement

The ESR experiments were performed by using X-band spectrometer of JOEL JES-FE3AX system (Fig. 3-2-1) and K-band spectrometer constructed by the author (Fig. 3-2-2).

3-2-1. X-band ESR Spectrometer

The JES-FE3AX system is composed of the following units.

1 an electronic console
2 a microwave unit
3 a sample cavity with connecting wave guide
4 a magnet and a magnet power supply

The electronic console consists of the following modules and assembles : The magnetic field scanning unit provides direct field control (maximum field 13500 Oe) and regulation of the magnetic field. The 100 kHz and 80 Hz unit provides magnetic field modulation with the frequency of 100 kHz or 80 Hz (modulation width 0.002~20 Oe), gain of the amplifier and response time etc.. The oscilloscope displays ESR signals for observation and is used for tuning of the spectrometer. The X-Y recorder displays ESR spectrum as a function of magnetic field or time.

The microwave unit consists of the following modules and assembles : The microwave bridge supplies the microwave power with the frequency ranging from 8.8 GHz to 9.6 GHz, which is generated by a Gunn-effect oscillator, to the cavity and detects ESR signals. The detection method is of the homodine crystal type. The reference arm design permits operation at the microwave power

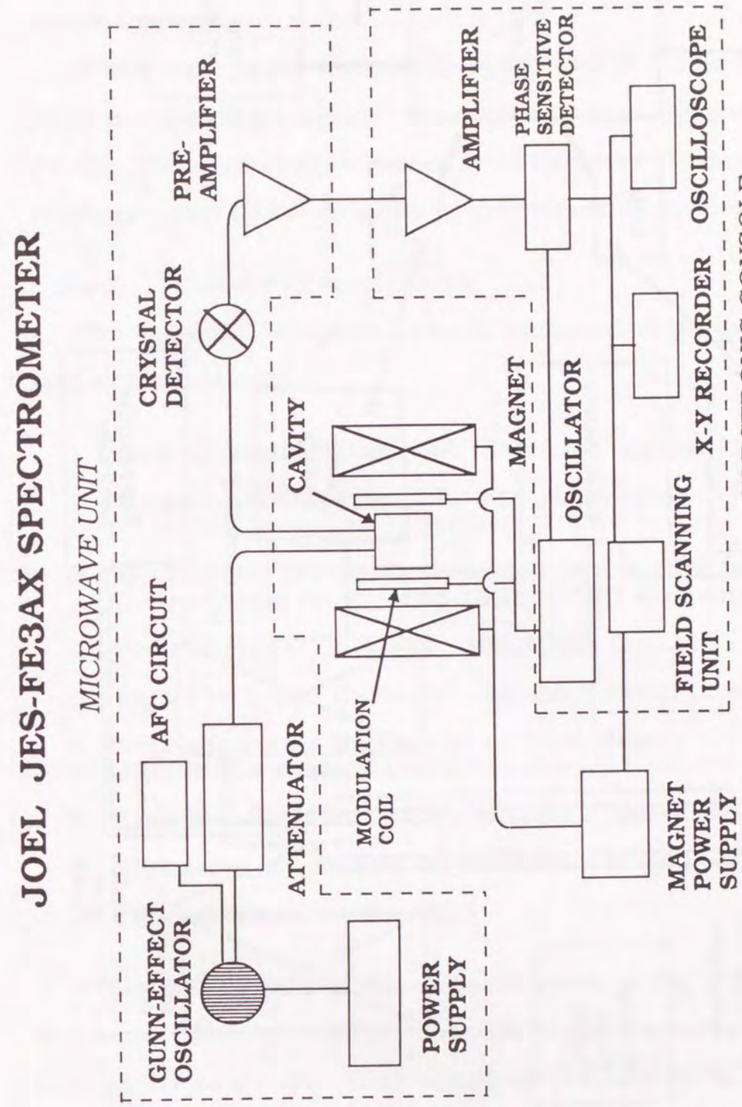


Fig. 3-2-1. Block diagram of the X-band ESR spectrometer.

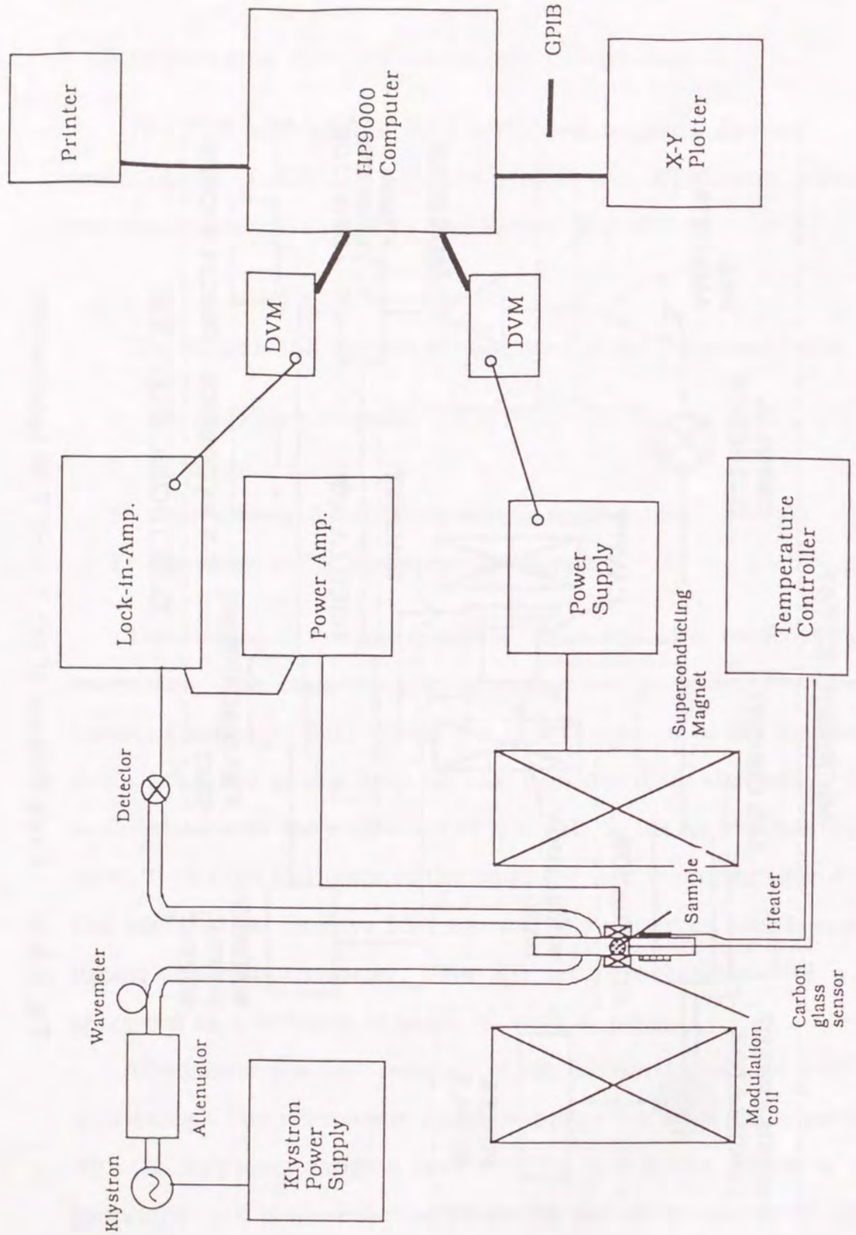


Fig. 3-2-2. Block diagram of the K-band ESR spectrometer.

levels to 0.1 microwatt. The automatic frequency control (AFC) circuit, pre-amplifier and Gunn-effect oscillator power supply are built in this unit.

The sample cavity is a cylindrical one with TE_{011} mode. The cavity is designed for the use above liquid nitrogen temperature (77 K). The electromagnet has a gap of 75 mm. The magnet power supply provides 13 kW dc power to the magnet.

3-2-2. K-band ESR spectrometer

The K-band ESR spectrometer is composed of the following apparatuses and units.

1 Lock-in-Amplifier (PAR124A : Princeton Applied Research)

2 Temperature Controller (DRC-91A : Lake Shore Cryotronics, Inc.)

3 Klystron (20V10 : OKI Ceramic Industry Co.,Ltd.) and Klystron Power Supply (EKS-7600 : ECHO electronics Co.,Ltd.)

4 Power Amplifier (BPA186A : METRONIX Co.,Ltd.)

5 Digital Voltmeter (HP3478A : Hewlett Packard Company)

6 Superconducting Magnet and its Power Supply (OXFORD Instruments Ltd.)

7 Computer (HP9000-360CH : Yokogawa-Hewlett-Packard Ltd.)

8 Microwave components (Micro Device Co.,Ltd.)

9 Cryostat (Made by the author)

The block diagram of this system is shown in Fig. 3-2-2. The microwave power generated by the Klystron goes into the cavity through the wave guide. ESR signals are detected by the crystal diode detector and fed to the Lock-in-Amplifier. The output signal after phase sensitive detection is transferred to the computer

through the digital voltmeter via the GPIB interface. A modulation field is applied to a sample by a small coil attached to the cavity.

The cryomagnetic system consists of a superconducting solenoid which produces a vertical magnetic field centered at a sample position. The range of a static magnetic field generated with the superconducting magnet is from 0 T to 12.5 T. The strength of the magnetic field is measured by reading the value of the current fed to the superconducting solenoid. The temperature of the sample can be set between 1.5 K and 300 K. The program for the ESR measurement was written by the author. The ESR signals are plotted out on the XY plotter.

3-2-3. Detection of ESR signals

In both of the X- and K-band spectrometers, the ESR sample in the cavity is irradiated with microwave energy from the Gunn-effect oscillator or the Klystron-oscillator. At resonance fields, a change of the loaded Q value occurs for a fixed microwave frequency. The microwave energy change at the resonance fields is detected by the crystal detector. After detection at the crystal, the field modulated signal containing the ESR information is amplified, and is phase-detected to obtain the ESR spectrum.

3-2-4. X-band ESR cryostat

A cryostat with the rectangular resonant cavity (TE_{102} mode) is used at X-band measurement. The temperature between 1.6 K and 4.2 K can be obtained by reducing the vapor pressure of liquid helium. The temperature above 4.2 K can be obtained by the temperature control unit with the two heaters. The low

temperature apparatus consists of two Dewar's vessels, a cap and a support (Fig. 3-2-3). Each Dewar has an unsilvered strip window along its length for nitrogen and helium level observation. The cap provides a vacuum tight seal at the top of the inner Dewar. The cryostat flange is screwed on the cap and an O-ring seal is used. A mica plate and an O-ring are used to seal the top of the wave guide.

3-2-5. Temperature control system

The temperature control system shown in Fig. 3-2-4 is used above 4.2 K. The apparatus consists of a carbon-glass resistance thermometer, two heaters (R_a and R_b), a current power supply and DRC-91C temperature controller (Lake Shore Cryotronics,Inc.). The temperature is controlled with the following manner. The temperature can be read directly in the temperature range between 1.5 K and 100 K by the DRC-91C controller. The temperature of the sample is controlled automatically either by heating the sample by R_a or cooling it by cold helium vapor boiled with heater R_b. The output current to the heater R_a is controlled with a PID (Proportional, Integral and Derivative) manner. In this way, the temperature is kept within 0.1 K.

Similarly, temperature above liquid nitrogen can be obtained by using liquid nitrogen instead of liquid helium. The sample is glued to the cavity by Apiezon N grease or high vacuum grease to keep a good thermal contact. The wires from the thermometer and the heaters are connected to a hermetic seal connecter at the cryostat flange (Fig. 3-2-3).

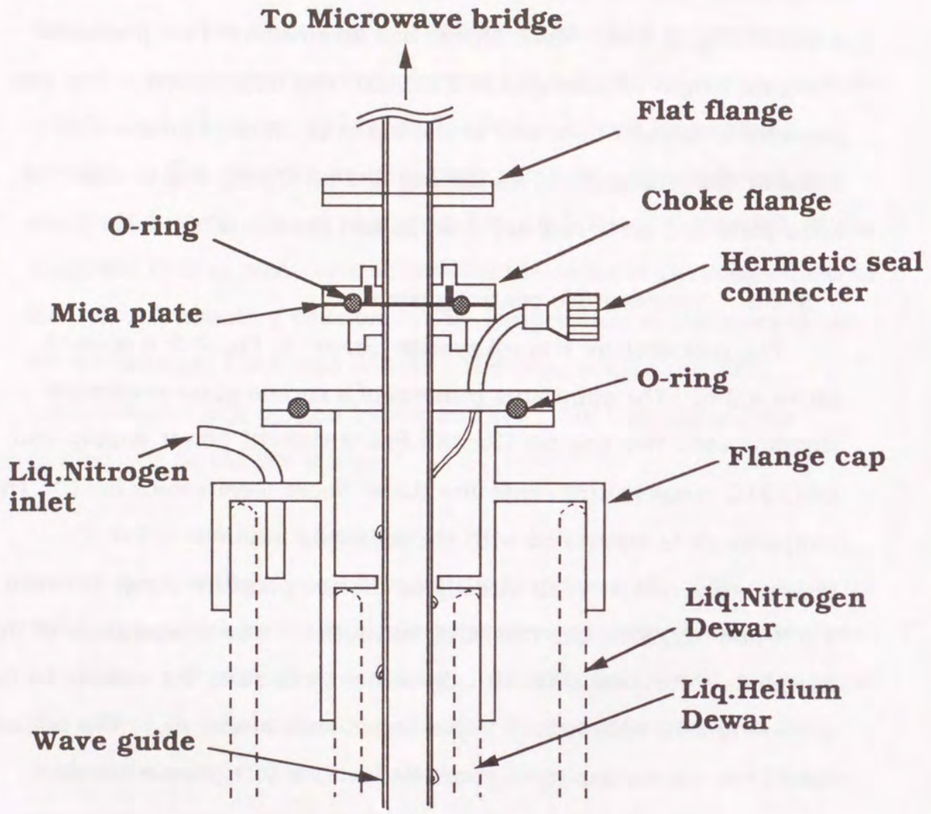


Fig. 3-2-3. Cut view of the cryostat flange and the Dewar cap (X-band).

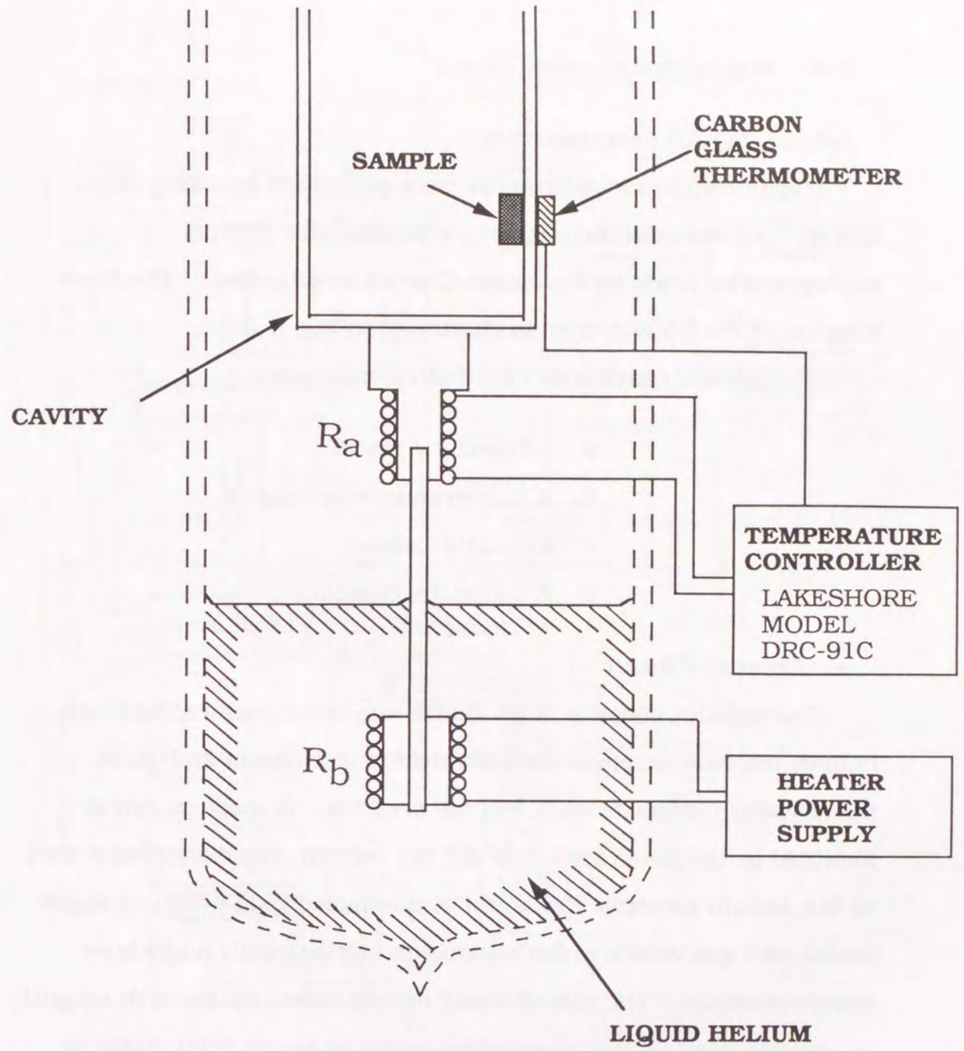


Fig. 3-2-4. A schematic diagram of the temperature control system for the X-band ESR spectrometer. R_a is used as a heater to warm the sample and R_b is a heater for vaporizing liquid helium.

3-3. Magnetization measurement

3-3-1. SQUID susceptometer

Magnetization measurements were performed by using S600 SQUID (Superconducting QUantum Interference Device) susceptometer made by Cryogenic Consultants Limited. The block diagram of the S600 system is illustrated in Fig. 3-3-1.

This system consists of four main components.

a A Cryostat / Insert

b A Superconducting magnet

c A Control Cabinet

d A Computer System

a. Cryostat / Insert

The cryostat consists of an aluminium outer shell containing a helium reservoir constructed from welded aluminium and glass fiber/ epoxy composite neck and tail sections. A niobium can is mounted in the lower section of the tail section. Radiation heat load to the helium reservoir (35 liters) is minimized using both nitrogen cooled and gas cooled radiation shields together with multi-layer superinsulation. The rate of liquid helium consumption with magnet in persistent mode and variable temperature insert (VTI) stable is 3 liters/day. The cryostat is surrounded by a single Mu-metal shield which reduces the ambient field within the helium reservoir to a few micro-Tesla. The temperature at sample position ranges from 1.7 K to 325 K, and the temperature accuracy of sample is 0.5 multiplied T (K) %. The temperature uniformity over sample

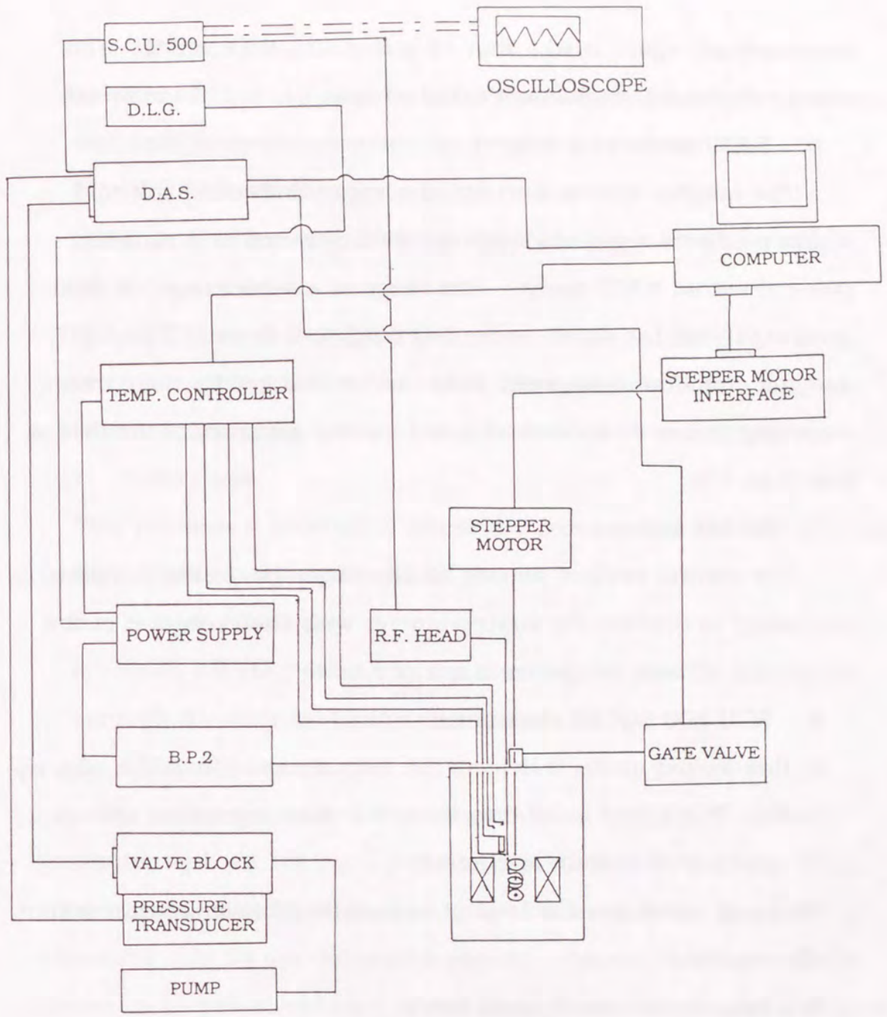


Fig. 3-3-1. Block diagram of the S600 SQUID susceptometer.

measurement space is ±0.1 K at 10 K and ±0.5 K at 325 K. The sample transport mechanism is bolted onto the top of the insert.

b. Superconducting magnet

The magnet system consists of a superconducting solenoid which produces a vertical magnetic field centered at a sample position within a VTI space. The range of a static magnetic field generated with the superconducting magnet is from 0 T to 6.5 T, and the direction of magnetic field can be changed by the current switching unit. Field resolution is 1 Oe and accuracy of the field is less than 1 %.

c. Control Cabinet

The control cabinet houses all the major electronic components necessary to operate the susceptometer with the exception of the computer. These components are as follows :

1. SCU 500 SQUID electronics

In flux-locked mode, it detects the output signal from the pick up coils. This signal is fed directly to the data acquisition system.

2. DLG 2000 Helium level meter

This unit measures the level of helium liquid in millimeter within the cryostat.

3. Data Acquisition System (DAS)

It is used to control all analogue and digital inputs/outputs to the system hardware with the exception of the power supply and temperature controller.

4. Temperature Controller

Lakeshore DRC91C model temperature controller which monitors two independent thermometers located within the VTI.

5. PS80C Power Supply

Superconducting magnet power supply is capable of delivering 80 amps at 5 volts.

6. BP2 Current Switching Unit

It allows current sense reversal in the superconducting magnet which is necessary when making hysteresis measurements.

7. Valve Block

This contains a network of solenoid valves used in the operation of the variable temperature insert.

8. Pumping Station

It houses a 2-stage rotary vane pump to draw gaseous helium through the variable temperature insert.

d. Computer System

The computer control system comprises an EPSON Ax3 computer with 40 MB hard disk and 1.2 MB 5 and 1/4" disk drive, monochrome monitor with video graphics array (VGA) graphics capability and 24 pin dot matrix printer. An associated peripheral device to be positioned next to the computer is the sample transport power supply.

3-3-2. Method of signal detection[100]

A schematic view of SQUID detection is shown in Fig. 3-3-2. When a sample passes through the second order gradiometer pick-up coil, the signal is picked up with the coil. This pick-up coil is connected to the input coil which couples mutual-inductively to a

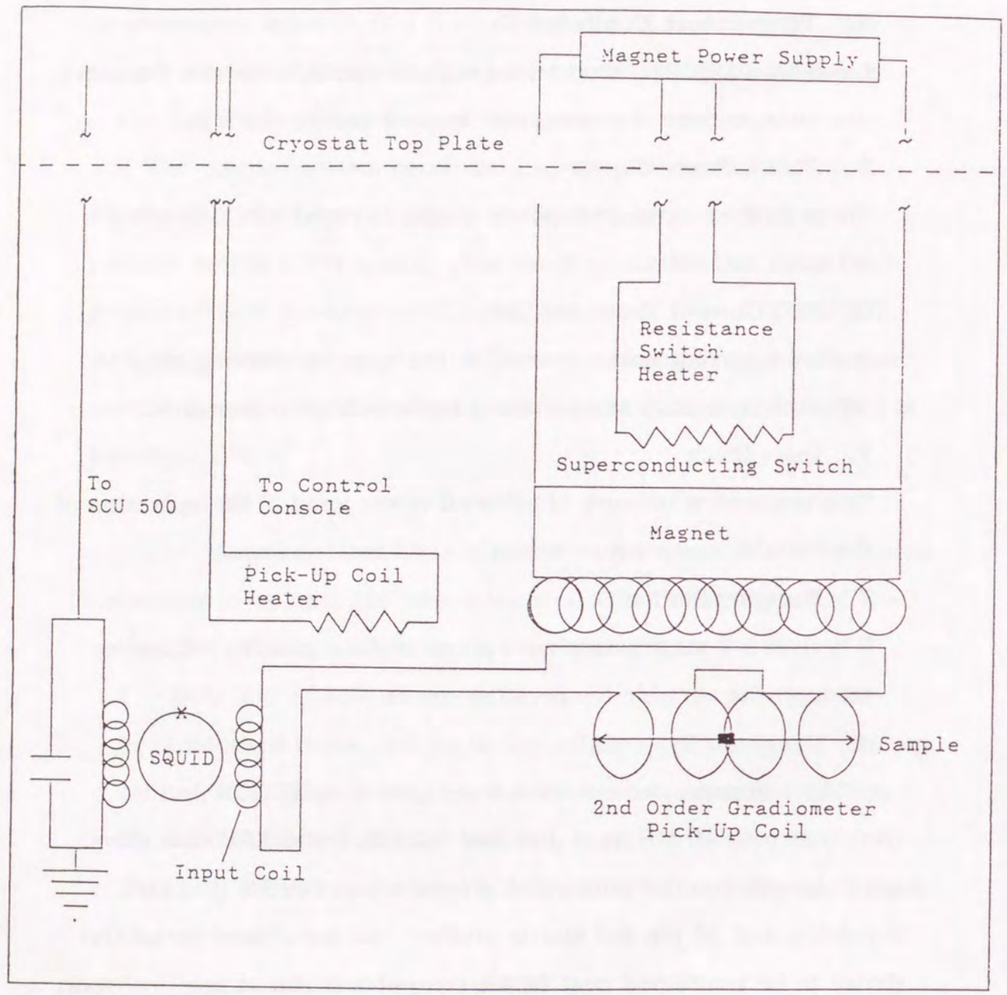


Fig. 3-3-2. Schematic view of SQUID detection and magnet circuitry

superconducting ring with a Josephson junction that is used for measurement of magnetic flux with the sensitivity approaching 10^{-11} gauss·cm^2. The output voltage via a resonant circuit, which couples inductively to the ring and is driven by an rf bias (20 MHz), is amplified and then detected with SCU 500 SQUID electronics. Magnetic moment sensitivity is 10^{-8} emu and dynamic range lies from $\pm10^{-7}$ to 10^{-1} emu. The absolute value of magnetization was calibrated by using a single crystal of $Fe(NH_4)(SO_4)_2 \cdot 12H_2O$. Pick-up coil heater is used to reduce remanent magnetic flux in the pick-up coil before detecting signal.

3-4. High field magnetization measurement

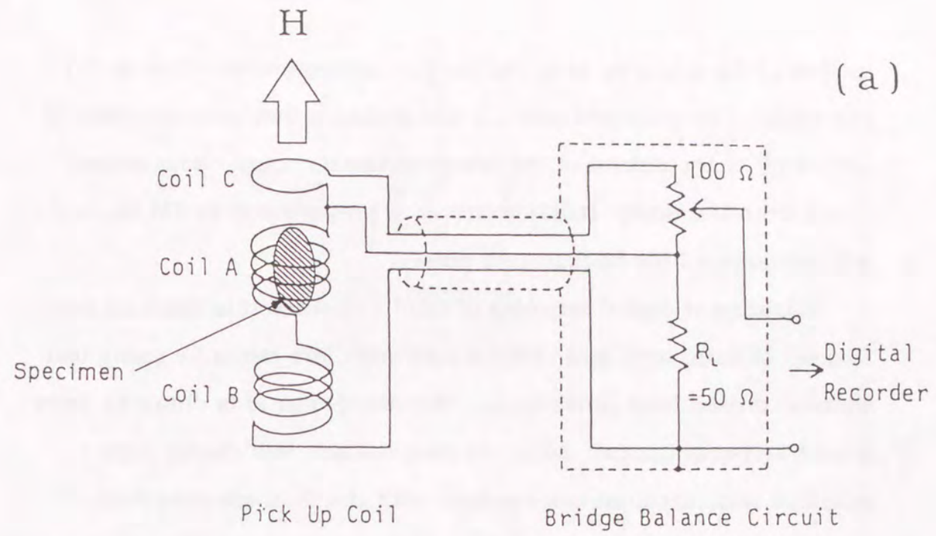
3-4-1. Magnet system

The high field magnetization measurement was carried out at the High Magnetic Field Laboratory of Research Center for Extreme Materials, Osaka University. The D-2 magnet system with the 1.25 MJ capacitor bank was used in this work. A two layered magnet 150(2L)20 was used, which can produce fields up to 700 kOe with the pulse width of 0.4 msec within 18 mm inner diameter. The magnetic field is monitored by a field pick-up coil and recorded in a digital recorder.

3-4-2. Method of magnetization measurement[101)]

The magnetization is measured by using a balanced pick-up coil system. The technique of reducing the background flux change due to a transient field, which is usually 10^4~10^6 times larger than the flux change caused by the magnetization of the specimen, is shown schematically in Fig. 3-4-1 (a). The A-coil picks up the magnetic flux changes of the specimen and the external field while the B-coil is wound oppositely to the A-coil in order to compensate the background flux change. A fine adjustment is established with the one turn C-coil.

Figure 3-4-1(b) is a cut view of the standard pick-up coil which has been used in this laboratory. Considering the field duration and frequency response, the A-coil is wound with 80 turns on a 3.0 mm diameter bakelite pipe. The B-coil is wound with 40 turns coaxially on the A-coil in opposite direction to the A-coil and the C-coil with 1 turn on the B-coil. The cross section of the B-coil is twice as large



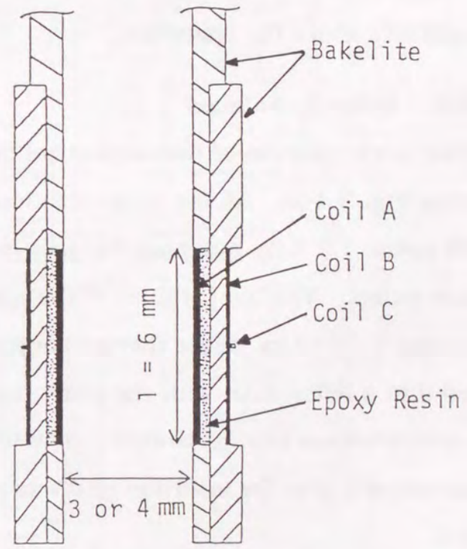


Fig. 3-4-1. (a) Pick-up coils and the method of magnetic flux compensation (b) Cut view of the standard pick-up coil. (Quoted from ref. 101)

as that of the A-coil so as to receive the same amount of flux in the two coils. The standard pick-up coil attains a flux compensation of 10^{-4}~10^{-5} at the output of the bridge balance circuit. The output signal from the bridge balance circuit is proportional to dM/dt, but still contains a little background noise.

A transient digital recorder is used to reduce this residual noise. Two set of data, with and without specimen, are taken by using two shots of pulsed field generation. The dM/dt signal is obtained from a subtraction of the two data. In this manner, sufficiently high sensitive measurement can be done with the final effective flux compensation of 10^{-6}. The field and magnetization pick-up coils were calibrated by a single crystal of MnF_2 as the standard specimen using the known values of the spin-flop transition field and the susceptibility above the transition.

3-4-3. Other techniques

The block diagram of the magnetization measurement system is shown in Fig. 3-4-2. All the magnetization measurements were carried out at 1.3 K by pumping ^{4}He in a quartz dewar connected to a vacuum pump. The temperature of the specimen was monitored by a gold-iron (0.07%) vs. silver thermo-couple. The specimen was located into a teflon tube with the inner diameter of 2.4 mm and was fixed with alumina (Al_2O_3) powder. The teflon tube was mounted on the bottom of a pipe for insertion and was adjusted at the right position.

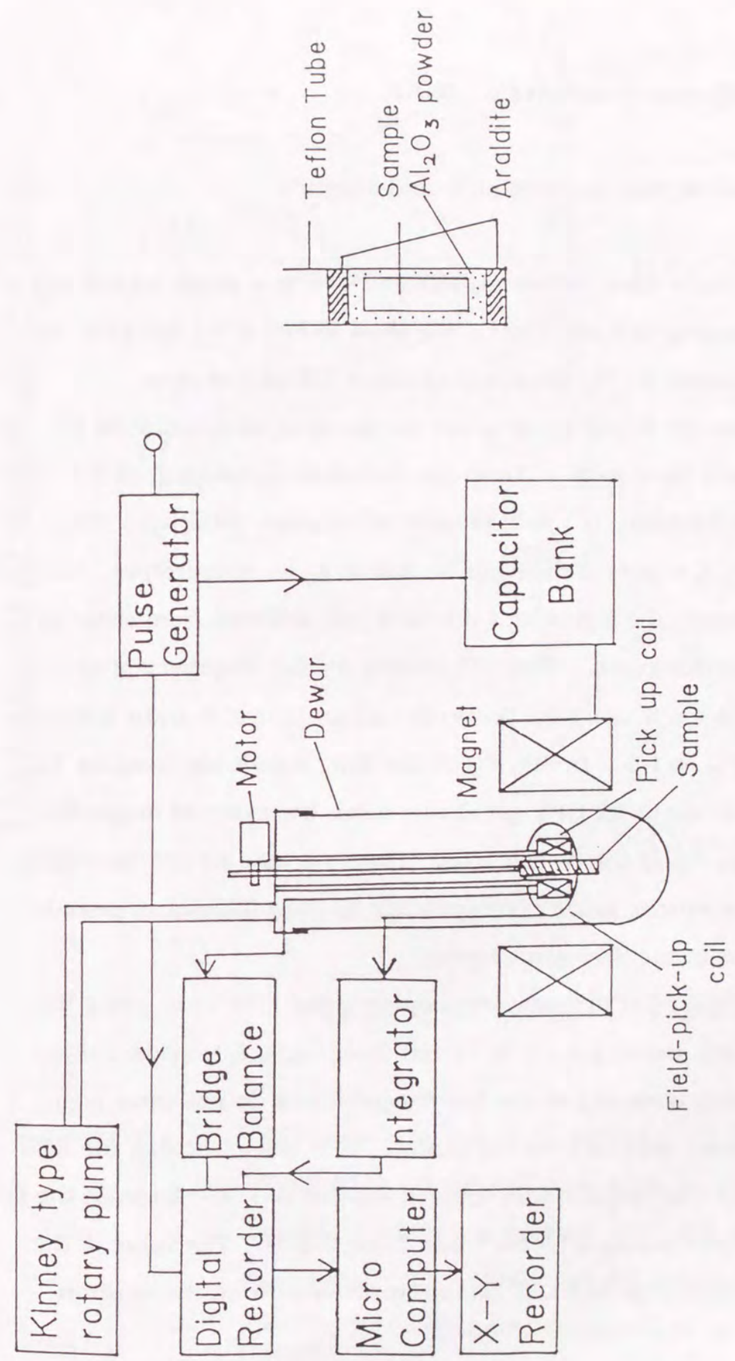


Fig. 3-4-2. Block diagram of the high field magnetization measurement system. The way of setting the sample is illustrated on the right side. (Quoted from ref. 102)

§ 4. ESR experiment on Cu : NENP

4-1. ESR signals observed at X- and K-bands

The sample used in this experiment[88,89] is a single crystal of NENP containing 0.7 at% Cu^{2+}. We show in Fig. 4-1-1 the ESR signals obtained for the frequency of about 9.5 GHz at room temperature, 77 K and 4.2 K when the external magnetic field is applied along the c axis. These are derivative signals ($d\chi''/dH$) of the absorption intensity (χ'') with respect to magnetic field (H). The signal at 77 K is almost the same as that at room temperature. On the other hand, the signal at 4.2 K is largely different from those at the high temperatures. The ESR signals for the frequency of about 9.25 GHz at 4.2 K along the three crystallographic a, b and c axes are shown in Fig. 4-1-2. In Fig. 4-1-3, the ESR signals observed for the frequency of about 22 GHz are shown when the external magnetic fields is applied to the b- or c-axis. Here, we take for the resonance fields the magnetic fields corresponding to the midpoint of peak-to-peak height in the derivative curves.

The g values of the rightmost and leftmost ESR lines along the b- and c-axes are far from 2.0. From these facts, it is evident that the ESR lines observed at the low temperatures do not come from free Cu^{2+} ions isolated from the chains. It is also clear that the ESR signal is not due to Cu^{2+} spin coupled with an S=1 Ni^{2+} because the D value of NENP is about 10 cm^{-1} (see Table 2-2-1). The value of the Haldane gap energy in NENP has been obtained from the neutron

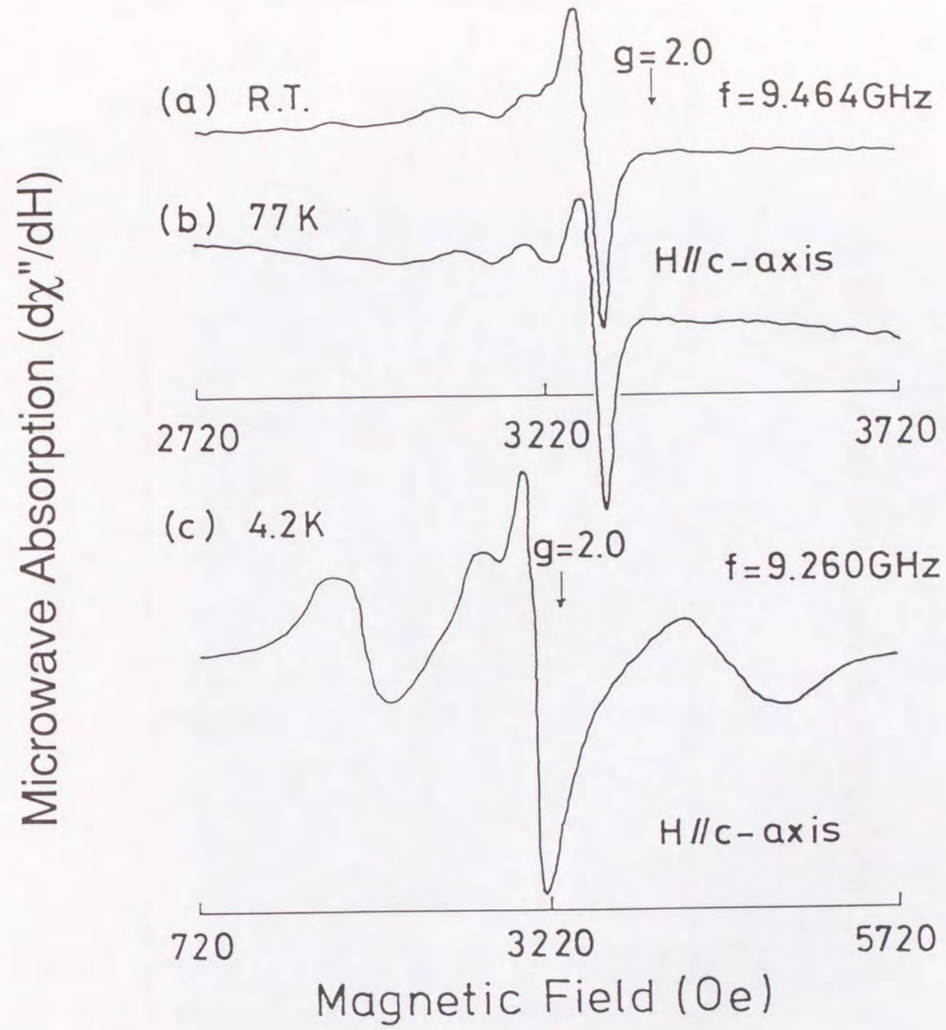


Fig. 4-1-1. ESR signals from a single crystal of Cu^{2+} : NENP obtained at (a) room temperature, (b) 77 K and (c) 4.2 K, when the external magnetic field is applied along the c-axis. Note that the scale of the magnetic field in (c) is expanded compared to (a) and (b).

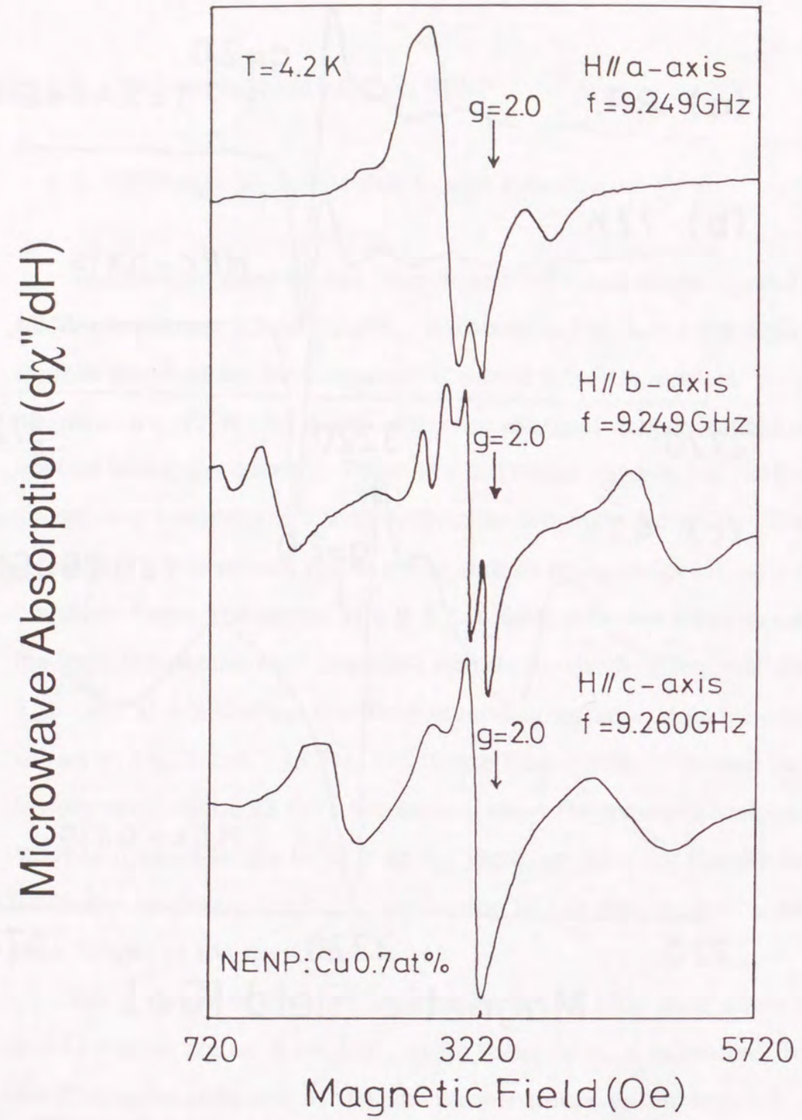


Fig. 4-1-2. ESR signals in 0.7at% Cu : NENP at 4.2 K for the frequency of about 9.25 GHz along the three crystallographic a, b and c axes.

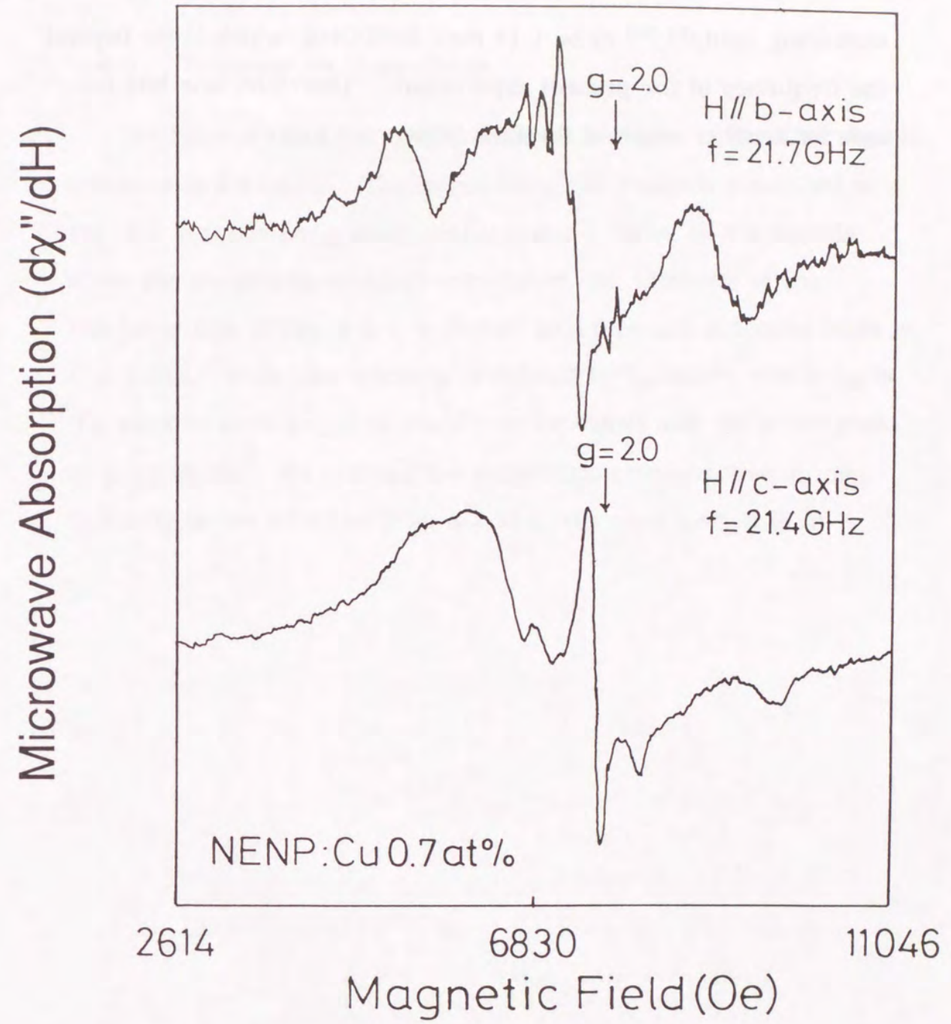


Fig. 4-1-3. ESR signals in 0.7at% Cu : NENP at 4.2 K for the frequency of about 22 GHz, when the external magnetic field is applied to the b- or c-axis.

scattering study[74-76] to be 1.17 meV (283 GHz), which is far beyond the frequency of the present experiment. Therefore, one has to look for another origin of the ESR lines.

4-2. Temperature dependence

We have studied the temperature dependence of the ESR signals obtained at 9.25 GHz. The signal along the c-axis is presented in Fig. 4-2-1 at the designated temperatures. Since all the signals show the same temperature dependence, the intensity of the rightmost line in Fig. 4-2-1 is plotted as a function of temperature in Fig. 4-2-2. Here, the intensity is defined by $I_{pp}(\Delta H)^{2}$, where I_{pp} is the peak-to-peak height of the derivative signal and ΔH is the peak-to-peak width. We discuss the temperature dependence of the intensity of the ESR line (Fig. 4-2-2) in the next section (§ 5).

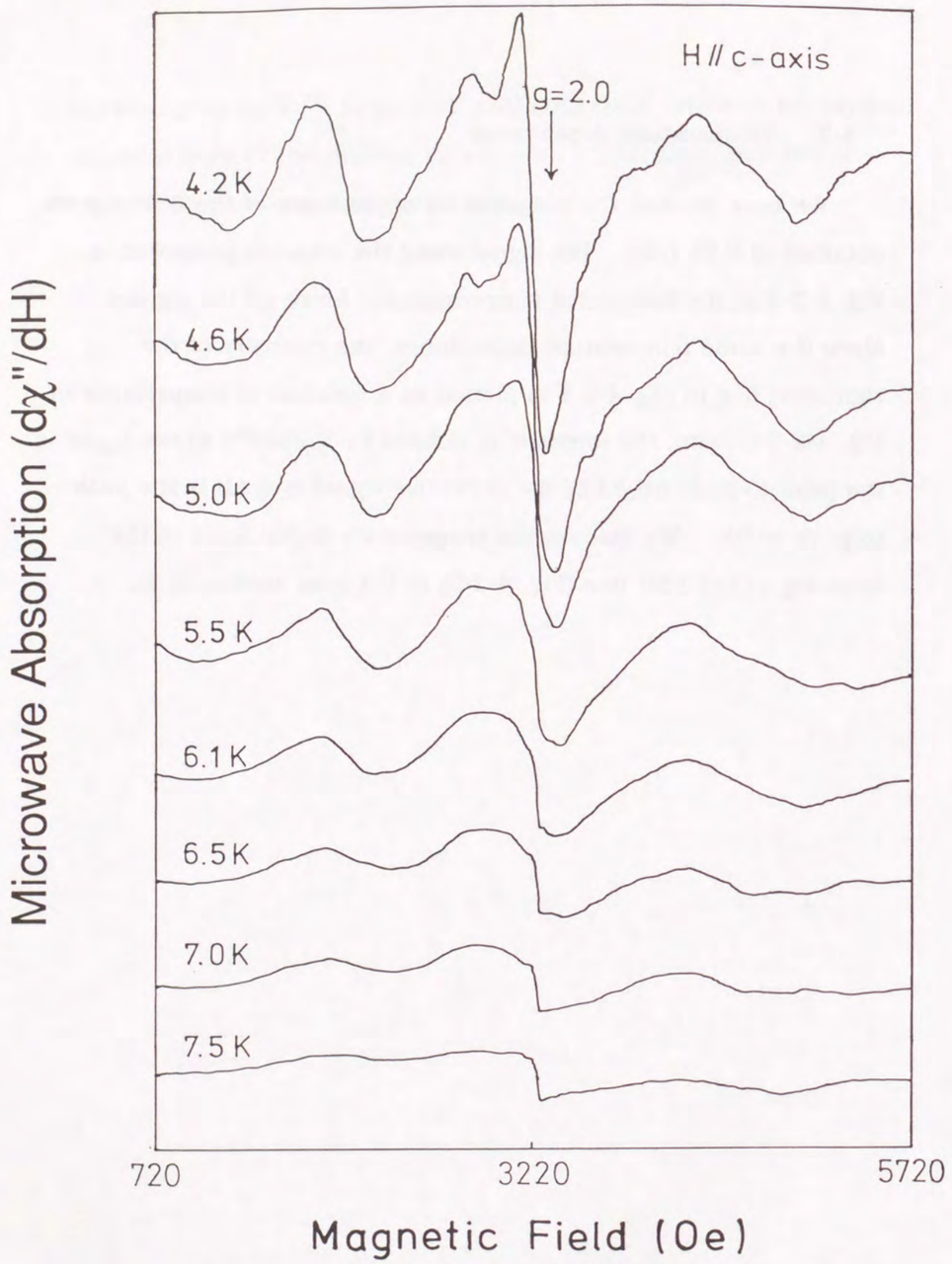


Fig. 4-2-1. Temperature dependence of the ESR signal in Cu^{2+} : NENP, when the external magnetic field is directed to the c-axis. In the a- and b-axes, we obtain the similar temperature dependence of the ESR signal.

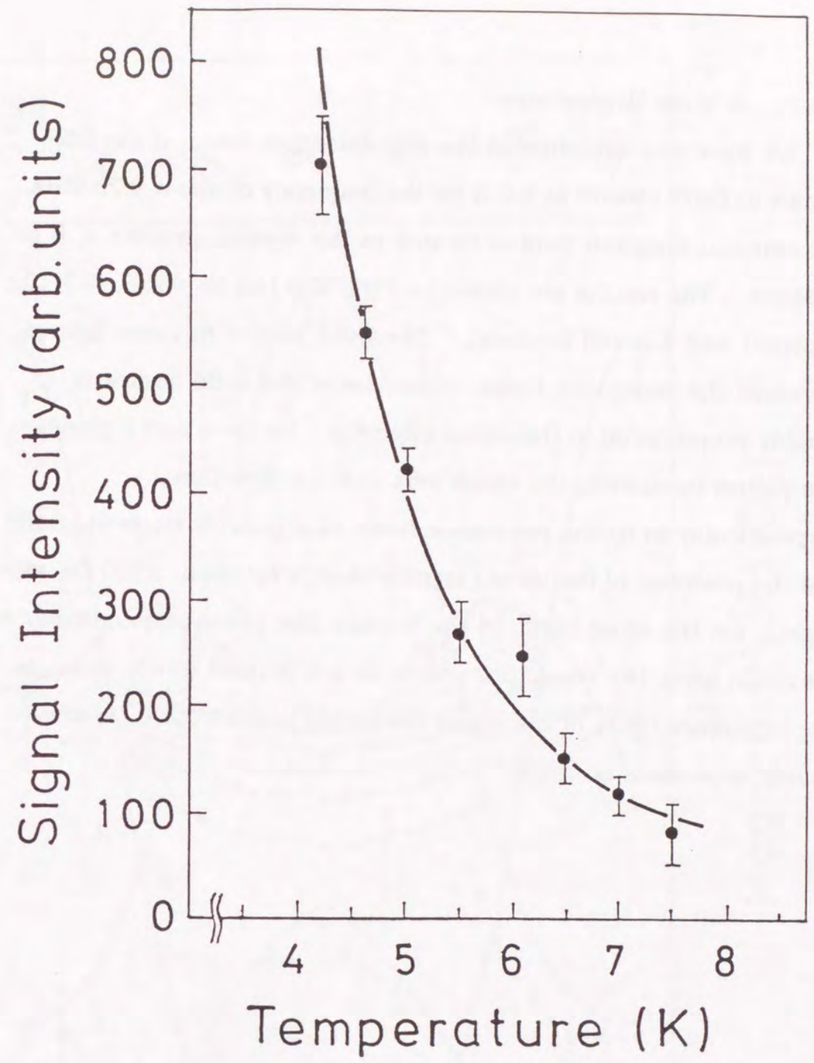


Fig. 4-2-2. Temperature dependence of the intensity of the ESR signal observed at low temperatures in Cu^{2+} : NENP. We show here the intensity of the rightmost signal in Fig. 4-2-1. The solid line is the fit to Eq. (5-2-1) with the Haldane gap energy E_G/k_B=13 K.

4-3. Angular dependence

We have also investigated the angular dependence of the ESR signals in Cu^{2+} : NENP at 4.2 K for the frequency of about 9.25 GHz. The external magnetic field is rotated in the crystallographic a, b or c planes. The results are shown in Figs. 4-3-1(a) (a-plane), 4-3-1(b) (b-plane) and 4-3-1(c) (c-plane). The solid circles in these figures represent the resonance fields. The size of the solid circles is roughly proportional to the signal intensity. In the a and c planes (the planes containing the chain axis and the direction perpendicular to it) the resonance fields change with angle similarly and the positions of the strong signals change by about 2500 Oe with angle. On the other hand, in the b plane (the plane perpendicular to the chain axis), the resonance points do not depend much on angle. The resonance fields of the signal appearing around 3200 Oe are weakly dependent on angle.

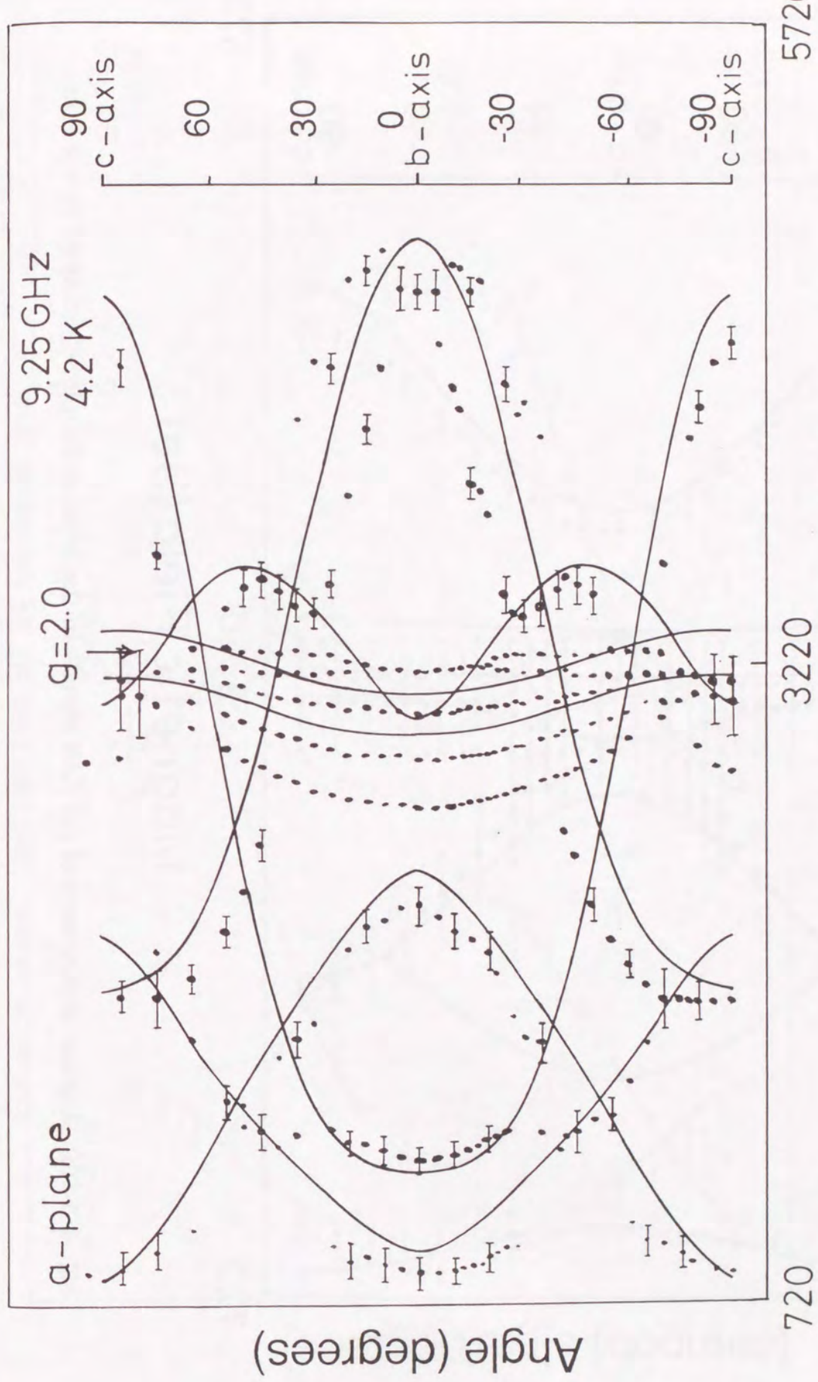


Fig. 4-3-1(a). Angular dependence of the ESR signals in the a-plane (bc-plane) obtained at 4.2 K in 0.7at% Cu : NENP. The solid lines represent the theoretical resonance fields calculated with the Hamiltonian (5-1-1).

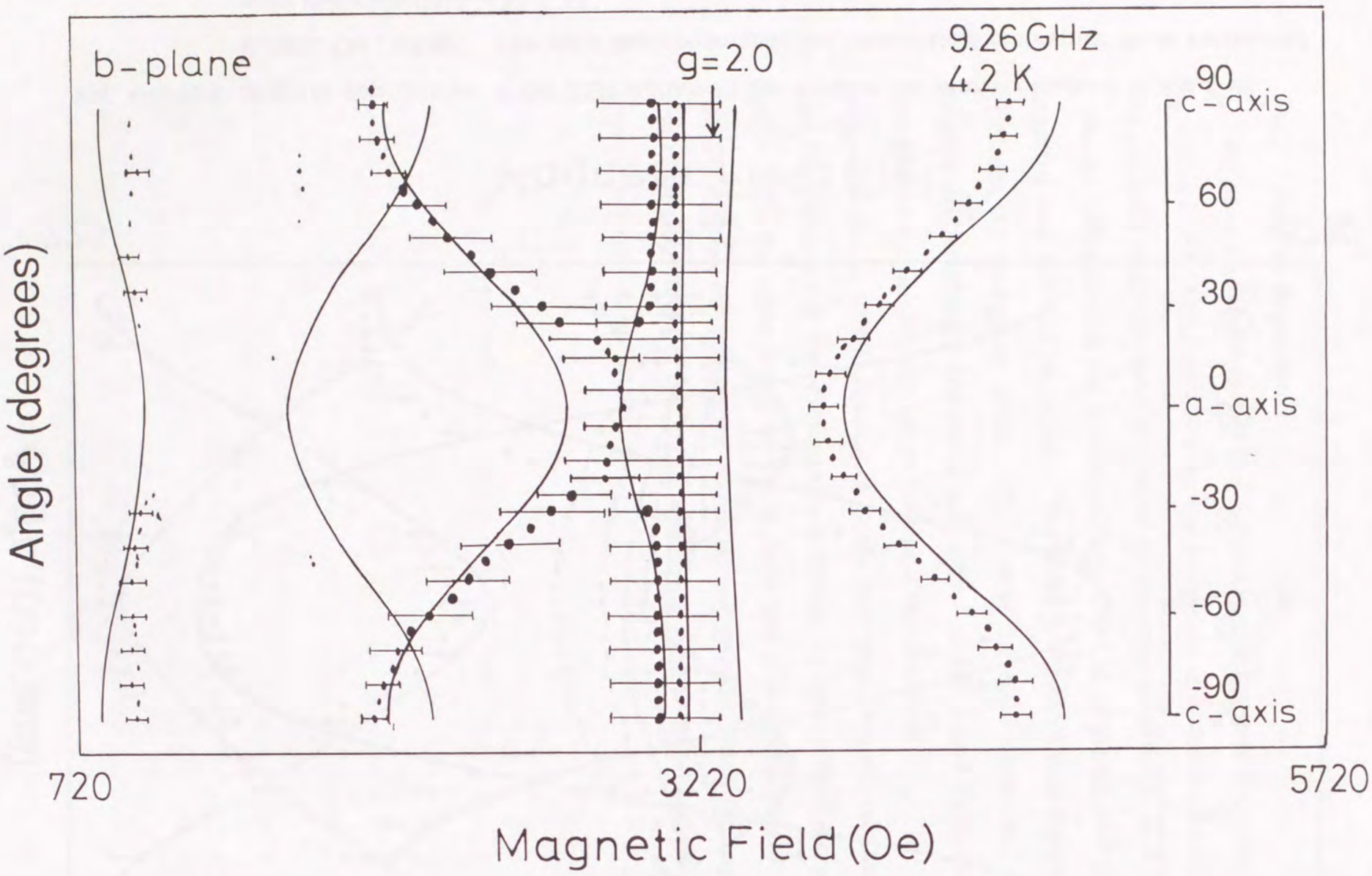


Fig. 4-3-1(b). Angular dependence of the ESR signals in the b-plane (ac-plane) obtained at 4.2 K in 0.7at% Cu : NENP. The solid lines are the theoretical ones.

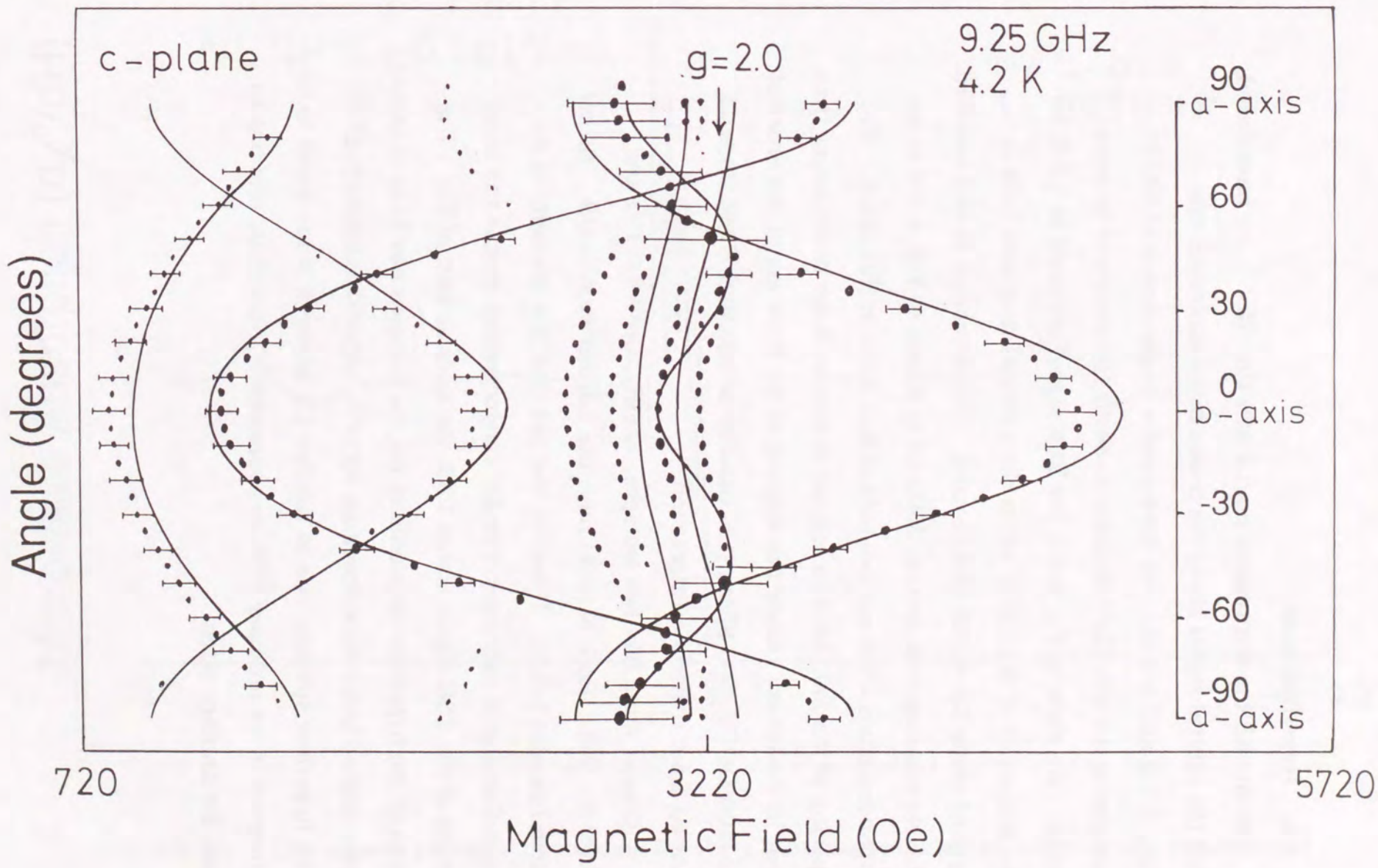


Fig. 4-3-1(c). Angular dependence of the ESR signals in the c-plane (ab-plane) obtained at 4.2 K in 0.7at% Cu : NENP. The solid lines are the theoretical ones.

4-4. Hyperfine lines

In the ESR measurement on 0.7 at% Cu : NENP, we have found that the central signal along the b-axis has a structure (see Figs. 4-1-2 and 4-1-3). We have used a single crystal of NENP containing 0.1 at% Cu^{2+} in order to study the structure in more detail. We show in Fig. 4-4-1 the ESR signal obtained at 1.6 K for the frequency of 9.21 GHz when the external magnetic field is applied along the chain axis (b-axis). The structure is well resolved. The signals observed around 3000 Oe is shown in Fig. 4-4-2 in an expanded scale. We see two sets of four lines in this chart. The spacing of the four lines in one set is almost three times larger than that in the other. Since the spacing of the lines are of the order of 10~100 Oe (30~300 MHz), it is natural to interpret these lines as arising from hyperfine interaction.

Copper atom has two isotopes, namely, Cu^{63} (69.1%) and Cu^{65} (30.9%). Both of them have the nuclear spin I=3/2. Nickel atom has also I=3/2. However, the fact that the intensity of the hyperfine signal increases with Cu concentration means the main origin of the ESR signal comes from the nuclear spin of Cu. The ratio of the hyperfine constants of the Cu isotopes has been obtained from atomic beam experiment as $A(Cu^{63})/A(Cu^{65})=0.933567\pm2$[103]. The hyperfine splitting due to the two Cu isotopes is too small to be observed in an ordinary ESR measurement. Therefore, one has to look for another origin.

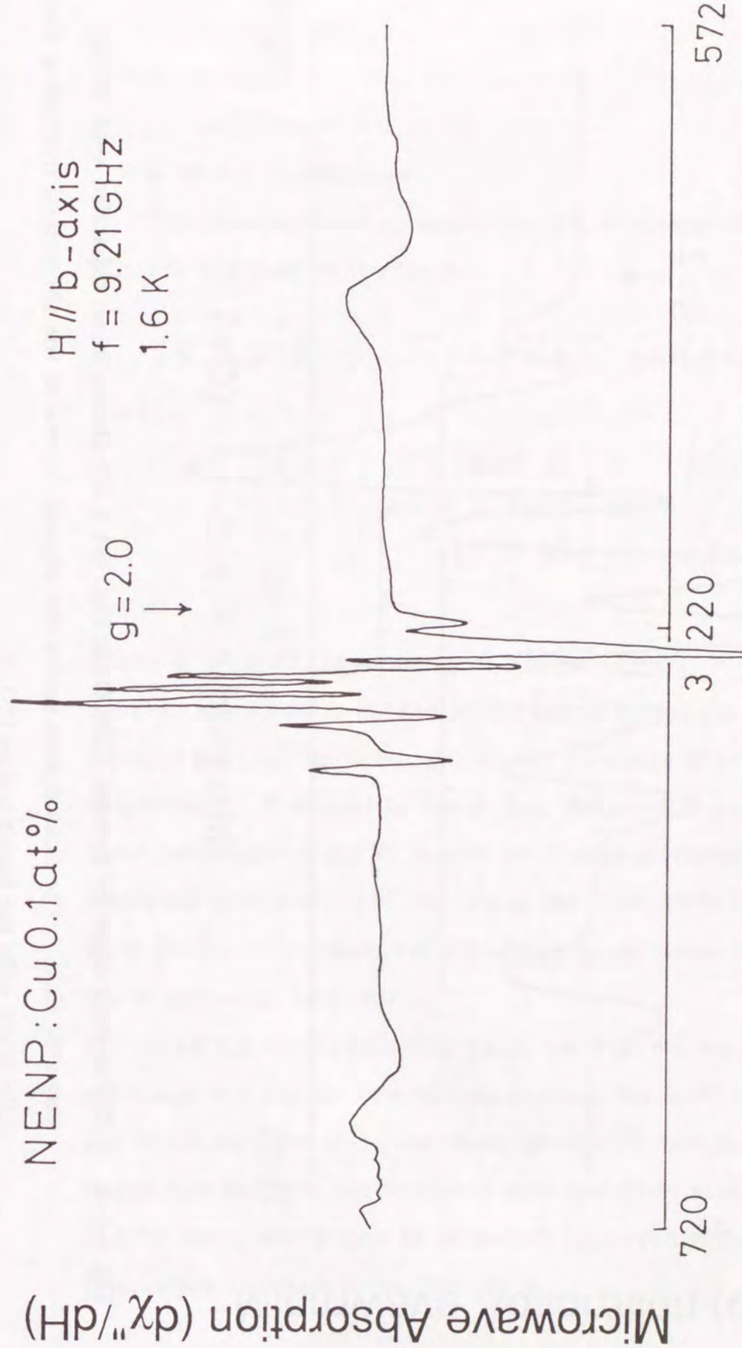


Fig. 4-4-1. ESR signals in NENP containing 0.1at% Cu atoms obtained at 1.6 K for the frequency of 9.21 GHz, when the external magnetic field is applied to the b-axis. We see well resolved signals around 3000 Oe.

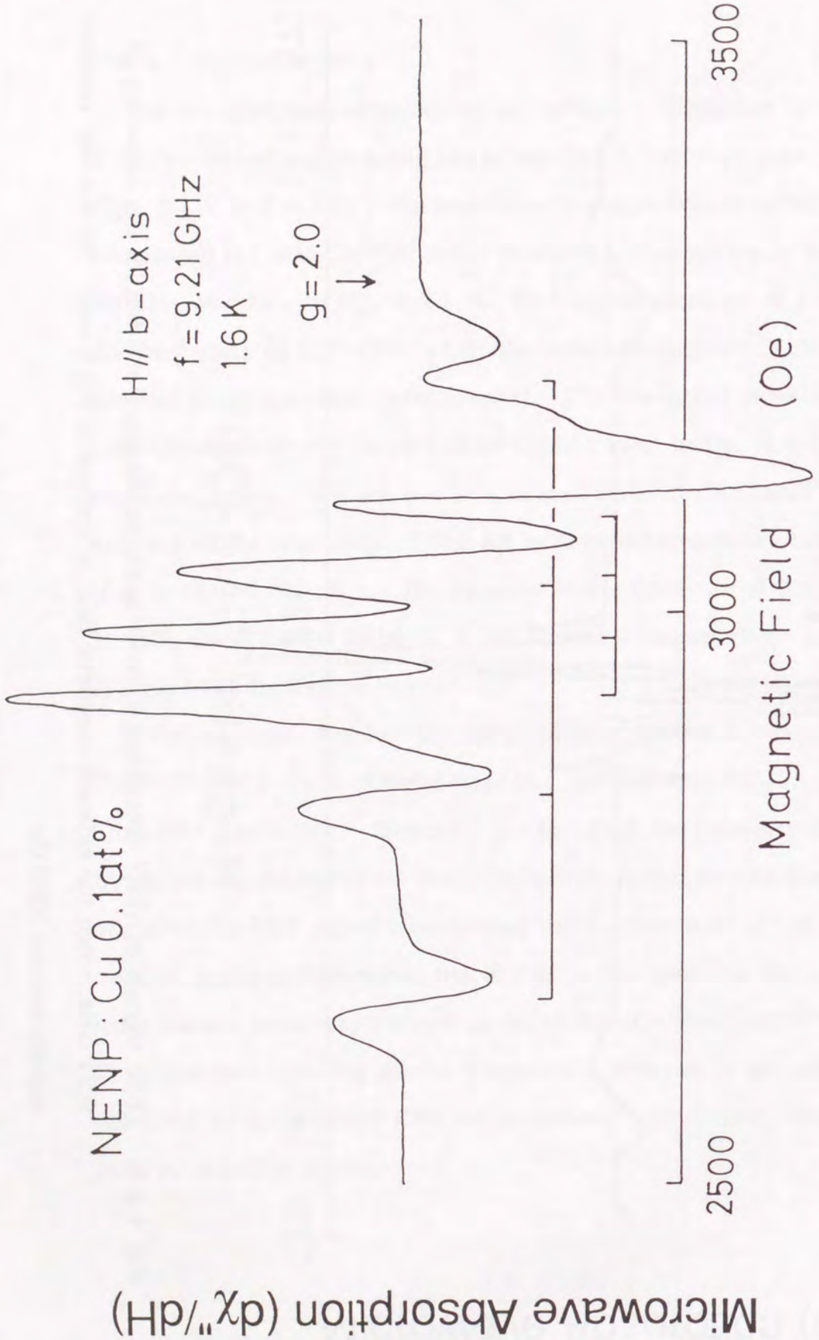


Fig. 4-4-2. ESR signals observed around 3000 Oe in Fig. 4-4-1 are shown in an expanded scale of the magnetic field. The ticks drawn under the signals represent the theoretical resonance fields calculated with the Hamiltonian (5-1-3).

§ 5. Analysis

5-1. Model Hamiltonian

The Hamiltonian expressing the model system illustrated in Fig. 1-2-4(b) may be written as,

$$\mathcal{H} = -2\,(\vec{S_1} + \vec{S_2})\,\tilde{J}\,\vec{s} + \mu_B(\vec{S_1} + \vec{S_2})\,\tilde{g_{Ni}}\,\vec{H} + \mu_B\,\vec{s}\,\tilde{g_{Cu}}\,\vec{H}, \quad (5\text{-}1\text{-}1)$$

with

$$\tilde{J} = \begin{pmatrix} J_x & 0 & 0 \\ 0 & J_y & 0 \\ 0 & 0 & J_z \end{pmatrix}, \quad \tilde{g_{Ni}} = \begin{pmatrix} g_{Ni}^x & 0 & 0 \\ 0 & g_{Ni}^y & 0 \\ 0 & 0 & g_{Ni}^z \end{pmatrix}, \quad \tilde{g_{Cu}} = \begin{pmatrix} g_{Cu}^x & 0 & 0 \\ 0 & g_{Cu}^y & 0 \\ 0 & 0 & g_{Cu}^z \end{pmatrix}, \quad (5\text{-}1\text{-}2)$$

where $\tilde{J}$ is the Ni-Cu exchange interaction tensor, $\vec{S}_1$, $\vec{S}_2$ (=1/2) the spin variables induced at the Ni sites neighboring Cu impurity, $\vec{s}$ (=1/2) the Cu^{2+} spin, $\tilde{g}_{Ni}$ and $\tilde{g}_{Cu}$ the g tensors of Ni and Cu spins, respectively. It should be noted that, despite the much larger D term anisotropy in the Ni chains, no D term is possible for the fractional spin degrees of freedom at the chain ends because they have S=1/2. Therefore, the anisotropy is not larger than that of the Cu-Ni exchange interaction.

Since Cu concentration is small (~0.7 at. %), we can neglect the exchange and dipolar interactions between the Cu^{2+} spins. Taking the Ni-Cu distance along the chain as ~5 Å[96], the dipole-dipole interaction between the fractional spin and Cu^{2+} spin is of the order of 0.01 cm^{-1}, which may be neglected compared with the exchange interaction between them (See §5-3).

In the analysis of the experimental data on NENP containing 0.1 at% Cu impurities[90], we have to consider the hyperfine interaction. In this case, the Hamiltonian may be written as,

$$\mathcal{H} = -2\,(\vec{S_1}+\vec{S_2})\,\tilde{J}\,\vec{s} + \mu_B(\vec{S_1}+\vec{S_2})\,\tilde{g_{Ni}}\,\vec{H} + \mu_B\,\vec{s}\,\tilde{g_{Cu}}\,\vec{H} + \vec{I}\,\tilde{A}\,\vec{s}, \quad (5\text{-}1\text{-}3)$$

with

$$\tilde{A} = \begin{pmatrix} A_\perp & 0 & 0 \\ 0 & A_\perp & 0 \\ 0 & 0 & A_{//} \end{pmatrix}, \quad (5\text{-}1\text{-}4)$$

where $\vec{I}$ is the Cu nuclear spin (I=3/2) and $\tilde{A}$ is the hyperfine constant tensor. Here, we have assumed $A_x=A_y(=A_\perp)$.

5-2. Temperature dependence

We find that the observed intensity (Fig. 4-2-2) can be fitted, for 4.2 K < T < 7.5 K, by the phenomenological formula :

$$I = I_0\{1-\exp(-\sigma/k_BT)\}\{\exp(E_G/k_BT)-1\}, \quad (5\text{-}2\text{-}1)$$

where I_0 is a constant, σ the energy difference between the two levels pertaining to the ESR. The first factor is standard, following from the balance between emission and absorption. The second factor, involving the Haldane gap energy E_G, reflects the growing probability of finding isolated three spin systems as the temperature is reduced below the Haldane gap. At higher temperatures, magnetic excitations will exist in the chains. These excited states will interact with the three spin systems, broadening and weakening the ESR signal. The full curve in Fig. 4-2-2 is drawn using Eq. (5-2-1) with E_G/k_B=13 K. This value of E_G is the same as that obtained from the ESR measurement on NENP[79].

Recently, Mitra et al.[104] have proposed a theory on the temperature dependence of the ESR signals in NENP : Cu. The intensity I(T) is given theoretically by,

$$I(T) = I(0)\,\tanh\left(\frac{\beta h\nu_0}{2}\right)\frac{\exp[-(\pi^{-1/2}L_{min}\,\lambda_T^{-1}-1)\,e^{-\beta E_G}]}{1+\pi^{-1/2}L_0\,\lambda_T^{-1}\,e^{-\beta E_G}}, \quad (5\text{-}2\text{-}2)$$

$$\lambda_T \equiv \frac{hc}{2\pi}\left(\frac{\beta}{2E_G}\right)^{1/2}, \quad (5\text{-}2\text{-}3)$$

where I(0) is the intensity at 0 K, $\beta=1/k_BT$, L_{min} a lower cut off chain length discussed in ref. 104, $2\pi\lambda_T$ the de-Broglie thermal wave length of the boson, L_0 the average length of the chain and c the effective "velocity of light" ($E_G=mc^2$).

A physical explanation of this theory is the following : even if a single excitation is present on the chain, the resonance line is broadened out, because the excitation traverses the entire chain and interacts with the trimer spins. Therefore, the intensity is proportional to the probability of finding a chain with no excitation present. Mitra et al. have compared the theory with the experiment on 0.7 at% Cu : NENP. The result of the comparison is shown in Fig. 5-2-1.

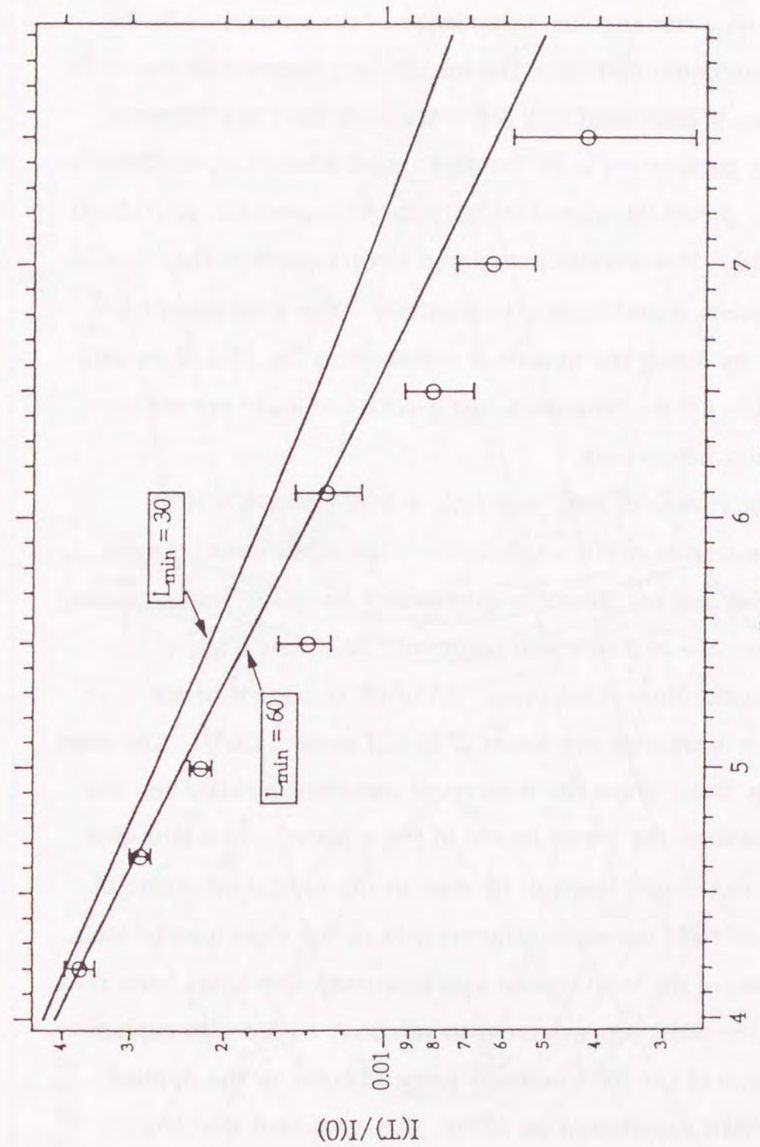


Fig. 5-2-1. Temperature dependence of the ESR intensity is plotted on a semilogarithmic scale. The intensities are normalized to one at T=0. Here, L_0=143 corresponding to the impurity concentration of 0.7% and ω_0=9.25 GHz are used. The curve for L_{min} =60 agrees qualitatively with the experimental data (O). (Quoted from ref. 104)

5-3. Angular dependence

We calculate the angular dependence of the resonance fields with the Hamiltonian (5-1-1). The angular dependence of the hyperfine lines is discussed in § 5-5. We have used the following values for the parameters to fit the data : J_x=0.83cm^{-1}, J_y=0.79cm^{-1}, J_z=0.67cm^{-1}, g_{Ni}^x=2.00, g_{Ni}^y=2.02, g_{Ni}^z=2.15, g_{Cu}^x=2.08. g_{Cu}^y=2.10 and g_{Cu}^z=2.24. The directions x, y and z correspond to the crystallographic c, a and b axes, respectively. The g-values of Cu^{2+} are obtained by fitting the hyperfine signals with Eq. (5-1-3) as will be discussed in § 5-5. Therefore, the g-values of Cu^{2+} are not adjustable parameters here.

The solid curves in Figs. 4-3-1(a), 4-3-1(b) and 4-3-1(c) represent the results of the calculation. The agreement between the experiment and the theory is satisfactory for the b- and c-planes. In the a-plane, the experimental resonance fields are slightly different from the theoretical ones. In order to have a better agreement, we introduce two kinds of ligand around Cu^{2+}. The solid curves in Fig. 5-3-1 show the theoretical transition fields when the z-axis is tilted from the b-axis by ±8° in the a-plane. This situation corresponds to the two kinds of Ni sites in the crystal structure of NENP. These solid curves satisfactorily fit to the experimental data.

The tilting of the local crystal axis discussed above has been also observed in the NMR measurement in ref. 85. In order to explain the observation of the Ni^{2+} moment perpendicular to the applied field in the NMR experiment on NENP, they assumed that the principal axis of g tensor is tilted from the b-axis, reflecting the local crystal symmetry. They used the tilting angle of ±10° for the fit of

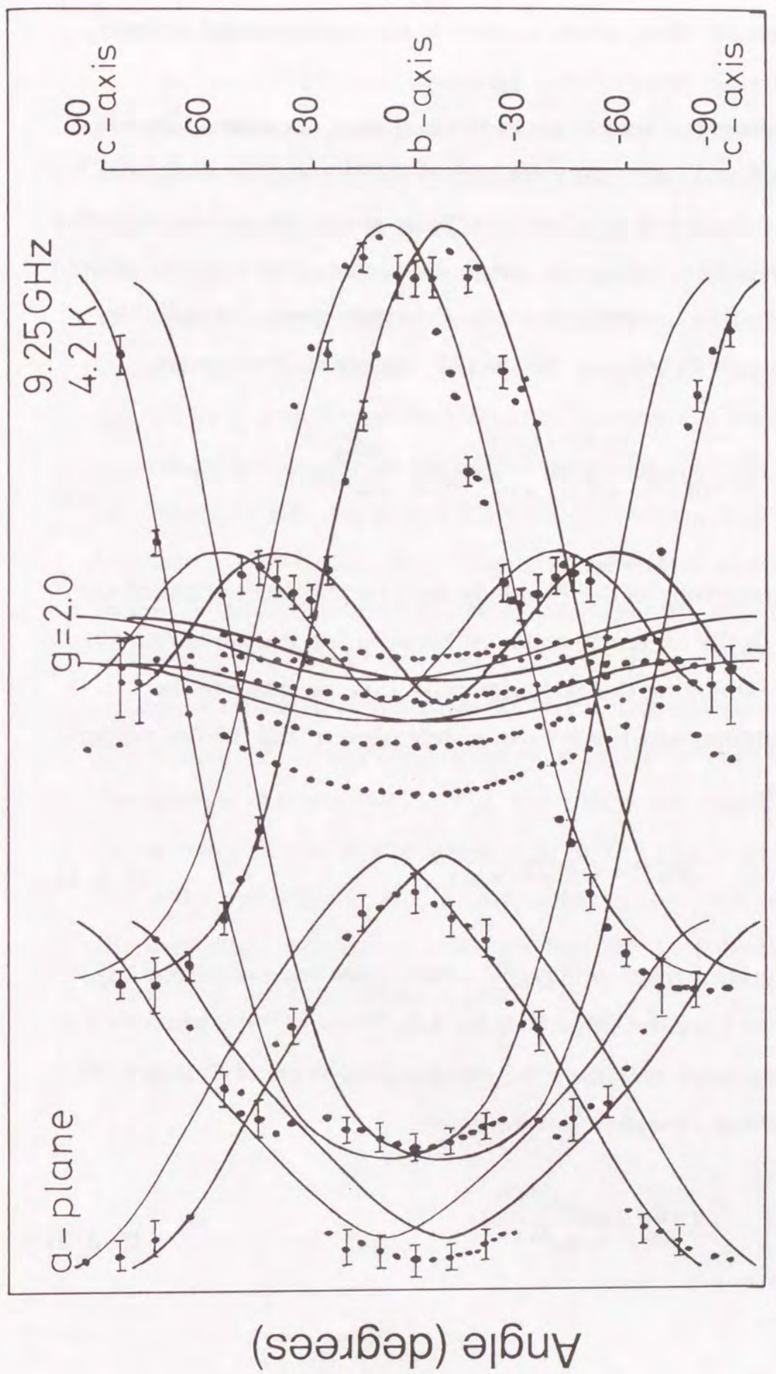


Fig. 5-3-1. The solid lines represent the theoretical resonance fields when the principal z-axis tilts from the b-axis by ± 8° in the a-plane. The experimental data are the same as in Fig. 4-3-1(a).

the experimental data, which is close to the one obtained in this study (±8°).

We discuss the anisotropy in the exchange constants between the fractional and Cu^{2+} spins denoted by $J_x^{Ni\text{-}Cu}$, $J_y^{Ni\text{-}Cu}$ and $J_z^{Ni\text{-}Cu}$. Because the fractional spin has S=1/2, no single ion anisotropy terms (D, E) are possible. Thus the single ion anisotropies in NENP should be reflected in the anisotropy of the exchange constants $J_x^{Ni\text{–}Ni}$, $J_y^{Ni\text{-}Ni}$ and $J_z^{Ni\text{–}Ni}$ between the S=1/2 degrees of freedom as,

$$\frac{E}{D} \approx \frac{J_x^{Ni\text{-}Ni} - J_y^{Ni\text{-}Ni}}{J_z^{Ni\text{-}Ni} - (J_x^{Ni\text{-}Ni} + J_y^{Ni\text{-}Ni})/2} \equiv \frac{\Delta J_{xy}^{Ni\text{-}Ni}}{\Delta J^{Ni\text{-}Ni}} . \qquad (5\text{-}3\text{-}1)$$

This anisotropy in $J^{Ni\text{-}Ni}$ should then be the main origin of the anisotropy in the exchange constant between the fractional and Cu spins. In estimating the exchange constants, we assume the following relation which has been widely used in the field of random magnetism,

$$J_{x,y,z}^{Ni\text{-}Cu} = \sqrt{J_{x,y,z}^{Ni\text{-}Ni} \cdot J_{x,y,z}^{Cu\text{-}Cu}} . \qquad (5\text{-}3\text{-}2)$$

Using the known relation $(\Delta g/g)^2 J$ which gives the anisotropy in exchange, we have the value 0.06 for $\Delta J_{xy}^{Ni\text{-}Cu}/\Delta J^{Ni\text{-}Cu}$, whereas the experimental value is 0.28. The experimental value of E/D is 0.08. From the above consideration, we have

$$O(\frac{E}{D}) = O(\frac{\Delta J_{xy}^{Ni\text{-}Cu}}{\Delta J^{Ni\text{-}Cu}}) . \qquad (5\text{-}3\text{-}3)$$

5-4. Energy diagram

We calculate the energy levels of this model system in order to compare the experimental data observed at X- and K-bands with the theory. In Fig. 5-4-1 are shown the energy values calculated with the Hamiltonian (Eq. (5-1-1)) as a function of external magnetic field, when H is applied to the b- or the c- axis. Here, we have used the same values for the parameters as in § 5-3 : J_x=0.83cm^{-1}, J_y=0.79cm^{-1}, J_z=0.67cm^{-1}, g_{Ni}^x=2.00, g_{Cu}^x=2.08, g_{Ni}^z=2.15 and g_{Cu}^z=2.24. The sign of the exchange constants is determined from the temperature dependence of the rightmost signals in Fig. 5-4-2 observed at 1.5 K, 1.8 K and 4.2 K for the frequency of ~22 GHz. In the case of H// b-axis, the intensity of the rightmost signal becomes larger as the temperature is decreased, while the situation is reversed in the case of H// c-axis. The g^z-value of Ni^{2+} is the same as that obtained from the susceptibility measurement and the g^x-value of Ni^{2+} is slightly smaller than that (see Table 2-1-1)[96]. The arrows at the bottom in Fig. 5-4-1 show the experimental resonance fields with stronger intensity (the bigger circles in Fig. 4-3-1), and the broken arrows between the sublevels represent the theoretical transitions. We see that the agreement between the theory and the experiment is good.

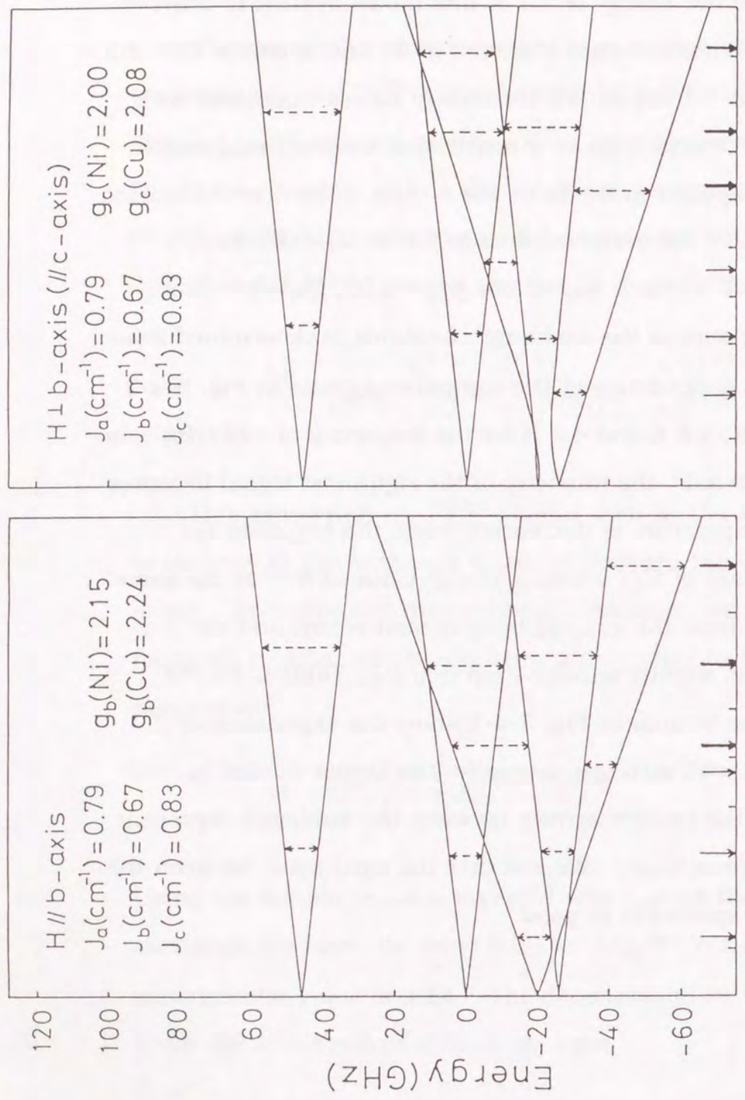


Fig. 5-4-1. Energy levels calculated with the Hamiltonian (Eq. (5-1-1)) as a function of external magnetic field parallel (left panel) and perpendicular (right panel) to the b-axis. The arrows show the experimental resonance fields corresponding to strong signals for the frequency of 9.249 GHz (H//b) and 9.260 GHz (H//c), and the thick arrows those for the frequency of 21.7 GHz (H//b) and 21.4 GHz (H//c), respectively. The broken arrows drawn between the energy levels represent the theoretical transitions.

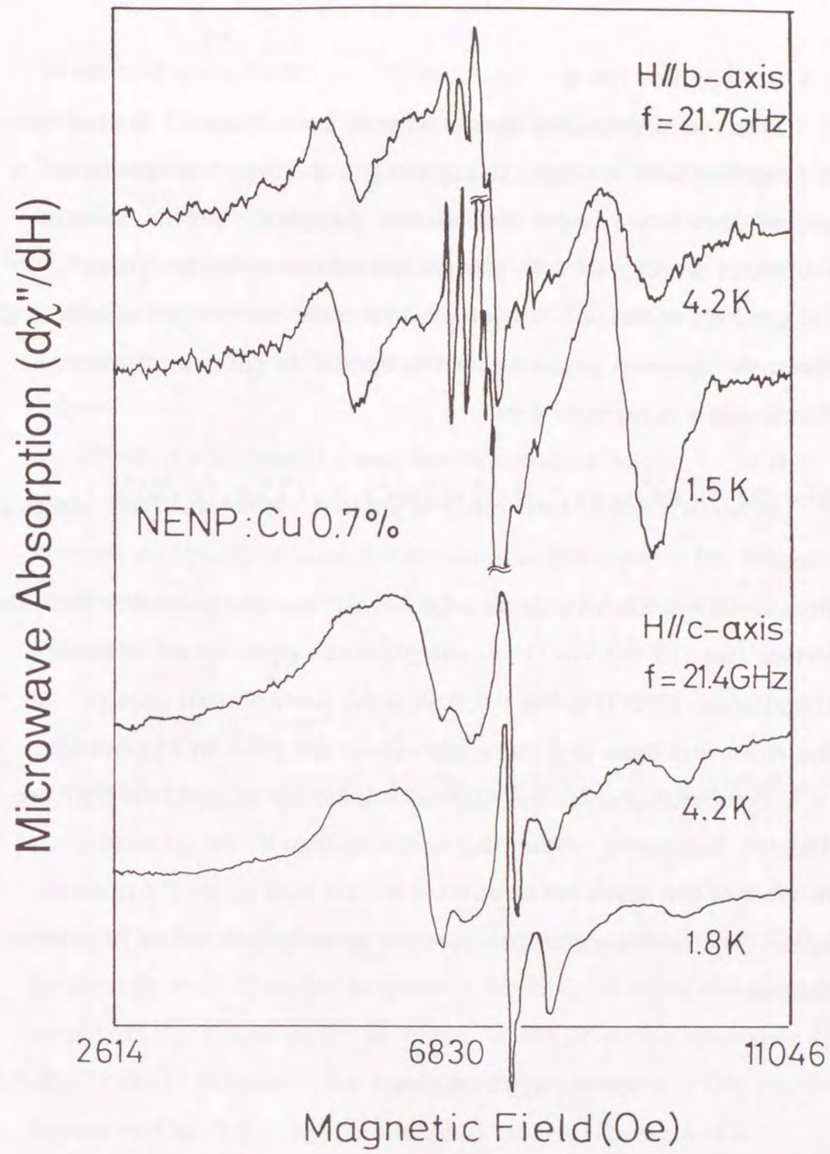


Fig. 5-4-2. ESR signals observed at 1.5 K, 1.8 K and 4.2 K for the frequency of ~22 GHz. For H// b, the intensity of the rightmost signal becomes larger as temperature is decreased, while the intensity becomes smaller for H// c.

5-5. Hyperfine lines

First, we discuss the reason why we have observed the two sets of hyperfine lines and why the spacing of the four lines in one set is almost three times larger than that in the other. For the sake of simplicity, we use the isotropic Hamiltonian where $J_x=J_y=J_z=J$, and the g-values of Ni (g_{Ni}) and Cu (g_{Cu}) have the same value ($g_{Ni}=g_{Cu}=g$). When the external magnetic field is applied to the z-axis, the Hamiltonian is expressed as,

$$\mathcal{H} = -2J\,(\vec{S_1}+\vec{S_2})\vec{s} + g\mu_B H\,(S_1^z+S_2^z+s^z) + A_{//}\,I^z s^z + A_\perp\,(I^x s^x + I^y s^y) \quad (5\text{-}5\text{-}1)$$

Because the latter two terms (~10^{-2} cm^{-1}) are much smaller than the former two (10^{-1}~1 cm^{-1}), we calculate the eigen states of the Hamiltonian (5-5-1) using the first order perturbation theory. All the eigen functions and the eigen values are given in Appendix I.

The conditions for the allowed transitions to occur in ESR are $\Delta S_m=\pm 1$ and $\Delta m=0$, where ΔS_m is the change in the quantum number of the resultant electron spin, Δm that of the Cu nuclear spin. The resonance frequencies are given as a function of external field as,

$$h\nu_0 = g\,\mu_B H + A_{//}\,m, \quad (5\text{-}5\text{-}2)$$

$$h\nu_0 = g\,\mu_B H + A_{//}\,m/3, \quad (5\text{-}5\text{-}3)$$

where m (m=3/2, 1/2, -1/2 and -3/2) is the quantum number of the Cu nuclear spin. The resultant spin $\vec{S}'$ ($=\vec{S}_1+\vec{S}_2$) consists of a singlet

(S'=0) and a triplet (S'=1). This singlet and the Cu spin (s=1/2) couple to form a doublet (denoted by a). On the other hand, the triplet and the Cu spin couple to form a doublet (denoted by b) and a quartet. Equation (5-5-2) corresponds to the transitions between the sublevels in the doublet a, and Eq. (5-5-3) to those in the doublet b and the quartet. Therefore, we have two kinds of hyperfine structure, one of which has three times larger spacing than the other.

Next, we analyze the angular dependence of one set of the hyperfine lines whose spacing is wider than that of the other. Since this set of hyperfine lines corresponds to the case of the singlet (S'=0) state of the resultant spin $\vec{S}'$, we use the following Hamiltonian,

$$\begin{aligned}\mathcal{H} &= \mu_B \vec{s}\,\tilde{g_{Cu}}\,\vec{H} + \vec{I}\,\tilde{A}\,\vec{s} \\ &= g^z_{Cu}\mu_B s^z H\cos\theta + g^x_{Cu}\mu_B s^x H\sin\theta + A_{//} I^z s^z + A_\perp (I^x s^x + I^y s^y)\end{aligned} \quad (5\text{-}5\text{-}4)$$

where θ is the angle between the external magnetic field and the chain axis (z // b) in the bc-plane. In §5-3, we tilted the principal axis from the b-axis in the bc-plane for the fit of the resonance fields. We, however, take here the b-axis as a principal one. The result is shown in Fig. 5-5-1, where the open circles represent the experimental data and the solid lines the transition fields calculated with the Hamiltonian (Eq. (5-5-4)). The resonance fields are calculated in Appendix II using the second order perturbation theory, the latter two terms in Eq. (5-5-4) being a perturbation.

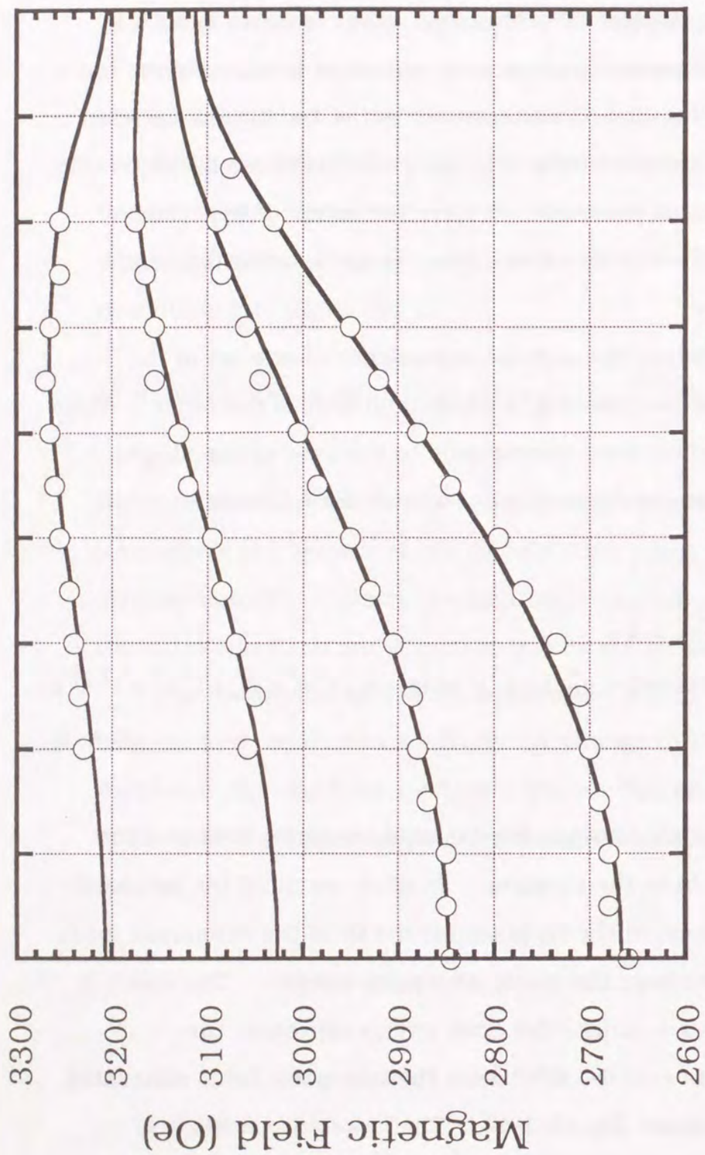


Fig. 5-5-1. Angular dependence of the hyperfine lines which have wider splitting than the other, when the external magnetic field is rotated in the a-plane (bc-plane). The solid lines are the theoretical resonance fields calculated with the Hamiltonian (5-5-4) (See appendix II). The circles show the experimental resonance fields.

The parameters are obtained from the fit of the experiment as follows: $g_z^{Cu}=2.24$, $g_x^{Cu}=2.08$, $|A_{//}|=188\times10^{-4}cm^{-1}$ (0.565 GHz) and $|A_{\perp}|=30.0\times10^{-4}cm^{-1}$ (0.090GHz). The values of the hyperfine constant are those generally accepted for the hyperfine constant of Cu. This is discussed in the latter part of this subsection. The g-value along the y-axis is also obtained to be $g_y^{Cu}=2.10$ from the analysis of the data (H//a).

The energy levels calculated with the Hamiltonian (Eq. (5-1-3)) are shown in Fig. 5-5-2 as a function of magnetic field. Here we use the same values of the parameters (Jx, Jy, Jz etc.) obtained in the previous subsection, and the g-values of Cu and the hyperfine constants obtained above. The lines drawn between the calculated levels in Fig. 5-5-2 represent the allowed transitions. We see three sets of four lines around 3000 Oe for the frequency of 9.210 GHz. Since the highest levels are located at about 50 GHz (2.4 K) above the others, we can not observe the signals from them at the low temperature (1.6 K). Therefore, we see two sets of hyperfine lines in the experiment. The ticks in Fig. 4-4-2 show the resonance fields calculated with the Hamiltonian (Eq. (5-1-3)). When the magnetic field is applied to the c- or a- axes, the hyperfine constant ($A_{\perp}$) is so small that we can not see the hyperfine structure.

Next, we discuss the large anisotropy in the hyperfine constant based on a ligand field theory. The study of hyperfine signals from Cu^{2+} in some single crystals and Cu complexes in solution or the vitreous state was carried out by Maki and McGarvey[105], Kivelson and Neiman[106] and Gersmann and Swalen[107]. Taking into account the covalent character of the bonding with the ligands, they

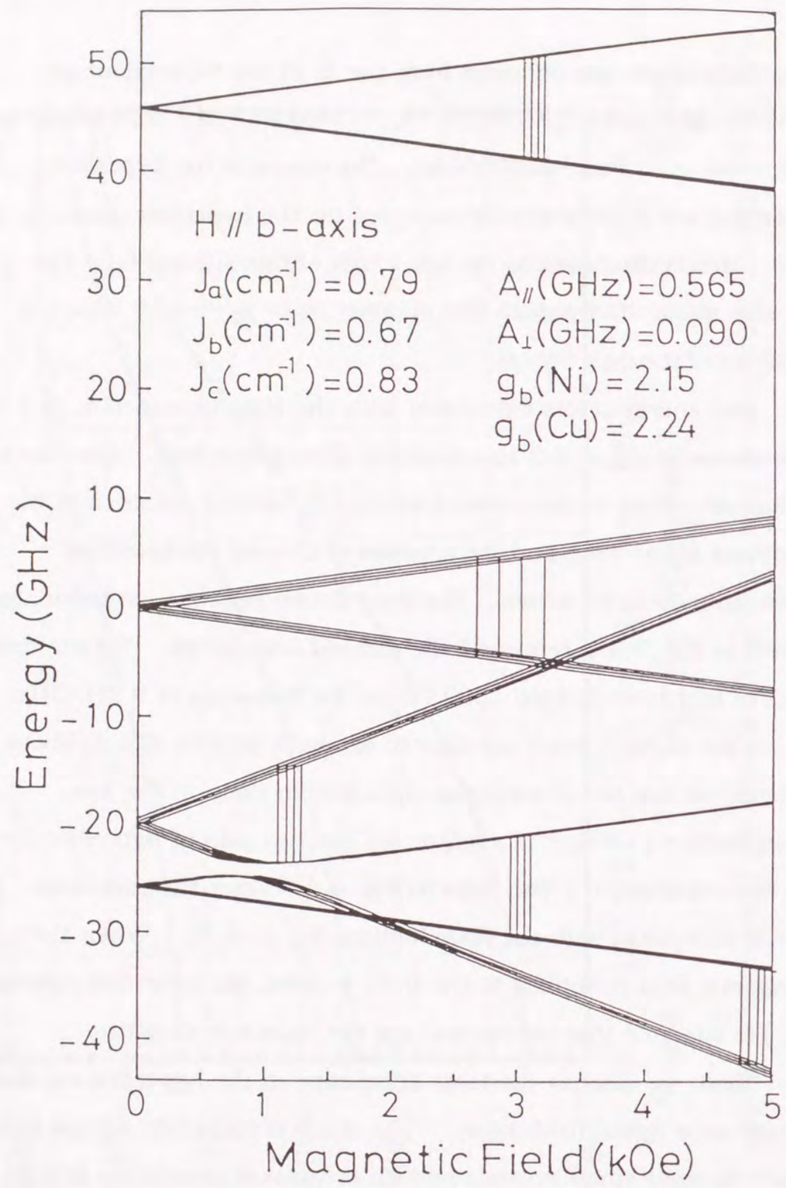


Fig. 5-5-2. Energy levels calculated with the Hamiltonian (Eq. (5-1-3)) as a function of external magnetic field. The solid lines drawn between the energy levels represent the theoretical transitions. We see three sets of four lines around 3000 Oe.

calculated the parameters of the spin Hamiltonian by applying second order perturbation theory.

When a Ni atom in NENP is substituted by a Cu atom, the Cu atom is placed under a distorted orthorhombic ligand field. We, hereafter, approximate this ligand field by a tetragonal one, because g_x-g_y is very small (0.02). Since the distance between ligands and the copper atom along the chain axis is longer than that in the plane perpendicular to the chain axis, the ground state is in $d_{x^2-y^2}$ orbital state. In this case, the parameters are written as follows :

$$g_{//} = 2.0023 - (8\lambda/\Delta E_{xy})[\alpha^2\beta^2 - f(\beta)] , \qquad (5\text{-}5\text{-}5)$$

$$g_{\perp} = 2.0023 - (2\lambda/\Delta E_{xz})[\alpha^2\delta^2 - g(\delta)] , \qquad (5\text{-}5\text{-}6)$$

$$A_{//} = P\,[-\alpha^2(\frac{4}{7}+\kappa) - 2\lambda\alpha^2(\frac{4\beta^2}{\Delta E_{xy}}+\frac{3}{7}\frac{\delta^2}{\Delta E_{xz}})] , \qquad (5\text{-}5\text{-}7)$$

$$A_{\perp} = P\,[\alpha^2(\frac{2}{7}-\kappa) - \frac{22}{14}\frac{\lambda\alpha^2\delta^2}{\Delta E_{xz}}] , \qquad (5\text{-}5\text{-}8)$$

where λ represents the spin-orbit coupling constant, ΔE_{xy} and ΔE_{xz} the energy difference between the ground state ($d_{x^2-y^2}$) and d_{xy} state, and that between $d_{x^2-y^2}$ and d_{xz} states, respectively, α, β and δ overlap parameters between 3d orbital and 2p ligand orbitals, $f(\beta)$ and $g(\delta)$ are small parameters of about 0.1 defined in ref. 107, κ a parameter representing the isotropic Fermi contact interaction. In the latter two expressions, P is given by,

$$P=2\gamma_{Cu}\mu_B\mu_N\langle d_{x^2-y^2}|1/r^3|d_{x^2-y^2}\rangle, \qquad (5\text{-}5\text{-}9)$$

where γ_{Cu} is the gyromagnetic ratio of the copper nucleus and $\langle d_{x^2-y^2}|1/r^3|d_{x^2-y^2}\rangle$ the average value of $1/r^3$ for a free Cu ion.

The parameters α, β and δ represent the effects of covalency. For instance, if $\alpha^2=1$, the bond would be completely ionic. On the other hand, if $\alpha^2=0.5$, the bond would be completely covalent. We use the value - 828cm^{-1} for λ determined spectroscopically. The parameter P has been calculated to be 0.036cm^{-1} by Abragam and Pryce[108]. The estimated error in these quantities is about 3%. The value of κ is assumed to be about 0.43 with an estimated uncertainty of about 5% as Kivelson and Neiman[106] did. Usually, ΔE_{xy} is about 15000 cm^{-1} while ΔE_{xz} is about 25000 cm^{-1}.

Kivelson and Neiman have given an approximate formula for α as,

$$\alpha^2= - (A_{//}/P) + (g_{//}-2.0023) + 3(g_{\perp}-2.0023)/7 + 0.04. \qquad (5\text{-}5\text{-}10)$$

Using the experimental values for $A_{//}$, $g_{//}$ and $g_{\perp}$ we have $\alpha^2=0.84$ from Eq. (5-5-10). Then, we use the values of $\beta^2=0.8$, $\delta^2=1$ and ΔE_{xy}=15000 cm^{-1} as discussed in ref. 107. The energy difference ΔE_{xz} is calculated to be about 28300 cm^{-1} from Eq. (5-5-7). Finally, by using these values, we obtain $A_{\perp}=-30\times10^{-4}$ cm^{-1}. This calculated value is in good agreement with the experimental value ($|A_{\perp}|=30.0\times10^{-4}$ cm^{-1}). We also calculate $g_{//}$ and $g_{\perp}$ with Eqs. (5-5-5) and (5-5-6), and obtain $g_{//}$=2.27 with $f(\beta)$=0.063 and $g_{\perp}$=2.05 with $g(\delta)$=0.042 (ref.107). The calculated g values are

slightly different from the experimental ones ($g_{//}$=2.24, $g_{\perp}$=2.09, $g_{\perp}\equiv(gx+gy)/2$).

5-6. Magnetization in Cu : NENP

In this subsection, we compare the magnetization data obtained from the static magnetization measurement by Renard et al.[82] with our calculation in order to test further the validity of our model. The eigen states for the Hamiltonian (Eq. (5-1-1)) along the b-axis are obtained exactly and the magnetization is calculated analytically. (See Appendix III) We have assumed that the three spin systems do not interact with each other because of the small concentration of Cu impurity. We compare in Fig. 5-6-1 the magnetization data obtained at 2 K in NENP : 6 at% Cu with the theory. In this comparison, we have used the same values of the parameters as those obtained in the ESR study. It should be stressed, therefore, that these are no adjustable parameters. We see that the agreement between the theory and the experiment is excellent.

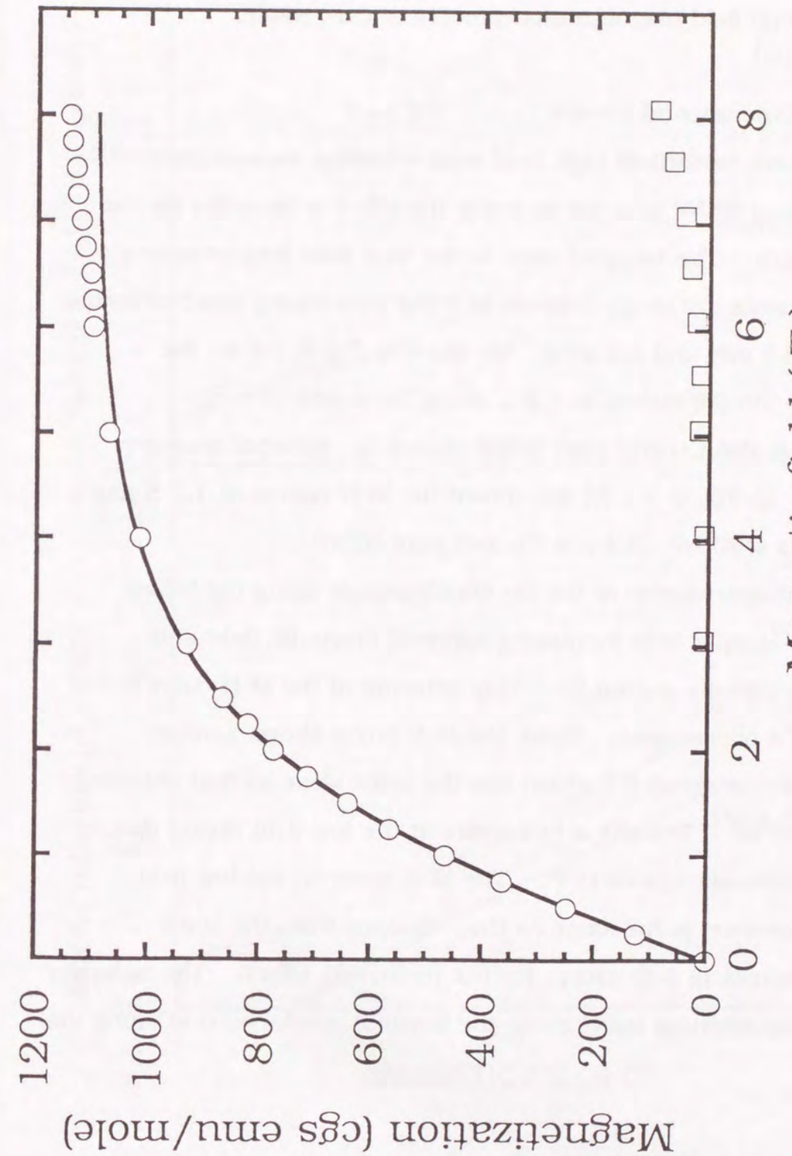


Fig. 5-6-1. The result of the calculation with the Hamiltonian (Eq. (5-1-1)) along the b-axis (see appendix III) is compared with the magnetization data obtained at 2 K from the static measurement by Renard et al. (Ref. 82). (○; NENP : 6at% Cu, □; pure NENP)

§ 6. High field magnetization process of Cu : NENP

6-1. Experimental results

We have performed high field magnetization measurements[91] on Cu doped NENP in order to study the effect of impurity on the Haldane gap. The samples used in the high field magnetization measurements are single crystals of NENP containing small amounts of Cu^{2+} (3.3 at% and 3.8 at%). We show in Fig. 6-1-1 (a) the magnetization (M) curves at 1.3 K along the a-axis of NENP : 3.8 at% Cu and pure NENP versus the external magnetic field (H). In Fig. 6-1-1 (b) are shown the M-H curves at 1.3 K along the b-axis of NENP : 3.3 at% Cu and pure NENP.

The magnetization of the Cu doped sample along the b-axis increases steeply with increasing external magnetic field and reaches a plateau around 2T. This behavior of the M-H curve is typical of a paramagnet. Then, the M-H curve shows another increase above about 8 T which has the same slope as that obtained in pure NENP. There is a hysteresis in the low field region due to the magnetocaloric effect[109]. The M-H curve in the low field region, however, is the same as that obtained from the static measurements (§ 5-6) except for the hysteresis effect. The behavior of the magnetization curve along the a-axis is similar to that along the b-axis.

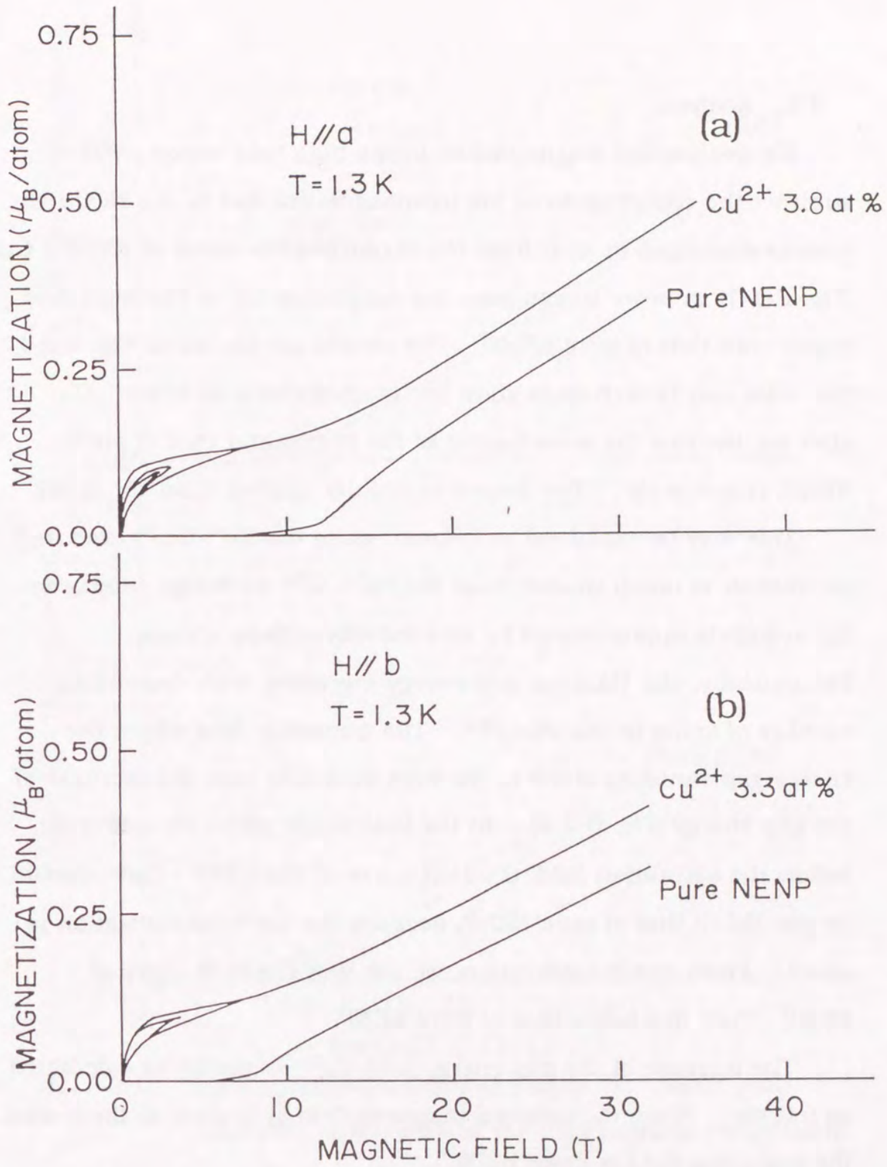


Fig. 6-1-1. (a) Magnetization curve at 1.3 K along the a-axis of 3.8at% Cu : NENP and of pure NENP versus the external magnetic field.
(b) M-H curve at 1.3 K along the b-axis of 3.3at% Cu : NENP and of pure NENP.

6-2. Analysis

We analyze the magnetization in the high field region. We subtract the contribution of the paramagnetism due to the Ni-Cu-Ni trimers discussed in §5-6 from the magnetization curve of NENP : Cu (Fig. 6-1-1) in order to compare the magnetization in the high field region with that of pure NENP. The results are shown in Fig. 6-2-1. The solid and broken lines show the magnetization of NENP : Cu after subtracting the contribution of the trimer and that of pure NENP, respectively. The former is slightly smaller than the latter.

This may be explained as follows : since the Ni^{2+}-Cu^{2+} exchange interaction is much weaker than the Ni^{2+}-Ni^{2+} exchange interaction, the system is approximated by an assembly of finite chains. Theoretically, the Haldane gap energy increases with decreasing number of spins in the chain[54]. The transition field where the energy gap vanishes shifts to the high field side with the increase of the gap energy (Fig. 6-2-2). In the field range above H_T and well bellow the saturation field, the M-H curve of the NENP : Cu^{2+} should be parallel to that of pure NENP, because the Cu^{2+} concentration is small. From this consideration, we see that the M-H curve of NENP : Cu^{2+} lies below that of pure NENP.

The increase of the gap energy with Cu^{2+} impurity is calculated as follows. When the external magnetic field is applied to the b-axis, the transition field is given by[78],

$$H_T = (E_G - |D|/3)/g_b \mu_B , \qquad (6\text{-}2\text{-}1)$$

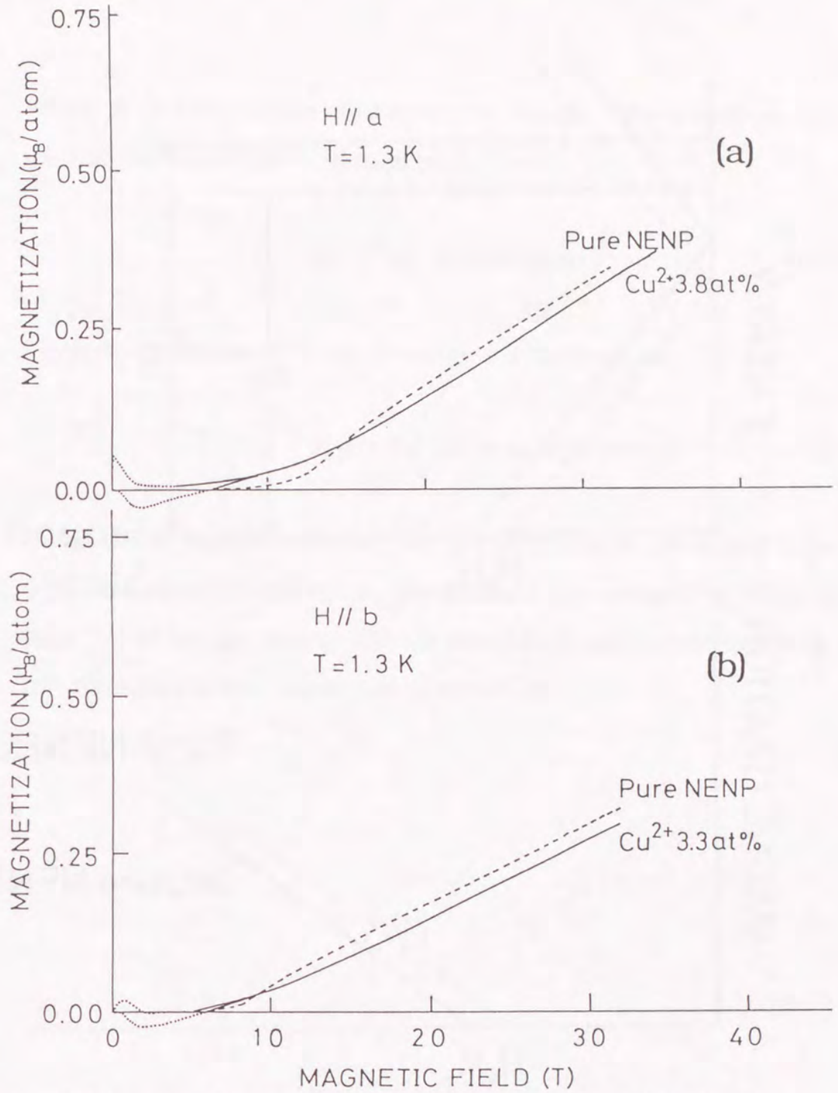


Fig. 6-2-1. (a) Magnetization curve of 3.8at% Cu : NENP (solid line) after subtraction of the paramagnetic contribution from the data shown in Fig. 6-1-1(a), and that of pure NENP (broken line). The dotted lines show the hysteric part of the magnetization curve in the impure sample.
(b) M-H curve of 3.3at% Cu : NENP (solid line) after subtraction of the paramagnetic contribution and that of pure NENP (broken line).

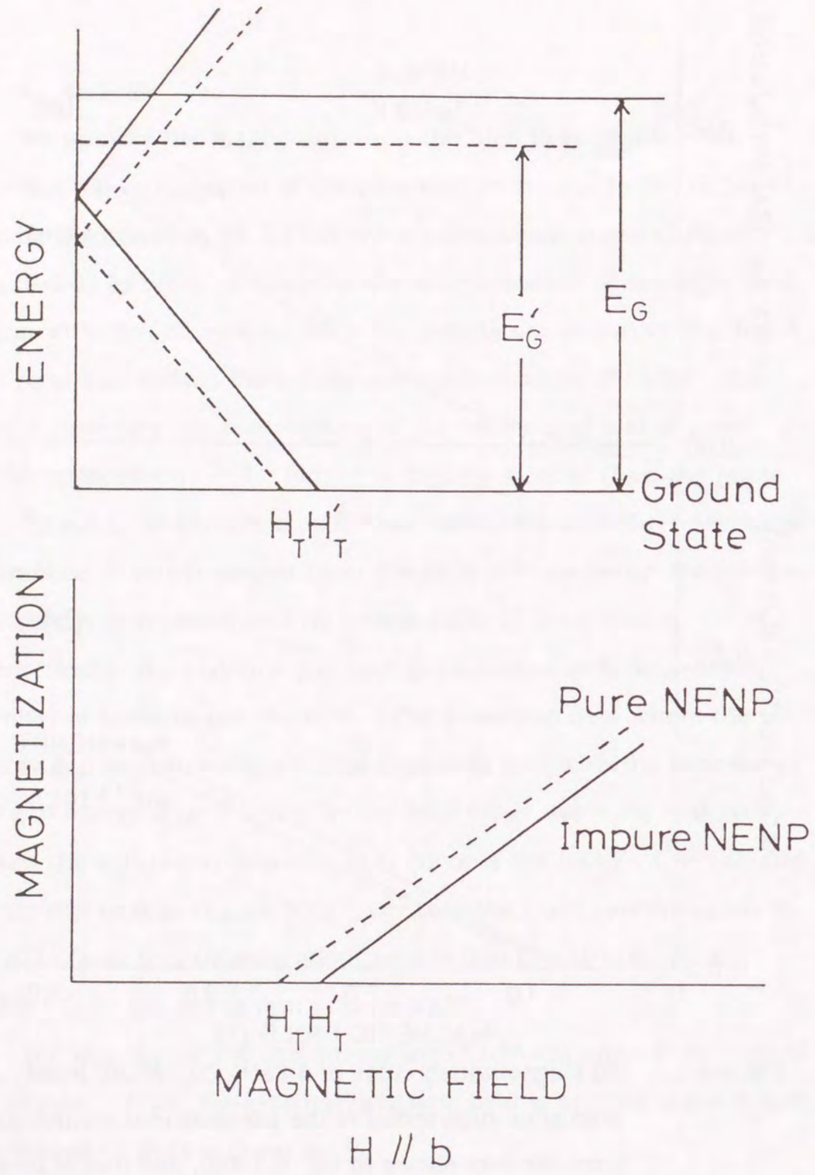


Fig. 6-2-2. A schematic presentation of the field dependence of the energy levels (upper part) and the magnetization curve (lower part). The solid and broken lines stand for impure and pure NENP, respectively.

where g_b is the g- value of Ni along the b-axis. The transition field for the impure NENP is written as,

$$H_T' = (E_G' - |D|/3)/g_b \mu_B . \qquad (6\text{-}2\text{-}2)$$

Then, the increase of the gap energy is expressed as,

$$\Delta E_G = E_G' - E_G = g_b \mu_B (H_T' - H_T). \qquad (6\text{-}2\text{-}3)$$

Using the experimental value, $H_T' - H_T \approx 1$ T, ΔE_G is estimated to be 3 K. On the other hand, the theoretical increase (see Fig. 1-2-1 at page 15) of the gap energy for the case of 30 spins corresponding to the concentration of 3.3 at% is at most 1 K.

§ 7. Spin 1/2 degrees of freedom in an undoped NENP

7-1. Background

In § 4 and § 5, we have discussed the novel ESR signals[88-90] observed in Cu doped NENP samples which are well explained by the model that the valence bonds are broken at the Cu sites resulting in the S=1/2 degrees of freedom at the Ni sites neighboring Cu atoms. Chronologically, the fractional spin was first observed by Hagiwara et al[88]. Subsequently, the S=1/2 degrees of freedom have been observed by Glarum et al.[92] in NENP doped with the non-magnetic atoms such as Zn, Cd and Hg. The ESR signals observed in NENP : Zn are shown in Fig. 7-1-1. We expect the presence of the S=1/2 degrees of freedom even in pure S=1 LCHA substances, since there is a possibility of finding finite magnetic chains in the sample broken from infinite chains by, for example, crystal defects. In this section, we report the observation of the S=1/2 degrees of freedom in an imperfect single crystal of NENP[93].

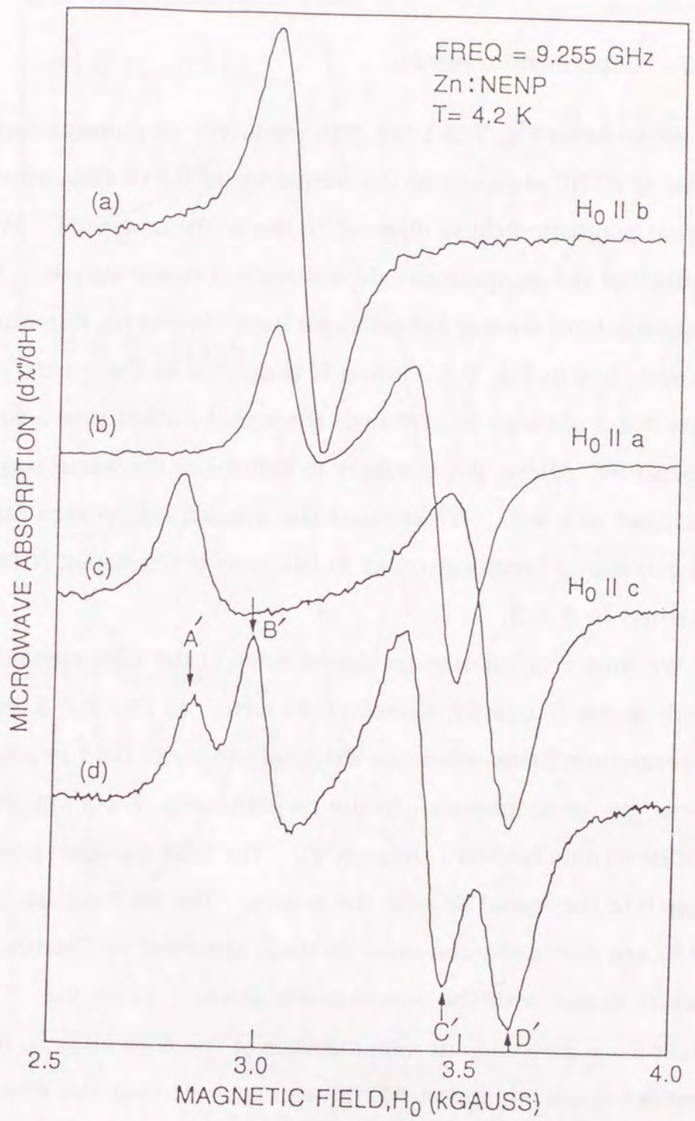


Fig. 7-1-1. ESR signals in NENP doped with the nonmagnetic Zn obtained by Glarum et al.. They defined the fields shown by the arrows (A', B', C' and D') as the resonance fields. (Quoted from ref. 92)

7-2. Experimental results

We show in Fig. 7-2-1 the ESR signals[93] in an imperfect single crystal of NENP obtained at the frequency of 9.216 GHz when the external magnetic field is directed to the a-, b- or c-axes. We have investigated the temperature dependence of these signals. Since all the signals have similar behavior, we have chosen for this study the rightmost line in Fig. 7-2-1 when H is applied to the a-axis.
Figure 7-2-2 shows a logarithm of the signal intensity as a function of temperature. Here, the intensity is defined in the same way as mentioned in § 4-2. We see that the intensity decreases rapidly with increasing temperature as in the case of Cu doped NENP presented in § 4-2.

We then studied angular dependence of the ESR signals of this sample at the frequency of about 9.22 GHz. In Fig. 7-2-3 are shown the resonance fields when the external magnetic field is rotated in the ca-, bc- or ab-planes. In the ca-plane (Fig. 7-2-3 (a)), there are six ESR signals labeled I through VI. The ESR signals I and II merge into the signal III near the a-axis. The ESR signals I, II, V and VI are essentially the same as those observed by Glarum et al.[92] in NENP doped with the nonmagnetic atoms. From the temperature and angular dependences of the ESR lines in the imperfect single crystal of NENP, we conclude that the ESR signals come from the S=1/2 degrees of freedom produced at the ends of finite chains.

In order to confirm further that we have observed the S=1/2 degrees of freedom, we have measured the magnetization of the very

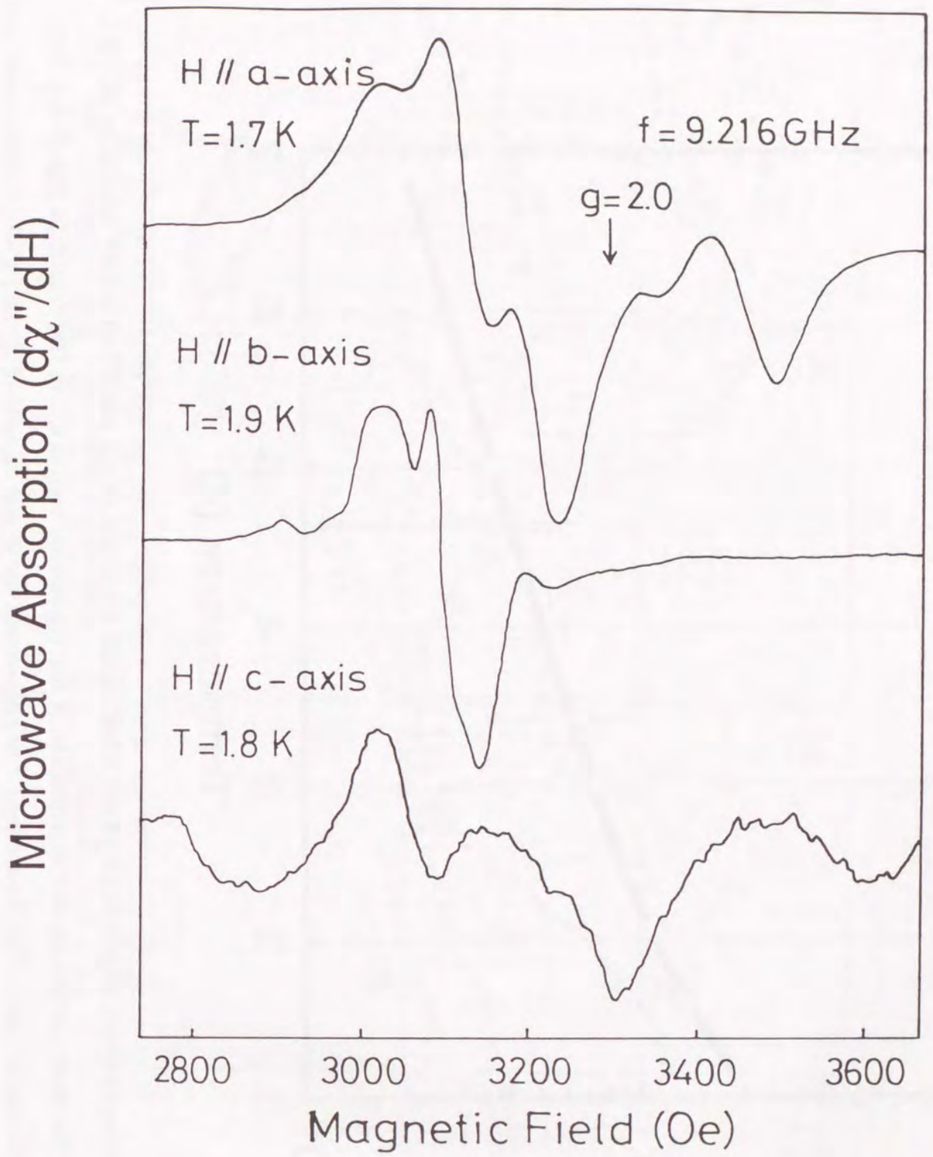


Fig. 7-2-1. ESR signals in an imperfect single crystal of NENP for the frequency of 9.216 GHz along the a-, b- and c-axes.

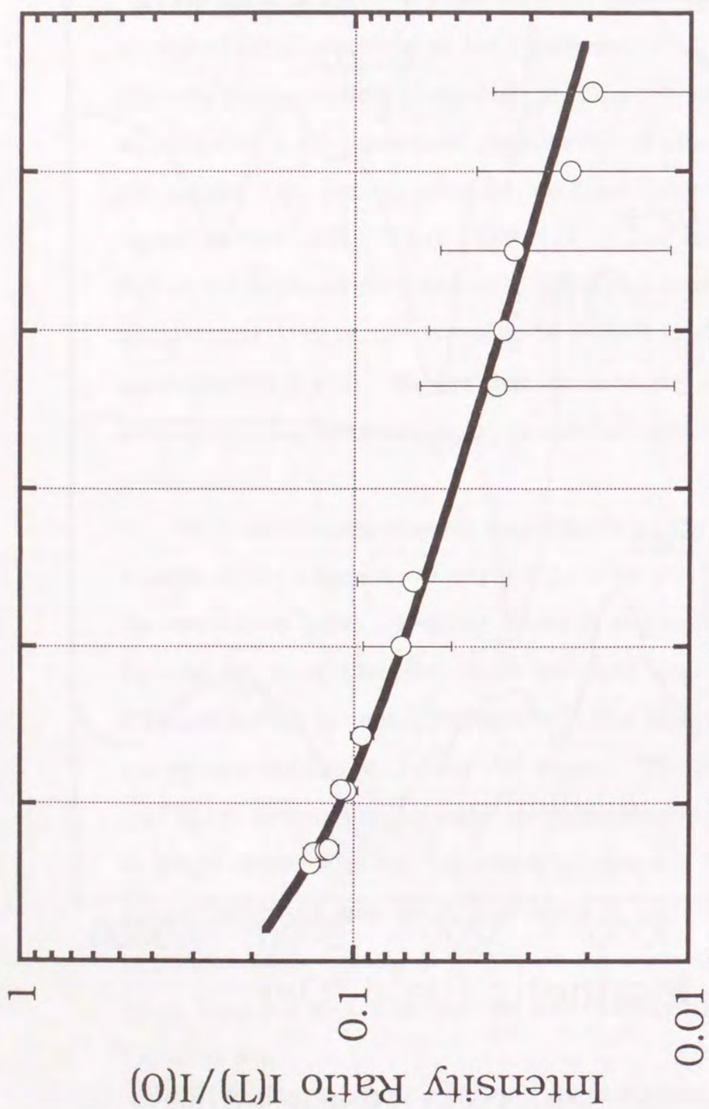


Fig. 7-2-2. Temperature dependence of the ESR signal intensity in an imperfect single crystal of NENP. The open circles show the intensity of the rightmost signal along the a-axis in Fig. 7-2-1 and the solid line is the theoretical one calculated by using Eqs. (5-2-2) and (5-2-3) with L_0=40 and L_{min}=30. L_{min} is the only one adjustable parameter. (See text)

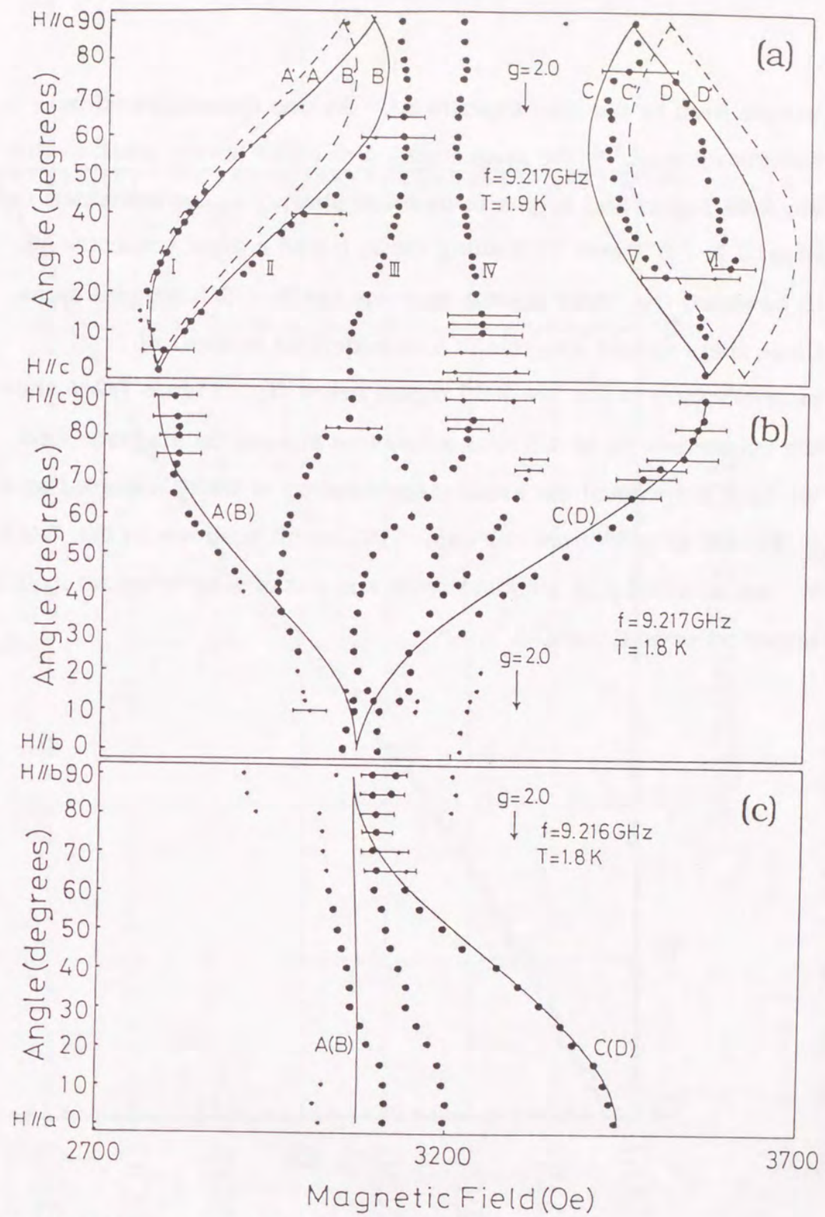


Fig. 7-2-3. Angular dependence of the ESR signals in an imperfect single crystal of NENP, when the external magnetic field is rotated in (a) the ac-plane, (b) cb-plane and (c) ba-plane. The solid (A, B, C and D) and broken (A', B', C' and D') lines represent the transition fields calculated with Eq. (7-3-3).

sample used in the ESR experiment. As was demonstrated by Katsumata et al.[78], the magnetization of NENP is very small in the low-field region and begins to increase sharply at the transition field (H_T=13 T, 7.5 T and 11 T along the a, b and c axes, respectively). If, however, the NENP crystal contains the S=1/2 fractional spins, these spins should give rise to a considerable amount of magnetization in the low field region below H_T. Figure 7-2-4 shows the magnetization at 4.2 K as a function of external magnetic field. We have subtracted the small magnetization of NENP observed at 4 K by Renard et al.[82] from our data. The result is shown in Fig. 7-2-5. We see in this figure a considerable amount of magnetization in the imperfect crystal sample.

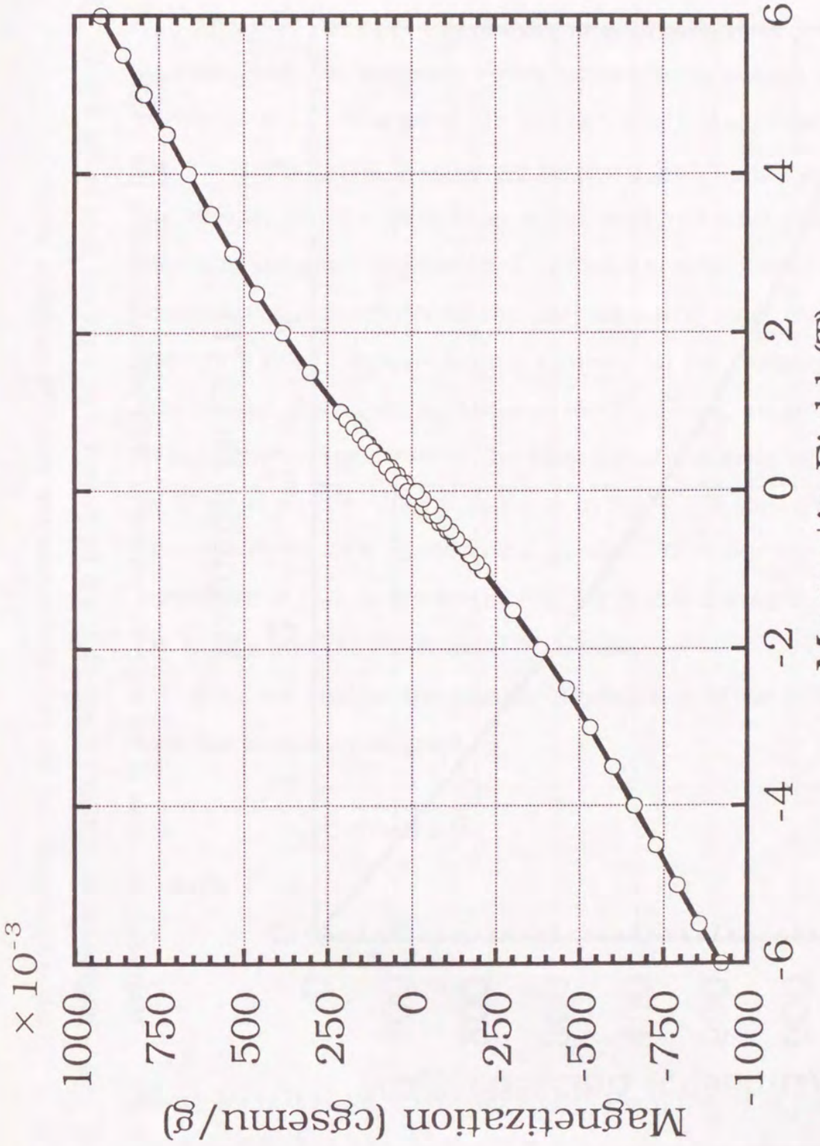


Fig. 7-2-4. Magnetization curve of the imperfect crystal of NENP at 4.2 K, when the external magnetic field is applied to the b-axis up to 6 T. The open circle shows the experimental data and the solid curve is a guide to the eyes.

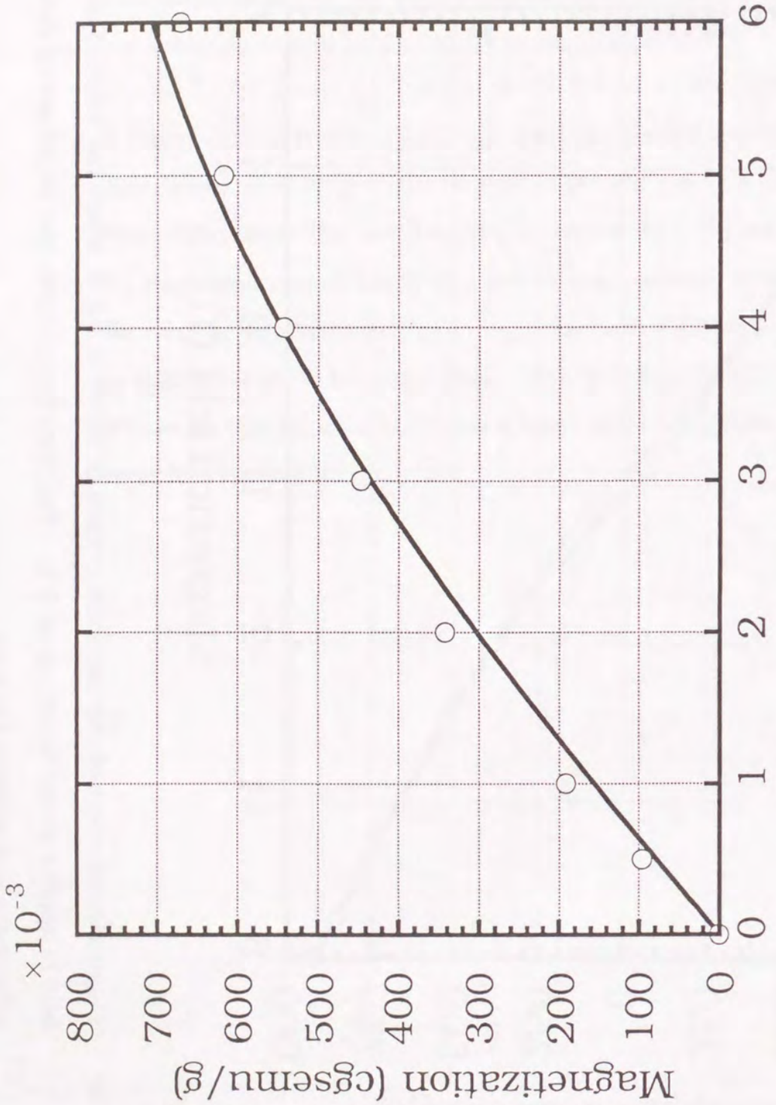


Fig. 7-2-5. Magnetization curve of the imperfect crystal of NENP after subtracting the small magnetization of NENP observed at 4 K by Renard et al. from our data in Fig. 7-2-4. The solid curve represents the S=1/2 Brillouin function with 5 % magnetic atoms.

7-3. Analysis

The solid curve in Fig. 7-2-5 represents the S=1/2 Brillouin function with 5% magnetic atoms (others are assumed to be nonmagnetic). This gives the average length (L_0) of forty Ni atoms for the finite chains, because we have one S=1/2 spin at each end of the chains. In the early stage of the work, we have proposed the phenomenological expression (Eq. (5-2-1)) to explain the temperature dependence of the ESR intensity, since we had no theory on this. Now we have the theory on the temperature dependence developed by Mitra et al[104]. Here, we compare the temperature dependence of the ESR signal intensity with the theory by Mitra et al.[104]. The solid curve in Fig. 7-2-2 shows the theoretical one with L_0=40 and L_{min}=30. The only one adjustable parameter is L_{min}. We see in Fig. 7-2-2 that the agreement between the theory and the experiment is satisfactory.

Next, we analyze the angular dependence of the ESR signals with the Hamiltonian given by,

$$\mathcal{H} = \mu_B \vec{s}\,\tilde{g}\,\vec{H}, \tag{7-3-1}$$

with

$$\tilde{g} = \begin{pmatrix} g_x & 0 & 0 \\ 0 & g_y & 0 \\ 0 & 0 & g_z \end{pmatrix}, \tag{7-3-2}$$

where $\vec{s}$(=1/2) is the fractional spin, $\tilde{g}$ the g tensor of that spin. The solid and dashed lines in Fig. 7-2-3 represent the standard formula for the angular dependence of the g value given by,

$$g^2 = g_x^2 \cos^2\theta + g_y^2 \sin^2\theta, \qquad (7\text{-}3\text{-}3)$$

where g_x and g_y are respectively the g values along the local principal axes x and y, and θ is the angle between $\vec{H}$ and the x axis.

In the ca-plane (Fig. 7-2-3 (a)), the broken lines labeled A' through D' represent the theoretical curves with the g-values obtained by Glarum et al.[92]. The lines C' and D' have the different local principal axes due to the two kinds of ligands around Ni atom which are formed by the ethylene diamine group with different configurations. The angle between the local principal axis of g_x and the a-axis is determined to be 31.4° (ref. 92) (Fig. 7-3-1 (a)). The lines A' and B' also have the different local principal axes. The angle that the local principal axis of g_x makes with the a-axis is 14° (ref. 92) (Fig. 7-3-1 (b)). We use the same angles for the fit of the lines A, B, C and D.

From the fit of the experimental data with Eq. (7-3-3), we obtain the following values,

$$\left.\begin{aligned} g_x^{A,B} &= 2.123 \\ g_y^{A,B} &= 2.382 \end{aligned}\right\}, \qquad (7\text{-}3\text{-}4)$$

for the lines A and B, and

$$\left.\begin{aligned} g_x^{C,D} &= 1.948 \\ g_y^{C,D} &= 1.812 \end{aligned}\right\}, \qquad (7\text{-}3\text{-}5)$$

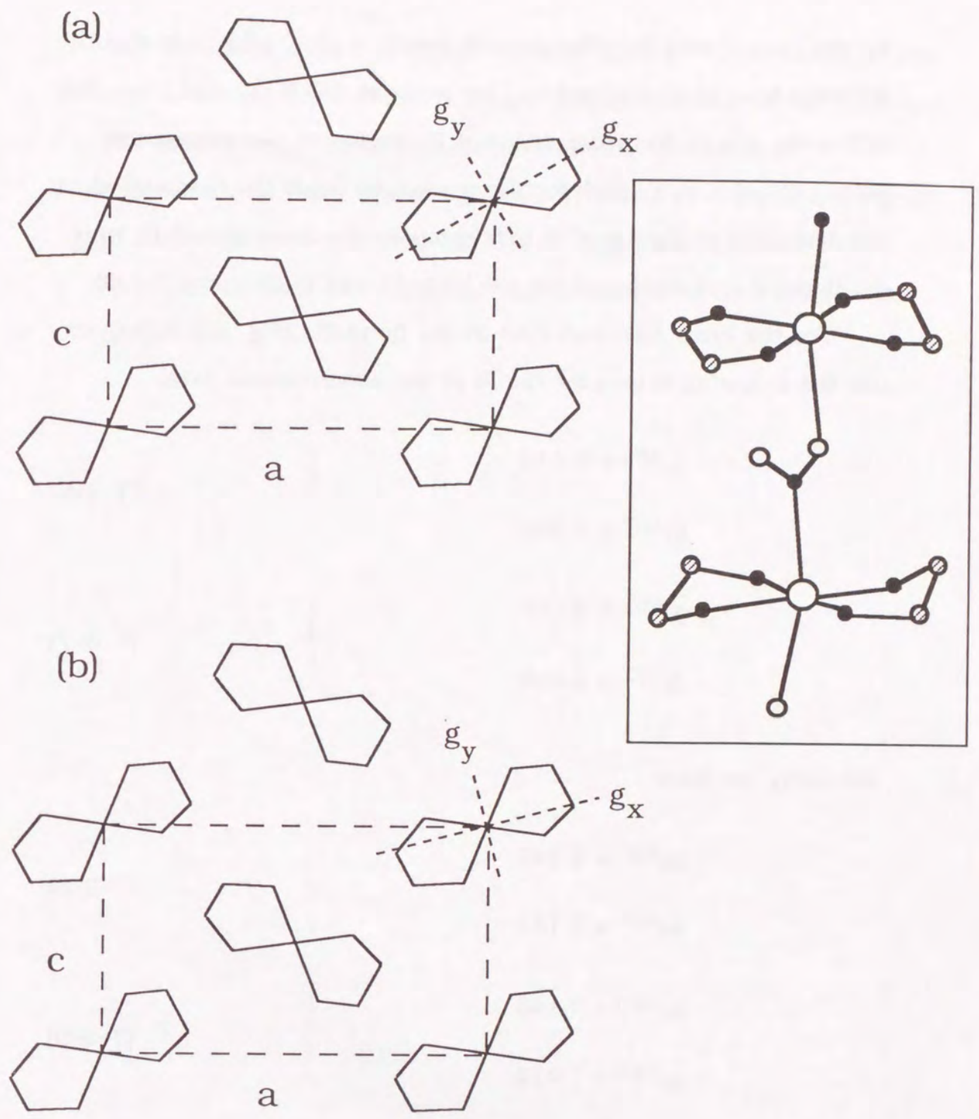


Fig. 7-3-1. Two kinds of the local principal axes (g_x and g_y) of the g tensor in the ac-plane observed in the ESR experiment[92]. Inset : Arrangement of the molecules around Ni^{2+} in NENP.

for the lines C and D. The present result (A, B, C and D) is slightly different from that obtained by Glarum et al. (A', B', C' and D'). This difference comes from the different definition of the resonance fields : Glarum et al. took for the resonance fields the fields at which the derivative of the signal is maximum for the lines A' and B', and the derivative is minimum for the lines C' and D' (See Fig. 7-1-1).

For the lines A(B) and C(D) in the bc-plane (Fig. 7-2-3 (b)), we use the following values for the fit of the experimental data,

$$\left.\begin{aligned} g_x^{A(B)} &= 2.146 \\ g_y^{A(B)} &= 2.368 \end{aligned}\right\}, \qquad (7\text{-}3\text{-}6)$$

$$\left.\begin{aligned} g_x^{C(D)} &= 2.146 \\ g_y^{C(D)} &= 1.850 \end{aligned}\right\}. \qquad (7\text{-}3\text{-}7)$$

Similarly, we have

$$\left.\begin{aligned} g_x^{A(B)} &= 2.146 \\ g_y^{A(B)} &= 2.139 \end{aligned}\right\}, \qquad (7\text{-}3\text{-}8)$$

$$\left.\begin{aligned} g_x^{C(D)} &= 2.146 \\ g_y^{C(D)} &= 1.912 \end{aligned}\right\}, \qquad (7\text{-}3\text{-}9)$$

for the lines A(B) and C(D) in the ab-plane (Fig. 7-2-3 (c)). In these cases, the local principal axes x and y correspond to the b- and c-axes, respectively, in the bc-plane, and to the b- and a-axes, respectively, in the ab-plane.

We see another two signals around 3200 Oe in the ca-plane (the signals III and IV). These two signals split into four in the bc-plane. The intensities of these signals have similar temperature dependence to those of the signals I, II, V and VI. Thus, the signals III and IV must come from the S=1/2 degrees of freedom. However, we have not yet succeeded in assigning their sites in the crystal.

§ 8. Conclusions

We have found novel ESR signals at X- and K-bands at low temperatures in NENP containing Cu impurity. The intensity of these signals decrease rapidly as temperature is increased. The resonance fields, and the temperature and angular dependences of the ESR signals are well explained by the following model based on the VBS state : when Ni atoms are substituted by Cu atoms, the valence bonds in the VBS state are broken at the impurity sites resulting in S=1/2 degrees of freedom at the Ni sites neighboring the Cu atoms.

Using this trimer model, we have also successfully explained the hyperfine lines observed in the ESR experiment and the magnetization of NENP : Cu. Moreover, we have observed the S=1/2 degrees of freedom in an undoped NENP through ESR and magnetization measurements.

Thus the present study provides the first experimental evidence for the existence of a fractional spin in magnetic system. At the same time, the ground state of an S=1 linear-chain Heisenberg antiferromagnet is shown to be well approximated by the VBS model. We hope that the present experiments will stimulate further study on quantum spin chains.

Acknowledgements

The author wishes to express his sincere gratitude to Doctor Koichi Katsumata of the Institute of Physical and Chemical Research (RIKEN), Guest professor of Research Center for Extreme Materials, Osaka University, for suggesting this problem and for continuous encouragement and enlightening discussions throughout the present work.

He is indebted to Professor Muneyuki Date of Osaka University for his variable suggestions and continuous encouragement in the present study.

He is grateful to Professor Jean-Pierre Renard of Université Paris-Sud, France for his collaboration on this work and for supplying single crystals of Cu doped NENP.

He wishes to acknowledge fruitful discussions with Professor Ian Affleck of University of British Columbia, Canada and Professor Bertrand I. Halperin of Harvard University, U.S.A..

He wishes to express his thanks to Professor Hidenobu Hori and Mr. Tetsuya Takeuchi for the high field magnetization measurements on Cu doped NENP.

He also would like to thank Doctor Taturu Yosida for his valuable suggestion concerning sample preparation.

Thanks are also due to the Inorganic Analysis Center and Chemical Analysis unit in the Instrumentation and Characterization Center in RIKEN for their skilful and precise work in the chemical analysis of the samples used in the present work.

Finally, the author would like to thank all the members of the Magnetic Materials Laboratory in RIKEN.

References

1) F. Bloch : Z. Physik **61** (1930) 206 ; Z. Physik **74** (1932) 295.

2) H. Bethe : Z. Physik **71** (1931) 205.

3) L. Hulthén : Arkiv. Mat. Astron. Fysik **26A** (1938) No.11.

4) R. Orbach : Phys. Rev. **112** (1958) 309.

5) L. R. Walker : Phys. Rev. **116** (1959) 1089.

6) C. N. Yang and C. P. Yang : Phys. Rev. **150** (1966) 321.

7) R. B. Griffiths : Phys. Rev. **133** (1964) A768.

8) J. C. Bonner and M. E. Fishier : Phys. Rev. **135** (1964) A640.

9) P. W. Anderson : Mat. Res. Bull **8** (1973) 153.

10) E. Lieb, T. Shultz and D. Mattis : Ann. Phys. **16** (1961) 407.

11) S. Katsura : Phys. Rev. **127** (1962) 1508.

12) E. Ising : Z. Phys. **31** (1925) 253.

13) M. Suzuki, B. Tsujiyama and S. Katsura : J. Math. Phys. **8** (1967) 124.

14) T. Obokata and T. Oguchi : J. Phys. Soc. Jpn. **25** (1968) 322.

15) M. E. Fisher : Amer. J. Phys. **32** (1964) 343.

16) T. Holstein and H. Primakoff : Phys. Rev. **58** (1940) 1098.

17) F. J. Dyson : Phys. Rev. **102** (1956) 1217,1230.

18) P. W. Anderson : Phys. Rev. **86** (1952) 694.

19) R. Kubo : Phys. Rev. **86** (1952) 929 ; Rev. Mod. Phys. **25** (1953) 344.

20) J. Des Cloizeaux and J. J. Pearson : Phys. Rev. **128** (1962) 2131.

21) K. Nakamura and T. Sasada : Phys. Lett. **48A** (1974) 321.

22) H. J. Mikeska : J. Phys. C : Solid State Phys. **11** (1978) L29.

23) H. J. Mikeska : J. Phys. C : Solid State Phys. **13** (1980) 2913.
24) J. Villain : Physica **79B** (1975) 1.
25) N. Ishimura and H. Shiba : Prog. Theor. Physics **63** (1980) 743.
26) See for a review including theory, L. J. de Jongh and A. R. Miedema : Adv. Phys. **23** (1974) 1.
27) See for a review including dynamic properties, M. Steiner, J. Villain and C. G. Windsor : Adv. Phys. **25** (1976) 87.
28) T. Oguchi : Phys. Rev. **133** (1964) A1098.
29) K. Takeda, S. Matsukawa and T. Haseda : J. Phys. Soc. Jpn. **30** (1971) 1330.
30) M. Date and M. Motokawa : Phys. Rev. Lett. **16** (1966) 1111.
31) M. Date and M. Motokawa : Bussei **6** (1965) 549. (In Japanese)
32) J. B. Torrance Jr and M. Tinkham : Phys. Rev. **187** (1969) 587.
33) R. E. Dietz, F. R. Merritt, R. Dingle, D. Hone. B. G. Silbernagel and P. M. Richards : Phys. Rev. Lett. **26** (1971) 1186.
34) K. Nagata and Y. Tazuke : J. Phys. Soc. Jpn. **32** (1972) 337.
35) Y. Endoh, G. Shirane, R. J. Birgeneau, P. M. Richards and S. L. Holt : Phys. Rev. Lett. **32** (1974) 170.
36) J. K. Kjems and M. Steiner : Phys. Rev. Lett. **41** (1978) 1137.
37) J. P. Boucher, L. P. Regnault, J. Rossat-Mignod, J. P. Renard, J. Bouillot and W. G. Stirling : Solid State Comm. **33** (1980) 171.
38) J. P. Boucher and J. P. Renard : Phys. Rev. Lett. **45** (1980) 486.
39) H. Yoshizawa, K. Hirakawa, S. K. Satija and G. Shirane : Phys. Rev. **B23** (1981) 2298.
40) J. M. Loveluck, T. Schneider, E. Stoll and H. R. Jauslin : Phys. Rev. Lett. **45** (1980) 1505.

41) G. Reiter : Phys. Rev. Lett. **46** (1981) 202.
42) H. J. Mikeska : J. Appl. Phys. **52** (1981) 1950.
43) F. D. M. Haldane : Phys. Lett. **93** (1983) 464, Phys. Rev. Lett. **50** (1983) 1153.
44) J. C. Bonner and G. Müller : Phys. Rev. **B29** (1984) 5216.
45) J. B. Parkinson and J. C. Bonner : Phys. Rev. **B32** (1985) 4703.
46) R. Botet and R. Jullien : Phys. Rev. **B27** (1983) 613.
47) R. Botet, R. Jullien and M. Kolb : Phys. Rev. **B28** (1983) 3914.
48) M. Kolb, R. Botet and R. Jullien : J. Phys. A: Math. Gen. **16** (1983) L673.
49) U. Glaus and T. Schneider : Phys. Rev. **B30** (1984) 215.
50) J. Sólyom and T. A. L. Ziman : Phys. Rev. **B30** (1984) 3980.
51) A. Moreo : Phys. Rev. **B35** (1987) 8562.
52) T. Sakai and M. Takahashi : Phys. Rev. **B42** (1990) 1090.
53) G. Gómez-Santos : Phys. Rev. Lett. **63** (1989) 790.
54) M. P. Nightingale and H. W. J. Blöte : Phys. Rev. **B33** (1986) 659.
55) K. Sogo and N. Uchinami : J. Phys. A : Math. Gen. **19** (1986) 493.
56) M. Takahashi : Phys. Rev. **B38** (1988) 5188 ; Phys. Rev. Lett. **62** (1989) 2313.
57) K. Nomura : Phys. Rev. **B40** (1989) 2421.
58) J. B. Parkinson, J. C. Bonner, G. Müller, M. P. Nightingale and H. W. J. Blöte : J. Appl. Phys. **57** (1985) 3319.
59) H. J. Schultz and T. Ziman : Phys. Rev. **B33** (1986) 6545.
60) J. Oitmaa, J. B. Parkinson and J. C. Bonner : J. Phys. C: Solid state phys. **19** (1986) L595.

61) K. Kubo and S. Takada : J. Phys. Soc. Jpn. **55** (1986) 438.

62) T. Delica, K. Kopinga, H. Leschke and K. K. Mon : Europhys. Lett. **15** (1991) 55.

63) J. Sólyom : Phys. Rev. **B36** (1987) 8642.

64) J. C. Bonner : J. Appl. Phys. **61** (1987) 3941.

65) I. Affleck, T. Kennedy, E. H. Lieb and H. Tasaki : Phys. Rev. Lett. **59** (1987) 799 ; Commun. Math. Phys. **115** (1988) 477.

66) For a review see, I. Affleck : J. Phys.: Condens. Matt. **1** (1989) 3047.

67) I. Affleck : Phys. Rev. Lett. **62** (1989) 474.

68) H. Tasaki : Phys. Rev. Lett. **64** (1990) 2066.

69) T. Sakai and M. Takahashi : Phys. Rev. **B42** (1990) 4537.

70) T. Kennedy : J. Phys.: Condens. Matt. **2** (1990) 5737.

71) T. Kennedy and H. Tasaki : Phys. Rev. **B45** (1992) 304. ; preprint

72) W. J. L. Buyers, R. M. Morra, R. L. Armstrong, M. J. Hogan, P. Gerlach and K. Hirakawa : Phys. Rev. Lett. **56** (1986) 371.

73) M. Steiner, K. Kakurai, J. K. Kjems, D. Petitgrand and R. Pynn : J. Appl. Phys. **61** (1987) 3953.

74) J. P. Renard, M. Verdaguer, L. P. Regnault, W. A. C. Erkelens, J. Rossat-Mignod and W. G. Stirling : Europhys. Lett. **3** (1987) 945.

75) J. P. Renard, M. Verdaguer, L. P. Regnault, W. A. C. Erkelens, J. Rossat-Mignod, J. Ribas, W. G. Stirling and C. Vettier : J. Appl. Phys. **63** (1988) 3538.

76) J. P. Renard, L. P. Regnault and M. Verdaguer : J. Physique **49** (1988) C8-1425.

77) J. Ferré, J. P. Jamet, C. P. Landee, K. A. Reza and J. P. Renard : J. Physique **49** (1988) C8-1441.

78) K. Katsumata, H. Hori, T. Takeuchi, M. Date, A. Yamagishi and J. P. Renard : Phys. Rev. Lett. **63** (1989) 86.

79) M. Date and K. Kindo : Phys. Rev. Lett. **65** (1990) 1659.

80) W. Lu, J. Tuchendler, M. von Ortenberg and J. P. Renard : Phys. Rev. Lett. **67** (1991) 3716.

81) W. Palme, H. Kriegelstein, B. Lüthi, T. M. Brill, T. Yosida and M. Date : Preprint

82) J. P. Renard, V. Gadet, L. P. Regnault and M. Verdaguer : J. Magn. & Magn. Mater. **90&91** (1990) 213.

83) J. P. Boucher : Hyperfine Interactions **49** (1989) 423.

84) P. Gaveau, J. P. Boucher, L. P. Regnault and J. P. Renard : Europhys. Lett. **12**(7) (1990) 647.

85) M. Chiba, Y. Ajiro, H. Kikuchi, T. Kubo and T. Morimoto : J. Magn. & Magn. Mater. **90&91** (1990) 221 ; Phys. Rev. **B44** (1991) 2838.

86) N. Fujiwara, T. Goto, T. Kohmoto and S. Maegawa : J. Magn. & Magn. Mater. **90&91** (1990) 229 ; preprint.

87) T. Kobayashi, Y. Tabuchi, K. Amaya, Y. Ajiro, T. Yosida and M. Date : J. Phys. Soc. Jpn **61** (1992) 1772.

88) M. Hagiwara, K. Katsumata, I. Affleck, B. I. Halperin and J. P. Renard : Phys. Rev. Lett. **65** (1990) 3181.

89) M. Hagiwara and K. Katsumata : Mod. Phys. Lett. **B5** (1991) 741.

90) M. Hagiwara, K. Katsumata, J. P. Renard, I. Affleck and B. I. Halperin : J. Magn. & Magn. Mater. **104-107** (1992) 839.

91) M. Hagiwara, K. Katsumata, H. Hori, T. Takeuchi, M. Date, A. Yamagishi, J. P. Renard and I. Affleck : Physica **B177** (1992) 386.

92) S. H. Glarum, S. Geschwind, K. M. Lee, M. L. Kaplan and J. Michel : Phys. Rev. Lett. **67** (1991) 1614.

93) M. Hagiwara and K. Katsumata : J. Phys. Soc. Jpn. **61** (1992) 1481.

94) V. Gadet, M. Verdaguer, V. Brios, A. Gleizes, J. P. Renard, P. Beauvillain, C. Chappert, T. Goto, K. Le Dang and P. Veillet : Phys. Rev. **B 44** (1991) 705.

95) N. Achiwa : J. Phys. Soc. Jpn. **27** (1969) 561.

96) A. Meyer, A. Gleizes, J. J. Girerd, M. Verdaguer and O. Kahn : Inorg. Chem. **21** (1982) 1729.

97) J. B. Goodenough : Phys. Rev. **100** (1955) 564.

98) J. Kanamori : J. Phys. Chem. Solids **10** (1959) 87.

99) I. Affleck : Private communication

100) O. V. Lounasmaa : " Experimental Principles and Methods below 1 K" (Academic Press 1974) Chap. 7.

101) T. Sakakibara, H. Mollymoto, M. Motokawa and M. Date : "High Field Magnetism" ed. M. Date (North Holland Company, 1983) 299.

102) T. Takeuchi : Master Thesis, Osaka University (1990).

103) Y. Ting and H. Lew : Phys. Rev. **105** (1957) 581.

104) P. P. Mitra, B. I. Halperin and I. Affleck : Phys. Rev. **B45** (1992) 5299.

105) A. H. Maki and B. R. McGarvey : J. Chem. Physics **29** (1958) 31.

106) D. Kivelson and R. Neiman : J. Chem. Phys. **35** (1961) 149.

107) H. R. Gersmann and J. D. Swalen : J. Chem. Phys. **36** (1962) 3221.

108) A. Abragam and M. H. L. Pryce : Proc. Roy. Soc. (London) **A206** (1951) 164.

109) H. Mollymoto : Ph. D. Thesis, Osaka University (1980).

110) A. Abragam and B. Bleaney : "Electron Paramagnetic Resonance of Transition Ions", 2nd eds. (Dover Pub., Inc., New York, 1986).

Appendix I

The hyperfine lines in the present model

In this appendix, we calculate the eigen states and eigen functions of the Hamiltonian (5-5-1) given by,

$$\mathcal{H} = -2J(\vec{S_1}+\vec{S_2})\vec{s}+g\,\mu_B H\,(S_1^z + S_2^z + s^z)+A_{//}\,I^z s^z+A_{\perp}\,(I^x s^x+I^y s^y) \quad \text{.(AI-1)}$$

We regard the former two terms as a non-perturbing Hamiltonian and the latter two terms as a perturbing one. Here, we define the resultant spin of $\vec{S}_1$ and $\vec{S}_2$ as $\vec{S'}$, and the resultant spin of this $\vec{S'}$ and $\vec{s}$ as $\vec{S}$. We find easily the eigen functions for the non-perturbing Hamiltonian. The eigen functions are shown below :

$$\begin{array}{ll}
\left.\begin{array}{l}
\Phi_{\frac{3}{2},\,m} = \alpha_1\alpha_2\alpha|m> \\
\Phi_{\frac{1}{2},m} = \frac{1}{\sqrt{3}}(\beta_1\alpha_2\alpha+\alpha_1\beta_2\alpha+\alpha_1\alpha_2\beta)|m> \\
\Phi_{\frac{-1}{2},m} = \frac{1}{\sqrt{3}}(\alpha_1\beta_2\beta+\beta_1\alpha_2\beta+\beta_1\beta_2\alpha)|m> \\
\Phi_{\frac{-3}{2},\,m} = \beta_1\beta_2\beta|m>
\end{array}\right\} & S=3/2,\ (S'=1) \\
\left.\begin{array}{l}
\xi_{\frac{1}{2},m} = -\frac{1}{\sqrt{6}}(\alpha_1\beta_2\alpha+\beta_1\alpha_2\alpha-2\alpha_1\alpha_2\beta)|m> \\
\xi_{\frac{-1}{2},m} = \frac{1}{\sqrt{6}}(\alpha_1\beta_2\beta+\beta_1\alpha_2\beta-2\beta_1\beta_2\alpha)|m>
\end{array}\right\} & S=1/2,\ (S'=1) \\
\left.\begin{array}{l}
\eta_{\frac{1}{2},m} = \frac{1}{\sqrt{2}}(\alpha_1\beta_2\alpha-\beta_1\alpha_2\alpha)|m> \\
\eta_{\frac{-1}{2},m} = \frac{1}{\sqrt{2}}(\alpha_1\beta_2\beta-\beta_1\alpha_2\beta)|m>
\end{array}\right\} & S=1/2,\ (S'=0)
\end{array} \quad \text{, (AI-2)}$$

where α_1 and β_1 denote the eigen states of spin 1/2 and the others are defined similarly, $|m>$ is the nuclear spin states with magnetic quantum number m.

Accordingly, the eigen states for the Hamiltonian (AI-1) are calculated with the wave functions in (AI-2) using the first-order-perturbation theory. The eigen states may be written as,

$$\begin{array}{ll}
\left.\begin{array}{ll}
S_m = \frac{3}{2} & W_1 = -J + \frac{3}{2}g\,\mu_B H + \frac{A_{//}}{2}\,m \\
S_m = \frac{1}{2} & W_2 = -J + \frac{1}{2}g\,\mu_B H + \frac{A_{//}}{6}\,m \\
S_m = -\frac{1}{2} & W_3 = -J - \frac{1}{2}g\,\mu_B H - \frac{A_{//}}{6}\,m \\
S_m = -\frac{3}{2} & W_4 = -J - \frac{3}{2}g\,\mu_B H - \frac{A_{//}}{2}\,m
\end{array}\right. & \\
\left.\begin{array}{ll}
S_m = \frac{1}{2} & W_5 = 2J + \frac{1}{2}\,g\,\mu_B H - \frac{A_{//}}{6}\,m \\
S_m = -\frac{1}{2} & W_6 = 2J - \frac{1}{2}\,g\,\mu_B H + \frac{A_{//}}{6}\,m
\end{array}\right. & S=1/2,\ (S'=1) \\
\left.\begin{array}{ll}
S_m = \frac{1}{2} & W_7 = \frac{1}{2}\,g\,\mu_B H + \frac{A_{//}}{2}\,m \\
S_m = -\frac{1}{2} & W_8 = -\frac{1}{2}\,g\,\mu_B H - \frac{A_{//}}{2}\,m
\end{array}\right. & S=1/2,\ (S'=0)
\end{array} \quad \text{. (AI-3)}$$

The conditions for allowed transitions in the ordinary ESR are $\Delta S_m=\pm 1$ and $\Delta m=0$. Then, the resonance fields are obtained as,

$$\begin{array}{lll}
\left.\begin{array}{ll}
\Delta S_{\frac{3}{2}\leftrightarrow\frac{1}{2}} & h\nu_0 = g\,\mu_B H + \frac{A_{//}}{3}\,m \\
\Delta S_{\frac{1}{2}\leftrightarrow-\frac{1}{2}} & h\nu_0 = g\,\mu_B H + \frac{A_{//}}{3}\,m \\
\Delta S_{-\frac{1}{2}\leftrightarrow-\frac{3}{2}} & h\nu_0 = g\,\mu_B H + \frac{A_{//}}{3}\,m
\end{array}\right. & S=3/2,\ (S'=1) \\
\Delta S_{\frac{1}{2}\leftrightarrow-\frac{1}{2}} & h\nu_0 = g\,\mu_B H + \frac{A_{//}}{3}\,m & S=1/2,\ (S'=1) \\
\Delta S_{\frac{1}{2}\leftrightarrow-\frac{1}{2}} & h\nu_0 = g\,\mu_B H + A_{//}\,m & S=1/2,\ (S'=0)
\end{array} \quad \text{. (AI-4)}$$

As is seen from Eq. (AI-4), we have two kinds of line splittings in the hyperfine lines in the present model.

Appendix II

The angular dependence of the hyperfine lines

The resonance fields of hyperfine lines[110] are calculated with the Hamiltonian (5-5-4) (P.81) as follows :

$$\mathcal{H} = g^{z}_{Cu}\mu_B s^z H\cos\theta + g^{x}_{Cu}\mu_B s^x H\sin\theta + A_{//} I^z s^z + A_{\perp}(I^x s^x + I^y s^y) \quad \text{(AII-1)}$$

The Zeeman terms, which we assume to be larger than the hyperfine terms, are first diagonalized by rotating the coordinate system about the y-axis by an angle ϕ.

$$s^z = s_z'\cos\phi - s_x'\sin\phi, \quad \text{(AII-2)}$$

$$s^x = s_z'\sin\phi + s_x'\cos\phi. \quad \text{(AII-3)}$$

Then the Hamiltonian (AII-1) is written as,

$$\mathcal{H} = \mu_B H\{s'_x(g^{x}_{Cu}\sin\theta\cos\phi - g^{z}_{Cu}\cos\theta\sin\phi) + s'_z(g^{x}_{Cu}\sin\theta\sin\phi + g^{z}_{Cu}\cos\theta\cos\phi)\}$$
$$+ A_{//}(s'_z\cos\phi - s'_x\sin\phi)I^z + A_{\perp}(s'_z I^x\sin\phi + s_x I^x\cos\phi + s'_y I^y), \quad \text{(AII-4)}$$

and the coefficient of s_x' in the Zeeman term vanishes by choosing the angle ϕ such that,

$$\tan\phi = (g^{x}_{Cu}/g^{z}_{Cu})\tan\theta. \quad \text{(AII-5)}$$

If we define g by the equation

$$g^2 = g^x{}_{Cu}{}^2 \sin^2\theta + g^z{}_{Cu}{}^2 \cos^2\theta, \qquad \text{(AII-6)}$$

we have

$$\sin\phi = (g^x{}_{Cu} / g)\sin\theta,\ \cos\phi = (g^z{}_{Cu} / g)\cos\theta, \qquad \text{(AII-7)}$$

and the Hamiltonian is given by,

$$\mathcal{H} = g\mu_B H s'_z + s'_x (- A_{//} \sin\phi I^z + A_\perp \cos\phi I^x) + s'_y A_\perp I^y + s'_z (A_{//} \cos\phi I^z + A_\perp \sin\phi I^x) \quad \text{(AII-8)}$$

The coordinate system is then rotated by an angle ψ about the y-axis.

$$I^z = I_z' \cos\psi - I_x' \sin\psi, \qquad \text{(AII-9)}$$

$$I^x = I_z' \cos\psi + I_x' \cos\psi, \qquad \text{(AII-10)}$$

$$I^y = I_y'. \qquad \text{(AII-11)}$$

Then

$$\mathcal{H} = g\mu_B H s'_z + s'_x I'_x (A_{//} \sin\phi \sin\psi + A_\perp \cos\phi \cos\psi) + s'_x I'_z (- A_{//} \sin\phi \cos\psi + A_\perp \cos\phi \sin\psi) + s'_y I'_y A_\perp + s'_z I'_x (- A_{//} \cos\phi \sin\psi + A_\perp \sin\phi \cos\psi) + s_z I_z (A_{//} \cos\phi \cos\psi + A_\perp \sin\phi \sin\psi) \quad \text{(AII-12)}$$

and the coefficient of $s_z'I_x'$ vanishes by choosing the angle ψ such as,

$$\tan\psi = (A_\perp / A_{//}) \tan\phi = (A_\perp g^x{}_{Cu} / A_{//} g^z{}_{Cu}) \tan\theta. \qquad \text{(AII-13)}$$

The term in $s_z'I_z'$ may be written as $As_z'I_z'$, where

$$g^2 A^2 = g^z{}_{Cu}{}^2 A_{//}{}^2 \cos^2\theta + g^x{}_{Cu}{}^2 A_\perp{}^2 \sin^2\theta. \qquad \text{(AII-14)}$$

Finally, the Hamiltonian can be written as,

$$\mathcal{H} = g\mu_B H s'_z + A s'_z I'_z + s'_y I'_y A_\perp + s'_x [I'_x A_{//} A_\perp / A + I'_z g^x_{Cu} g^z_{Cu} \sin 2\theta (A_\perp^2 - A_{//}^2) / 2g^2 A] . \qquad \text{(AII-15)}$$

By using first- and second-order perturbation theory, the energies of the states are calculated as,

$$W\, s_m, m = g\mu_B H s_m + A s_m m - m(A_{//} A_\perp{}^2 / 4A\, g\mu_B H) + (A_{//}{}^2 + A^2)(A_\perp{}^2 / 4A^2 g\mu_B H) s_m \{ I(I+1) - m^2 \} - [\{ A_{//}{}^2 - A_\perp{}^2)^2 / 8A^2 g\mu_B H \} (g^z{}_{Cu}\, g^x{}_{Cu} / g^2)^2 \sin^2 2\theta] s_m m^2 , \qquad \text{(AII-16)}$$

where s_m is magnetic quantum number of Cu electron spin and m is magnetic quantum number of Cu nuclear spin.
Thus, the transition fields are obtained under the condition of $\Delta s_m = \pm 1$, $\Delta m = 0$ as,

$$h\nu_0 = g\,\mu_B H + Am + (A_{//}^2 + A^2)(A_\perp^2/4A^2 g\,\mu_B H)\{I(I+1)-m^2\} - [\{(A_{//}^2 - A_\perp^2)^2/8A^2 g\,\mu_B H\}(g^z_{Cu}\, g^x_{Cu}/g^2)^2 \sin^2 2\theta]m^2 . \quad \text{(AII-17)}$$

Consequently, the resonance fields are given as a function of angle by,

$$H_{s_m,\,m} = \{(h\nu_0 - Am) + \sqrt{(h\nu_0 - Am)^2 - (A_{//}^2 + A^2)(A_\perp^2/A^2)\{I(I+1)-m^2\} + [\{(A_{//}^2 - A_\perp^2)^2/2A^2\}(g^z_{Cu}\, g^z_{Cu}/g^2)^2 \sin^2 2\theta]m^2}\}/2g\,\mu_B \quad \text{(AII-18)}$$

Appendix III

Calculation of the magnetization curve

We calculate the eigen states of the Hamiltonian (5-1-1) exactly and the magnetization analytically, when the external magnetic field is applied to the z-axis. In this case, the Hamiltonian is given by,

$$\mathcal{H} = -2\{J_x(S_1^x + S_2^x)s^x + J_y(S_1^y + S_2^y)s^y + J_z(S_1^z + S_2^z)s^z\} + g\,\mu_B H(S_1^z + S_2^z) + g'\,\mu_B H s^z , \quad \text{(AIII-1)}$$

where $g = g^z_{Ni}$ and $g' = g^z_{Cu}$.

The eigen states are calculated in the following way. The secular equation to obtain the eigen states is written as,

	$\lvert+\rangle\lvert\frac{1}{2}\rangle$	$\lvert+\rangle\lvert\frac{1}{2}\rangle$	$\lvert0\rangle\lvert\frac{1}{2}\rangle$	$\lvert0\rangle\lvert\frac{1}{2}\rangle$	$\lvert-\rangle\lvert\frac{1}{2}\rangle$	$\lvert-\rangle\lvert\frac{1}{2}\rangle$	$\lvert0\rangle\lvert\frac{1}{2}\rangle$	$\lvert0\rangle\lvert\frac{1}{2}\rangle$	
$\langle\frac{1}{2}\lvert+\rvert$	J/2+G +G'/2-W	0	0	$\sqrt{2}\triangle$	0	0	0	0	
$\langle\frac{1}{2}\lvert+\rvert$	0	-J/2+G -G'/2-W	$\sqrt{2}$ J	0	0	0	0	0	
$\langle\frac{1}{2}\lvert0\rvert$	0	$\sqrt{2}$ J	G'/2-W	0	0	$\sqrt{2}\triangle$	0	0	
$\langle\frac{1}{2}\lvert0\rvert$	$\sqrt{2}\triangle$	0	0	-G'/2-W	$\sqrt{2}$ J	0	0	0	= 0
$\langle\frac{1}{2}\lvert-\rvert$	0	0	0	$\sqrt{2}$ J	-J/2-G +G'/2-W	0	0	0	
$\langle\frac{1}{2}\lvert-\rvert$	0	0	$\sqrt{2}\triangle$	0	0	J/2-G -G'/2-W	0	0	
$\langle\frac{1}{2}\lvert0\rvert$	0	0	0	0	0	0	G'/2-W	0	, (AIII-2)
$\langle\frac{1}{2}\lvert0\rvert$	0	0	0	0	0	0	0	-G'/2-W	

where $J=-2J_z$, $\Delta=-1/2(J_x-J_y)$, $j=-1/2(J_x+J_y)$, $G=g\mu_B H$, $G'=g'\mu_B H$ and W the eigen value. The states $|+>$, $|0>$, $|->$ and $|0>'$ represent those of the resultant spin $\vec{S}'$ composed of $\vec{S}_1$ and $\vec{S}_2$, and $|1/2>$ and $|-1/2>$ the eigen states of $\vec{s}$, respectively. These are given by

$$\begin{cases} S'=1 & \begin{cases} |+> = \alpha_1 \alpha_2 \\ |0> = \frac{1}{\sqrt{2}}(\alpha_1 \beta_2 + \beta_1 \alpha_2) \\ |-> = \beta_1 \beta_2 \end{cases} \\ S'=0 & |0>' = \frac{1}{\sqrt{2}}(\alpha_1 \beta_2 - \beta_1 \alpha_2) \end{cases} , \qquad \text{(AIII-3)}$$

where α and β have the usual meaning. The determinant (AIII-2) is decomposed into the following two parts :

	$\|+>\|\frac{1}{2}>$	$\|+>\|\frac{1}{2}>$	$\|0>\|\frac{1}{2}>$	$\|0>\|\frac{1}{2}>$	$\|->\|\frac{1}{2}>$	$\|->\|\frac{1}{2}>$
$<\frac{1}{2}\|<+\|$	$J/2+G+G'/2-W$	0	0	$\sqrt{2}\Delta$	0	0
$<\frac{1}{2}\|<+\|$	0	$-J/2+G-G'/2-W$	$\sqrt{2}\,j$	0	0	0
$<\frac{1}{2}\|<0\|$	0	$\sqrt{2}\,j$	$G'/2-W$	0	0	$\sqrt{2}\Delta$
$<\frac{1}{2}\|<0\|$	$\sqrt{2}\Delta$	0	0	$-G'/2-W$	$\sqrt{2}\,j$	0
$<\frac{1}{2}\|<-\|$	0	0	0	$\sqrt{2}\,j$	$-J/2-G+G'/2-W$	0
$<\frac{1}{2}\|<-\|$	0	0	$\sqrt{2}\Delta$	0	0	$J/2-G-G'/2-W$

$= 0$, (AIII-4)

and

	$\|0>\|\frac{1}{2}>$	$\|0>\|\frac{1}{2}>$
$<\frac{1}{2}\|<0\|$	$G'/2-W$	0
$<\frac{1}{2}\|<0\|$	0	$-G'/2-W$

$= 0$. (AIII-5)

The determinant (AIII-4) is written as,

$J/2+G+G'/2-W$	$\sqrt{2}\Delta$	0	0	0	0
$\sqrt{2}\Delta$	$-G'/2-W$	$\sqrt{2}\,j$	0	0	0
0	$\sqrt{2}\,j$	$-J/2-G+G'/2-W$	0	0	0
0	0	0	$-J/2+G-G'/2-W$	$\sqrt{2}\,j$	0
0	0	0	$\sqrt{2}\,j$	$G'/2-W$	$\sqrt{2}\Delta$
0	0	0	0	$\sqrt{2}\Delta$	$J/2-G-G'/2-W$

$= 0$. (AIII-6)

Then, this determinant is decomposed into two components written as,

$J/2+G+G'/2-W$	$\sqrt{2}\Delta$	0
$\sqrt{2}\Delta$	$-G'/2-W$	$\sqrt{2}\,j$
0	$\sqrt{2}\,j$	$-J/2-G+G'/2-W$

$= 0$, (AIII-7)

$-J/2+G-G'/2-W$	$\sqrt{2}\,j$	0
$\sqrt{2}\,j$	$G'/2-W$	$\sqrt{2}\Delta$
0	$\sqrt{2}\Delta$	$J/2-G-G'/2-W$

$= 0$. (AIII-8)

Thus, we obtain the following equations :

$$W^3+a_iW^2+b_iW+c_i=0 \qquad (i=1,2), \tag{AIII-9}$$

where

$$\left.\begin{aligned} a_1 &= -\frac{G'}{2} \\ b_1 &= -\{ \frac{G'}{4} +(\frac{J}{2} +G)^2+2(\Delta^2+j^2)\} \\ c_1 &= \frac{G'^3}{8} -(\frac{J}{2} +G)^2 \frac{G'}{2} +j^2J+2j^2G +j^2G'-\Delta^2J-2\Delta^2G +\Delta^2G' \\ a_2 &= \frac{G'}{2} \\ b_2 &= -\{ \frac{G'}{4} +(\frac{J}{2} -G)^2+2(\Delta^2+j^2)\} \\ c_2 &= - \frac{G'^3}{8} +(\frac{J}{2} -G)^2 \frac{G'}{2} +j^2J-2j^2G -j^2G'-\Delta^2J+2\Delta^2G-\Delta^2G' \end{aligned}\right\}, \tag{AIII-10}$$

and

$$W_7 = \frac{g' \mu_B H}{2}, \tag{AIII-11}$$

$$W_8 = - \frac{g' \mu_B H}{2}. \tag{AIII-12}$$

The cubic equations (AIII-9) are solved exactly, and the solutions are obtained as follows :

$$W_1 = R_1 \cos\frac{\theta_1}{3} + \frac{g' \mu_B H}{6}, \tag{AIII-13}$$

$$W_2 = R_1 \cos\frac{\theta_1+2\pi}{3} + \frac{g' \mu_B H}{6}, \tag{AIII-14}$$

$$W_3 = R_1 \cos\frac{\theta_1+4\pi}{3} + \frac{g' \mu_B H}{6}, \tag{AIII-15}$$

$$W_4 = R_2 \cos\frac{\theta_2}{3} - \frac{g' \mu_B H}{6}, \tag{AIII-16}$$

$$W_5 = R_2 \cos\frac{\theta_2+2\pi}{3} - \frac{g' \mu_B H}{6}, \tag{AIII-17}$$

$$W_6 = R_2 \cos\frac{\theta_2+4\pi}{3} - \frac{g' \mu_B H}{6}, \tag{AIII-18}$$

where

$$\left.\begin{aligned} R_1 &= \frac{2}{3}\sqrt{g'^2\mu_B^2H^2+3(-J_z+g \mu_B H)^2+3(J_x^2+J_y^2)} \\ \cos\theta_1 &= \frac{-g'^3\mu_B^3H^3+9g' \mu_B H\{(-J_z+g \mu_B H)^2+(J_x^2+J_y^2)/2\}-27J_x J_y (-J_z+g \mu_B H)}{\{g'^2\mu_B^2H^2+3(-J_z+g \mu_B H)^2+3(J_x^2+J_y^2)\}^{\frac{3}{2}}} \\ R_2 &= \frac{2}{3}\sqrt{g'^2\mu_B^2H^2+3(J_z+g \mu_B H)^2+3(J_x^2+J_y^2)} \\ \cos\theta_2 &= \frac{g'^3\mu_B^3H^3-9g' \mu_B H\{(J_z+g \mu_B H)^2-(J_x^2+J_y^2)/2\}+27J_x J_y (J_z+g \mu_B H)}{\{g'^2\mu_B^2H^2+3(J_z+g \mu_B H)^2+3(J_x^2+J_y^2)\}^{\frac{3}{2}}} \end{aligned}\right\}. \tag{AIII-19}$$

Accordingly, the magnetization is calculated in the following way. The free energy F is given by,

$$F = - Nk_BT \ln Z, \tag{AIII-20}$$

$$Z=\sum_{i=1}^{8}\exp(-W_i/k_BT) \quad , \qquad \text{(AIII-21)}$$

where N is the concentration of trimer spin, which is equal to that of Cu impurity atoms and Z the partition function.

Consequently, the magnetization is calculated as,

$$M=(-\frac{\partial F}{\partial H}) = -\frac{N}{W}\sum_{i=1}^{8}\frac{\partial W_i}{\partial H}\exp(-W_i/k_BT) \quad , \qquad \text{(AIII-22)}$$

where

$$\frac{\partial W_1}{\partial H}=\frac{\partial R_1}{\partial H}\cos\frac{\theta_1}{3}-\frac{R_1}{3}\frac{\partial\theta_1}{\partial H}\sin\frac{\theta_1}{3}+\frac{g'\mu_B}{6} \quad , \qquad \text{(AIII-23)}$$

$$\frac{\partial W_2}{\partial H}=\frac{\partial R_1}{\partial H}\cos\frac{\theta_1+2\pi}{3}-\frac{R_1}{3}\frac{\partial\theta_1}{\partial H}\sin\frac{\theta_1+2\pi}{3}+\frac{g'\mu_B}{6} \quad , \qquad \text{(AIII-24)}$$

$$\frac{\partial W_3}{\partial H}=\frac{\partial R_1}{\partial H}\cos\frac{\theta_1+4\pi}{3}-\frac{R_1}{3}\frac{\partial\theta_1}{\partial H}\sin\frac{\theta_1+4\pi}{3}+\frac{g'\mu_B}{6} \quad , \qquad \text{(AIII-25)}$$

$$\frac{\partial W_4}{\partial H}=\frac{\partial R_2}{\partial H}\cos\frac{\theta_2}{3}-\frac{R_2}{3}\frac{\partial\theta_2}{\partial H}\sin\frac{\theta_2}{3}-\frac{g'\mu_B}{6} \quad , \qquad \text{(AIII-26)}$$

$$\frac{\partial W_5}{\partial H}=\frac{\partial R_2}{\partial H}\cos\frac{\theta_2+2\pi}{3}-\frac{R_2}{3}\frac{\partial\theta_2}{\partial H}\sin\frac{\theta_2+2\pi}{3}-\frac{g'\mu_B}{6} \quad , \qquad \text{(AIII-27)}$$

$$\frac{\partial W_6}{\partial H}=\frac{\partial R_2}{\partial H}\cos\frac{\theta_2+4\pi}{3}-\frac{R_2}{3}\frac{\partial\theta_2}{\partial H}\sin\frac{\theta_2+4\pi}{3}-\frac{g'\mu_B}{6} \quad , \qquad \text{(AIII-28)}$$

$$\frac{\partial W_7}{\partial H}=\frac{g'\mu_B}{2} \quad , \qquad \text{(AIII-29)}$$

$$\frac{\partial W_8}{\partial H}=-\frac{g'\mu_B}{2} \quad , \qquad \text{(AIII-30)}$$

and

$$\frac{\partial\theta_1}{\partial H}=-\frac{1}{\sqrt{1-\cos^2\theta_1}}\frac{\partial(\cos\theta_1)}{\partial H} \quad , \qquad \text{(AIII-31)}$$

$$\frac{\partial\theta_2}{\partial H}=-\frac{1}{\sqrt{1-\cos^2\theta_2}}\frac{\partial(\cos\theta_2)}{\partial H} \quad . \qquad \text{(AIII-32)}$$